Title
Study of MHD Corrosion and Transport of Corrosion Products of Ferritic/Martensitic Steels in the Flowing PbLi and its Application to Fusion Blanket

Author
Saeidi, Sheida

Publication Date
2014

Peer reviewed|Thesis/dissertation

UNIVERSITY OF CALIFORNIA

Los Angeles

Study of MHD Corrosion and Transport of Corrosion Products of Ferritic/Martensitic Steels in the Flowing PbLi and its Application to Fusion Blanket

A dissertation submitted in partial satisfaction of the

requirements for the degree Doctor of Philosophy

in Mechanical Engineering

by

Sheida Saeidi

2014

Abstract of the Dissertation

Study of Corrosion and Transport of Corrosion Products of Ferritic/Martensitic Steels in Flowing PbLi and its Application to Fusion Blankets

by

Sheida Saeidi

Doctor of Philosophy in Mechanical Engineering

University of California, Los Angeles, 2014

Professor Mohamed Abdou, Chair

Two important components of a liquid breeder blanket of a fusion power reactor are the liquid breeder/coolant and the steel structure that the liquid is enclosed in. One candidate combination for such components is Lead-Lithium (PbLi) eutectic alloy and advanced Reduced Activation Ferritic/Martensitic (RAFM) steel. Implementation of RAFM steel and PbLi in blanket applications still requires material compatibility studies as many questions related to physical/chemical interactions in the RAFM/PbLi system remain unanswered. First of all, the mass loss caused by the flow-induced corrosion of the steel walls at temperatures in the range 450 °C - 550 °C needs to be better characterized. Second, another serious practical concern is the transport

of activated corrosion products and their precipitation in the cold section of the loop. Third, an important modeling parameter, the saturation concentration of iron in PbLi, needs further evaluations as the existing correlations demonstrate scattering of several orders of magnitude. Besides, the existing experimental data on corrosion are often contradictive and the underlying physics is not well understood, especially if the PbLi flow is turbulent and strongly affected by the applied magnetic field due to magnetohydrodynamic (MHD) effects in the flowing liquid metal.

The research performed here is aimed at: (1) better understanding of corrosion processes in the system including RAFM steel and flowing PbLi in the presence of a strong magnetic field and (2) prediction of corrosion losses in conditions of a Dual Coolant Lead Lithium (DCLL) blanket, which is at present the key liquid metal blanket concept in the US. To do this, numerical and analytical tools have been developed and then applied to the analysis of corrosion processes.

First, efforts were taken to develop a computational suite called TRANSMAG (Transport phenomena in Magnetohydrodynamic Flows) as an analysis tool for corrosion processes in the PbLi/RAFM system, including transport of corrosion products in MHD laminar and turbulent flows. The computational approach in TRANSMAG is based on simultaneous solution of flow, energy and mass transfer equations with or without a magnetic field, assuming mass transfer controlled corrosion and uniform dissolution of iron in the flowing PbLi. Then, the new computational tool was used to solve an inverse mass transfer problem where the saturation concentration of iron in PbLi was reconstructed from the experimental data resulting in the following correlation: $C^S = e^{13.604-12975/T}$, where T is the temperature of PbLi in K and C^S is in wppm. The new correlation for saturation concentration was then used in the analysis of corrosion processes in laminar flows in a rectangular duct in the presence of a strong transverse magnetic field. As shown in this study, the mass loss increases with the magnetic field such that the

corrosion rate in the presence of a magnetic field can be a few times higher compared to purely hydrodynamic flows. In addition, the corrosion behavior was found to be different between the side wall of the duct (parallel to the magnetic field) and the Hartmann wall (perpendicular to the magnetic field) due to formation of high-velocity jets at the side walls. In the blanket conditions, the side walls experience a stronger corrosion attack demonstrating a mass loss up to 2-3 times higher compared to the Hartmann walls. The analysis for a case of a strong magnetic field suggests scaling laws for the mass loss *ML* in rectangular ducts, which include the effects of the temperature *T*, mean bulk velocity U_{m} and the applying magnetic field B_0: $ML \sim e^{pT} U_m^q B_0^s$ for the side wall, and $ML \sim e^{pT} U_m^q$ for the Hartmann wall, where $q, s \sim 0.5$. As seen from these laws, the mass loss at the Hartmann wall is not affected by a magnetic field providing the magnetic field is high.

Further analysis was performed for corrosion in the Hartmann flow, which is the MHD analog of the hydrodynamic Poiseuille flow. The main goal of the analysis is to elucidate the effect of a magnetic field on the corrosion mass loss in the case when the applied magnetic field is perpendicular to the flow-confining wall. It was found that the corrosion rate is strongly dependent of the ratio between the thickness of the concentration boundary layer and that of the magnetohydrodynamic Hartmann boundary layer. Once the concentration boundary layer becomes thicker than the Hartmann layer, further increase in the magnetic field does not affect the corrosion rate. A self-similar solution for the concentration field was derived for two particular cases: (i) the thickness of the concentration boundary layer is much smaller than the thickness of the Hartmann layer and (ii) the Hartmann layer is much thinner than the concentration boundary layer. The derived solutions comply very well with the numerical data and thus can be recommended for calculations of the corrosion mass loss in fusion applications and also to analyze experimental data.

Analysis of the effect of a magnetic field on corrosion of RAFM steel in a turbulent PbLi flow is performed using numerical simulations. The impact of the magnetic field strength and its direction for this mass transfer problem is analyzed with the aid of a mass transfer equation for dissolved products coupled with the MHD equations. This approach utilizes a special form of the "*K*-ε" model of turbulence, which takes into account the effect of turbulence suppression by a magnetic field. Computations are performed for three orientations of the magnetic field, with respect to the main flow (streamwise, spanwise and wall-normal B-field) in the temperature range from 400 °C to 550 °C, which is of particular interest for fusion cooling applications. Changes in the corrosion rate caused by MHD effects have been analyzed with regard to turbulence modification by a magnetic field and to formation of the Hartmann boundary layer at the walls perpendicular to the magnetic field. As demonstrated, for all three magnetic field orientations, decrease of the corrosion rate occurs as the magnetic field increases. However, a wall-normal magnetic field has a stronger effect on the reduction of the corrosion rate compared to the other two magnetic field orientations due to more intensive turbulence suppression. For the case of a wall-normal magnetic field, a correlation for the turbulent dimensionless mass transfer coefficient (Sherwood number, *Sh*) has been constructed based on the numerical data, which shows the effect of the flow velocity via the Reynolds number (*Re*) and that of the applied magnetic field via the Hartmann number (*Ha*): $Sh = Sh_0 - 0.792 \times \left(Ha^{1.289} \right)$, where Sherwood number in a purely hydrodynamic flow Sh_0 is a function of *Re*.

The developed analytical and computational tools have been used in the calculations of the corrosion mass loss in the poloidal ducts of the DCLL blanket under conditions of the so-called US DEMO reactor. The present analysis is limited to the outboard region of the reactor where the magnetic field is ~ 4 T. One of the goals of the analysis is to establish conditions when a high PbLi

temperature at the blanket exit of ~700°C needed for high thermal efficiency of the power conversion cycle can be achieved, while the corrosion mass loss is maintained within the allowable limits. At present, the suggested maximum for the corrosion wall thinning is 20 μm/yr. The analysis includes parametric studies, using the electrical conductivity of the insulating flow channel insert (FCI) and the PbLi temperature as parameters. Also, more detailed computations have been performed using computed temperature distributions from the 3D MHD/thermofluid analysis. The obtained corrosion data suggest that the most corrosion losses occur in the thin gap between the First Wall and the FCI (side-wall section of the gap), while the corrosion losses in the Hartmann-wall section of the gap are almost negligible due to very low velocities there. Also, the maximum temperature at the interface between the RAFM wall and the flowing PbLi (which guaranties the average wall thinning < 20 μm/yr) was estimated at about 470 °C. This is consistent with the estimate from a more conservative analysis in the past.

The dissertation of Sheida Saeidi is approved.

Jeffrey D. Eldredge

Adrienne G. Lavine

George J. Morales

Sergey Y. Smolentsev

Mohamed A. Abdou, Committee Chair

University of California, Los Angeles

2014

Dedication

This work is dedicated to my parents Farima Mashhour and Hamid. R. Saeidi. All I have now and ever will accomplish are only possible due to their unlimited love, support and sacrifices.

I love you so much…

TABLE OF CONTENTS

List of Figures

List of Tables

NOMENCLATURE

Symbols or Abbreviations

RAFM	Reduced Activation Ferritic/Martensitic Steel
LM	Liquid Metal
Li	Lithium
PbLi	Lead-Lithium
MHD	Magnetohydrodynamic
ITER	International Thermonuclear Experimental Reactor
HCLL	Helium-Cooled Lithium-Lead
DCLL	Dual Coolant Lead Lithium
TBM	Test Blanket Module
BCSS	Blanket Comparison and Selection Study
FCI	Flow Channel Insert
He	Helium
SiC	Silicon Carbide
Ha	Hartmann number
Re	Reynolds number
Pe_D	Peclet number for diffusion
N	Interaction parameter or Stuart number
Pr	Prandtl number
Q2D	Quasi-Two-Dimensional
D-T	Deuterium-Tritium

DNS	Direct Numerical Simulation
$k-\varepsilon$	$k-\varepsilon$ model of turbulence
$\vec{u}(u,v,w)$	Velocity vector, (m/s)
$\vec{j}(j_x, j_y, j_z)$	Current density vector, (A)
p	Pressure, (Pa)
T	Absolute Temperature, (K)
C	Iron concentration, (kg/m$^{3)}$
D_h	Hydraulic diameter, (m)
J_i	Net mass flux of element *i*
r:	Loop position, (m)
k_i^z	Effective rate constant for dissolution, (m/s)
k_i^s	Effective rate constant for deposition, (m/s)
C_i^b	Local bulk concentration, (kg/m^3)
C_i^0	Solubility of element *I* in the liquid metal, (kg/m^3)
Δm^s	Mass of corroded material, (kg)
Δm^p	Mass of deposited material, (kg)
Δm^f	mass of particles that formed and stayed suspended, (kg)
Δm^d	Mass of detached deposits, (kg)
I	Mass flux from the wall, (kg/m^{2}s)
N	Species density, (atom/m^3)
D_{eff}	Effective diffusion coefficient, (m^2/s)
P	Species production, (atoms/m^3 s)

L	Species loss rate, (atoms/m^3 s)
C^S	Saturation concentration of iron in PbLi, (kg/m^3)
C_0	Inlet concentration
C_W	Concentration in the liquid metal at the interface, (wall concentration)
C_b	Concentration of iron in the bulk, (kg/m^3)
k	Dissolution rate constant, (m/s)
K	Mass transfer coefficient, (m/s)
D	diffusion coefficient of iron in PbLi, (m^2/s)
B_x	Induced magnetic field, (T)
C_w	Conductance ratio
$\vec{B}$	Magnetic field vector, (T)
t	time, (s)
x	Coordinates along the flow or axial coordinate, (m)
y	Coordinates across the flow or radial coordinate, (m)
z	Toroidal coordinate, (m)
λ	Thermal conductivity, (W/mK)
C_P	Specific heat, (J/kg K)
ρ	Density, (kg/m^3)
ν	Kinematic viscosity, (m^2.s),
$\mathcal{V}$	representing mass loss in Sannier's equation, (μm/yr)
a	Duct-half width in radial direction, (m)

b	Duct-half width in toroidal direction, (m)
L	Characteristic flow dimension
U_m	Mean bulk velocity
B_o^z	Applied magnetic field
σ	Electrical conductivity, (S/M)
t_w	Wall thickness
ξ_*	Dimensionless coordinate
h	Half channel width
$\dot{q}$	Volumetric heating due to neutrons
q_0	Maximum volumetric heating
$\bar{q}$	Mean volumetric heating
u', v', p', θ'	Perturbed quantities
k	Thermal conductivity

Greek Symbols

ϕ	Electric potential
σ	Electrical conductivity
μ	Magnetic permeability

Indices

cr	Critical
s	Saturation
w	Wall
b	Bulk
m	Mean
t	Turbulent transport properties

ACKNOWLEDGEMENTS

First and foremost I would like to express the deepest appreciation to Prof. Mohamed Abdou for giving me an opportunity to purse a graduate degree at UCLA, for supporting me over the years of graduate school, and for helping me in both the research performed and in preparation of this thesis.

I would like to extend my gratitude to my adviser Dr. Smolentsev for all of his patient guidance, teaching, insightful ideas and long hours of reading and revising my numerous revisions, this research and dissertation could not have been completed without him.

I would like to thank my committee members Prof. Lavine, Prof. Eldredge and Prof. Morales for all their support throughout.

I wish to acknowledge that this research is supported by the US Department of Energy (DOE) program grant under DOE Grant No. DE-FOA-0000603.

I would like to thank all fusion groups personal: Tom Sketchy, Samantha Townsend, Arnaud Larousse, Emily Hoffman, and Allison Ross. I would like to thank my colleagues at Fusion Science and Technology center. Special thanks to Dr. Vetcha for all of his help during my research. Dr. Prakash for endless email discussions, Dr. Vakhshouri for his endless support during the first year of graduate school, and Jack Young for always proof reading my manuscripts. I am very fortunate to work with the greatest people UCLA fusion group: Ryan, Hongjie, Jon, Anchol, Damien, Jack, Alberto, Haibo, Mo, Charlie, Tylor and Gautam.

I like to give a special recognitions to my special friend Samantha Townsend for always consulting me on matters needed to be addressed regarding administrative procedures, and for guiding me on the endless prepration for my qualification exam and the defense exam.

I have also been very fortunate to have number of close friends during my graduate school. I will always be indebted to friends like Melina Roshandell, Mandana Farhadieh, Ladan Amouzegar, Sarah Pashae, and Reyhaneh Zamani who helped me in a lot of different ways.

I have to say without my best friend unlimited support, Sarah Pashae, dissertation process was impossible. She was there every second of the day to help me get through all the emotional obstacles I encountered.

I am so grateful for the most important people in my life, my beautiful family. My divine parents, Farima and Hamid-Reza, the sweetest grandma, Fakhri, my amazing brother and sister, Mohammad-Reza and Shadi who supported me always and forever.

Finally, I want to thank the love of my life, my compassionate husband, Arash Shafi, for his understanding, endless love and support all these years of graduate school. I started this journey with him and I finished with him always having my back. I have to say he was the best part of this journey, and meeting him at UCLA was a miracle. He gave a new dimention to my life, and I always owe him for that. After long hours of work at school, it was his presence at home that motivated me to leave work behind, and live a life beside my PhD.

Sheida Saeidi

Los Angeles

June 2014

VITA

2008	B.S., University of California, San Diego, Chemical Engineering
2010	M.S., University of California, Los Angeles, Mechanical Engineering
2014	Ph.D. Canidate, University of California, Los Angeles, Mechanical Engineering

PUBLICATIONS

S. Smolentsev, S. Saeidi, S. Malang, M. Abdou, "Numerical study of corrosion of ferritic/martensitic steels in the flowing PbLi with and without a magnetic field," *Journal of Nuclear Materials*, 432(2012) 294-304.

S. Saeidi, S. Smolentsev, "Numerical study of the effect of a magnetic field on corrosion of ferritic/martensitic steel in a turbulent PbLi flow", *Magnetohydrodynamics*,50 (2014)

S. Smolentsev, S. Saedi , M. Abdou, , "Modeling Liquid Metal Corrosion in a Ferritic Steel - PbLi System with and without a Magnetic Field", *Proceedings of the 8th PAMIR International Conference on Fundamental and Applied MHD*, September 5-9, 2011, Borgo, France, Vol. 2, 593-597 (2011).

CHAPTER 1

INTRODUCTION

1.1 Problem Statement

Lead-lithium (PbLi) eutectic alloy and advanced reduced activation ferritic/martensitic (RAFM) steel, such as F82H or EUROFER, are envisaged as practical candidates for using in breeding blankets of a fusion power reactor as a breeder/coolant and a structural material respectively. Implementation of these materials in blanket applications still requires material compatibility studies as many questions related to physical/chemical interactions between PbLi and RAFM steels as well as earlier ferritic/martensitic steels remain to be answered (see, *e.g.* [1]). First of all, the mass loss caused by the flow-induced corrosion of the steel walls in the flowing PbLi at temperatures in the range between 450 °C to 550 °C, relevant to blanket operation conditions needs to be characterized. Present PbLi blanket studies limit the maximum wall thinning to 20 μm/yr that corresponds to the maximum wall temperature at the interface with the liquid metal in the hot leg of about 470 °C. These limits were derived in the past in the US in the Blanket Comparison and Selection Study (BCSS) [2] based on experience with sodium loops, where blocking of the liquid metal circuit by precipitated corrosion products was frequently observed in the cold section of the loop (see, *e.g.*, [3]). The experimental data on the mass loss for ferritic/martensitic steels in

the flowing PbLi vary however over a wide range, predicting possible wall thinning at temperatures higher than 450 °C from 20 μm/yr [4] to 900 μm/yr [5] (see also Table 1.1).

Table 1.1: Corrosion rate of ferritic/martensitic steels in the flowing PbLi

Steel	T_{max} (°C)	Flow regime	Corrosion rate (μm/yr)	B field	Reference
Fe-12Cr-1MoVW	500	Laminar	24	-	Tortorelli, 1986 [23]
HT-9, Fe-9CR	482	Laminar	20	-	Chopra, 1986 [4]
1.4914	550	Turbulent	370	-	Borgstedt, 1988 [41]
1.4914, HT9, T91	450	Laminar	30	-	Broc, 1988 [42]
1.4914	475	Turbulent	40	-	Sannier, 1991 [16]
MANET-1 , OPTIFER, F82H	480	Turbulent	100	-	Glasbrenner, 2000 [43]
EUROFER 97	480	Laminar	40	-	Benamati, 2002 [18]
EUROFER	550	Laminar	237-530	-	Bucenieks, 2006 [5]
EUROFER	550	Laminar	550-900	1.7 T	Bucenieks, 2006 [5]
EUROFER, MANET I, OPTIFER IVa, F82H-mod.	480	Turbulent	90	-	Konys, 2009 [22]
EUROFER, MANET I, OPTIFER IVa, F82H-mod.	550	Turbulent	400	-	Konys, 2009 [22]

Corrosion is usually defined as the disintegration of an engineered material into its constituent atoms due to chemical reactions with its surroundings. In the most common use of the word, this means electrochemical oxidation of metals in reaction with an oxidant. Corrosion of different types of steel (ferritic, martensitic, austenitic) in liquid metals (also known as “liquid-metal

attack") is different from many other known types of corrosion, where electron transport is of primary importance [6]. Unlike such types of corrosion, liquid-metal corrosion for the most part simply depends on the solution rate (not taking into account the effects due to induced electric currents in magnetohydrodynamic, MHD, flows) and the extent of solubility of the solid metal in the liquid metal. However, many complicating factors can influence the solution rate or the attainment of the solubility limit. The formation of surface intermetallic compounds and of oxide or nitride films are good examples of such factors. Other factors are: impurities in the liquid metals, which can increase the solution rate, the temperature gradients, and multi-metallic systems, which can cause an increase in the amount of attack over that expected. In the ducts of a liquid-metal blanket, the corrosion products dissolved in the liquid metal are then transported due to convection and diffusion in the flow. In some regions characterized for example by lower temperatures compared to the hot leg of the liquid-metal loop, these corrosion products can crystallize and form aggregates which can be deposited on the wall and thus can contribute to the plugging of the ducts. Deposition of corrosion materials, another mass transfer process, is usually considered as a mechanism opposite to corrosion but in fact it is significantly different from corrosion in many ways and is much less understood than corrosion itself. Both corrosion and deposition can have significant effect on blanket operation and performance.

Along with a possible deterioration of the mechanical integrity of the blanket structure due to the wall thinning at the interface with the flowing PbLi, there are other serious concerns associated with the transport of corrosion products throughout the liquid metal loop. When transported with the flowing PbLi in the blanket ducts, the corrosion products can be activated by the intense neutron flux. Their precipitation in the cold part of the PbLi loop, *e.g.* in a heat exchanger, may lead to considerable safety problems, particularly if deposition of corrosion products result in

localized regions of high concentration of activated materials. Plugging the loop by precipitated corrosion products in the cold section is another concern. Such an event has been reported in many experimental studies (see, *e.g.*, [7-9]). At present, it is widely assumed that deposition processes in the cooler parts of a loop are more critical to the safe blanket operation than reduction of strength by wall thinning in the hotter parts. In any case, the corrosion data are required to address transport of corrosion products throughout the liquid metal loop, in particular, to address their deposition in the cold section. Some considerations are given to deposition of corrosion materials in the cold section of the liquid-metal loop and to magnetic traps as a tool for extracting ferrous material from the loop to avoid loop plugging.

In what follows, this study will limit the considerations to particular solid materials. Among structural solid materials there are three types of steel: ferritic, martensitic, and austenitic. Martensitic stainless steels, the first stainless steels commercially developed, have a relatively high carbon content (0.1 - 1.2%) compared to other grades of stainless steels. They contain between 12 and 18% chromium. This stainless steel is of moderate corrosion resistance which can be hardened by heat treatment resulting in high strength and hardness. It has poor weldability, and it is magnetic. The ferritic steels are plain chromium stainless steels with varying chromium content between 11% and 18%, but with low carbon content. They have a moderate to good corrosion resistance, and are not hardenable by heat treatment. They are magnetic as well. Most commonly used austenitic stainless steels contain 18% chromium and 8% nickel. They have an excellent corrosion resistance, weldability, formability fabricability, ductility, cleanability and hygiene characteristics. Along with good high and excellent low temperature properties, these are non-magnetic and are hardenable by cold work only. This is the most widely used stainless steel.

Corrosion behavior of ferritic-martensitic steels, such as EUROFER or F82H, in the flowing PbLi is the main focus of the present literature review, since these materials are considered for using in the US DCLL blanket. Corrosion of austenitic steels in PbLi is reviewed in much smaller extent and liquid-metal corrosion in pure Li is not addressed at all since the concept of the self-cooled Lithium-Vanadium blanket is presently not developed in the US anymore. Several variables affecting liquid-metal corrosion must be considered, such as: (1) temperature; (2) temperature gradient; (3) surface area to volume ratio; (4) purity of liquid metal; (5) flow velocity, or Reynolds number; (7) surface condition of container material; (8) number of materials in contact with the same liquid metal.

Temperature is one of the most important variables on the corrosion rate. The higher the temperature is the higher the solubility of the solid metal in the liquid metal will be. Also, as the temperature increases, the diffusion rates increase, which is quite important in certain types of liquid-metal corrosion. In liquid-metal blankets, corrosion always occurs in the presence of a flowing liquid metal. Corrosion of steels exposed to the flowing liquid lead alloys can be affected by hydrodynamic parameters. Along with the temperature, the flow characteristic is one of the most important parameters that might increases the corrosion rate compared to static liquids. In general, the different mechanisms of combined action of flow and corrosion lead to four types of flow-induced corrosion [10]: (1) mass transport-controlled corrosion, (2) phase transport-controlled corrosion, (3) erosion-corrosion, and (4) cavitation-corrosion. At low velocities (mostly laminar flows), the corrosion rate is completely or partially mass transfer controlled. In such a case, the global dissolution at the solid-liquid interface is at the equilibrium and the corrosion process is thus limited by the diffusion/convection of the dissolved species through the boundary layer at the material interface to the bulk of the flow. The flow in the boundary layer mostly

controls mass transfer, therefore, in these conditions, the corrosion rate increases with increasing velocity (Fig. 1.1). Most of the studies performed in liquid metals have shown that a corrosion process is controlled by mass transfer. However, the studied velocity range was quite narrow. For example, in the case of PbLi, the maximum velocity of the alloy was 0.3 m/s [11]. Therefore, it is very likely that in the Helium-Cooled Lead-Lithium (HCLL) blanket (typical velocity < 1 mm/s), DCLL blanket (typical velocity ~ 0.1 m/s) and even in a self-cooled blanket (typical velocity ~ 0.5 m/s), the mass transfer-controlled corrosion is the dominating mechanism.

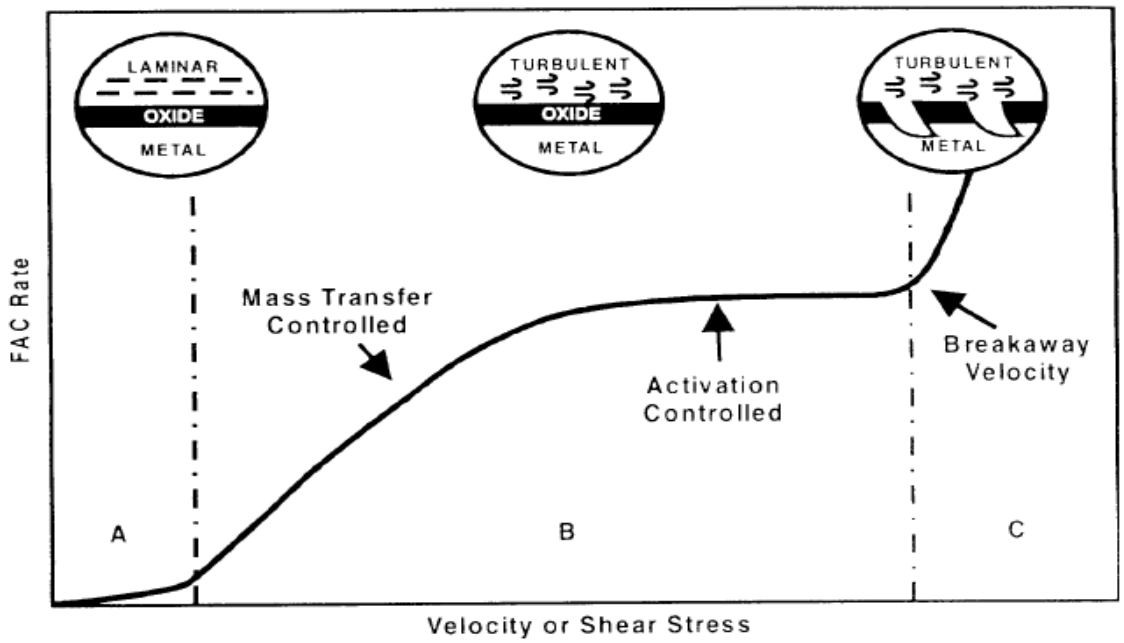

Figure 1.1: Variation of the mechanism of flow accelerated corrosion (FAC) as a function of the fluid velocity [10].

At high velocities when the flow becomes turbulent, the dissolution reaction at the solid-liquid interface becomes the limiting step. In this region, the corrosion rate is independent of the fluid velocity and, in principle, also of the geometry. At much higher velocities, erosion-corrosion may occur if the surface shear stress is high enough to strip a protective layer film from the surface.

Further increase in the corrosion rate can also be caused by mechanical interaction between the solid particles suspended in the flowing liquid and the wall. These types of corrosion associated with fully-developed turbulent flows are not expected in the liquid-metal blanket conditions with some possible exceptions in case of quasi-two-dimensional (Q2D) turbulent flows associated with MHD effects [12].

The observed variations in the experimental data on corrosion in the ferritic/martensitic steel-PbLi system point to a strong influence of the interface temperature and, what is also important, of the flow itself, including flow development effects, and especially turbulence and magnetohydrodynamic (MHD) phenomena [5]. Although the influence of the temperature on corrosion processes is known to be described well with a kind of Arrhenius law, the flow effects are poorly understood. The existing experimental data are in fact not sufficient to explain the strong variations in the corrosion rate, first of all due to uncertainties related to different flow conditions in the experiments. Moreover, these experimental data are mostly limited to purely hydrodynamic flows and thus cannot be used to predict corrosion processes and transport of corrosion products in a real blanket system, where the flowing PbLi is severely affected by a strong plasma confining magnetic field. General discussion of possible effects of a magnetic field on corrosion and deposition in PbLi is given in [13]. The main effect of the magnetic field on corrosion processes seems to be due to changes in the velocity profile, mostly due to steeper velocity gradients in the near-wall region and associated changes in the temperature distribution in the flow and at the material interface with the solid metal.

1.2 Scope of Work

This study covers ongoing work on modeling flow-induced corrosion processes in the ferritic/martensitic steel-PbLi system. Implementation of the eutectic alloy PbLi and ferritic steel in blanket applications requires further material compatibility studies, including a study of corrosion of ferritic walls in flowing PbLi at elevated temperatures relevant to the blanket operation conditions. The Scope of this work is to study flow-induced corrosion in the ferritic/martensitic steel-PbLi system in the presence of a magnetic field. This study tries to reduce the amount of uncertainties related to available experimental data on corrosion. In order to do that, both laminar and turbulent regimes have been addressed. Regarding the blanket application, corrosion computations will be considered in US DCLL blanket conditions in the presence of a strong magnetic field (4 T), in the presence of temperature gradient (400-700 ^{o}C), and in complex geometry including an upward and downward flow of PbLi in multi-channel structure for Demo. It is important to mention that this study assumes that the main corrosion process that eventually determines the wall mass loss arises from the uniform dissolution of iron, and only iron concentration in the PbLi is computed. Transport of other metallic components (Cr, Ni, Mn, W, V, Ta) is not considered in this study due to their lower concentration. In what follows, this study will limit the considerations to particular solid materials.

Two new computer programs have been developed to solve simultaneously the fluid flow, energy and mass transfer equations for either turbulent or laminar flows with or without a magnetic field. The model for turbulent flows is 2-D. The simulations performed using this code is mostly aimed originally at improving the existing data on the saturation concentration and then performing simulation for the case of turbulent MHD flow. In order to do this, the inverse problem was solved where the data on saturation concentration of iron in PbLi is reconstructed by comparing the

calculated results for the mass loss with the available experimental data. The second computer program covers the case of laminar MHD flows in an electrically conducting rectangular duct. This code utilizes a model of a fully developed 2D MHD flow, while the mass and heat transfer equations are solved in 3-D. The obtained data on the saturation concentration are then approximated with a new correlation, which is used to perform further analysis and comparisons. In particular to address the effects of the magnetic field, the temperature, and the flow velocity on the mass loss in MHD turbulent or laminar duct flows.

1.3 Contributions of Proposed Study to Field of Research

The benefits of successfully completing this research are immediately tangible. This work will produce a numerical study for induced-flow corrosion analysis of ferritic/martensitic steel walls, which will be directly applicable to manufacturing and qualification criterias for use in DEMO test blanket modules, as well as any future nuclear machine. Additionally, mass transfer data produced for these applications can be used as a reference guide in dealing with systems of similar. One such benefit from this work would be the improved understanding of the diffusion depths of elements mainly iron, at the interface of the solid wall into a flowing liquid metal. Characterization of the diffusion would produce data that can be referenced by future researchers. In this way, this research serves to provide both a general reference to community as well as useful applications.

1.4 Study Objective

The goal of the present research is to understand and compute corrosion phenomena and transport of corrosion products of ferritic/martensitic walls in the flowing PbLi inside the poloidal ducts of the fusion blanket associated with magnetic field effect. In support of this, the proceeding plan is followed:

1) The mass transfer problem is studied first by numerical investigation for simple flow geometry cases. The goal of this study is to improve existing correlations for the saturation concentration to predict corrosion rates more accurately. (Chapter 3)
2) The next step is to do more analysis using the new correlation for corrosion computations of laminar flow while a strong transverse magnetic field is applied. (Chapter 3)
3) The next is to conduct an analytical corrosion study for laminar flow under a transverse magnetic field in order to validate results obtained numerically. (Chapter 4)
4) The next goal of this study is to investigate the main effect of a magnetic field on corrosion and transport of corrosion products for turbulent flow. The existing experimental data are mostly limited to purely hydrodynamic flows and thus cannot be used to predict the corrosion process and transport of corrosion product in a real blanket system, where the flowing PbLi is severely affected by a strong plasma confining magnetic field. As a result, this study proposes further experimental and modeling efforts, including development and testing of phenomenological models and boundary conditions followed by new numerical algorithm and multi-parameter computation. (Chapter 5)
5) Finally, the main goal of this research is to study the effects of MHD coupled with heat and mass transfer in the domain that includes the bulk and gap flow, FCI, and the ferritic wall in the blanket relevant condition. This study will give a first assessment of the

importance of corrosion of RAFM steel walls in a DCLL blanket which is presently considered for testing in ITER and for further implementation in a DEMO reactor.(Chapter 6)

CHAPTER 2

REVIEW OF KEY LITERATURE

2.1 Experimental Results on Corrosion of Ferritic-Martensitic Steels and Deposition in PbLi

Many liquid-metal corrosion experiments as applied to liquid-metal blanket conditions have been performed in static fluid conditions using simple capsule tests. However, more meaningful test results can be obtained in the dynamic conditions, using flowing liquid metals to carefully reproduce the operating conditions in a blanket. This is usually carried out in convection loops, which are much more expensive, compared to static experiments with capsules. In the case of semi-stagnant tritium breeding blankets, such as HCLL blanket, thermal convection loops with low flow velocity and small temperature gradients are sufficient, while where higher velocities and temperatures are required, *e.g.* DCLL blanket, forced convection loops are necessary [14]. To study flow-induced corrosion, the rotating cylinder technique is also in general use. With this technique it is possible to establish if the corrosion process is limited by mass transfer or by dissolution depending on the law of the weight loss variation with the rotation rate (see refs. in [10]).

Among ferritic-martensitic steels tested experimentally in the recent past using a forced convection loop are RAFM steels, such as EUROFER, F82-H, OPTIFER, and MANET. All these

steels demonstrate similar corrosion behavior in PbLi. Detailed experimental studies on corrosion of these steels in PbLi have been performed in the US at ORNL by Tortorelli *et al.* (see, e.g. [15]), in France by Sannier *et al.* [16-17], in Italy by Ricapito *et al.* (see, *e.g.* [18]), and more recently in Germany using PICOLO loop by Konys *et al.* [9,11,19-22]. The experiments are typically performed with cylindrical samples exposed to the flowing PbLi for about 10,000 hours at operating temperatures above 400 °C and the flow velocities up to 0.3 m/s. The corroded samples are then carefully studied using optical microscopy, SEM/EDX mapping and EDX line-scan analysis (see, *e.g.* [11]).

The main findings from numerous experimental results are the following. The first stage in the liquid-metal attack is dissolving the passivation oxide layer on the steel surface. Such a layer is usually formed during the thermal treatment of steels and consist of $MnCr_2O_4$ and $(Fe,Cr)_2O_3$ detected by means of XPS and AES analysis. This stage is inhomogeneous since the oxide layer is not uniform in thickness and composition and it is due to poor wetting of this layer with PbLi. The wetting of a passivated steel surface by PbLi needs time (*e.g.* up to 3000 h at 500 °C) before the samples fully interact with the flowing liquid metal. This phenomenon is the so-called incubation period. The incubation period decreases as the temperature and the flow velocity increase. After the incubation stage, the corrosion attack proceeds distinctively faster via direct dissolution of iron and chromium.

The second stage of the liquid-metal attack is the dissolution of the steel matrix, which is characterized by a strong depletion of Fe and Cr. The remaining porous zone consists of elements of low solubility in PbLi, such as W, Mo and V, and shows a low adherence to the steel matrix so that it can be easily eroded from the surface by the flowing melt. The thickness of the depleted layer does not exceed 5 μm and the protecting function of this low adherent layer can thus be

neglected. The corrosion during the second stage is essentially uniform and demonstrates mass loss of almost linear in time. No penetration of PbLi in the matrix has been observed.

The corrosion rate in the uniform dissolution phase is severely affected by the temperature and the flow velocity. The corrosion rate at 480 °C and the flow velocity of 0.22 m/s is 90 μm/year compared to 500 μm/year at 550 °C as shown in [9]. The experimental data on corrosion of ferritic-martensitic steels in turbulent flows of PbLi are well described with the so-called Sannier's equation [16]:

$$v = 8 \times 10^9 \times exp\left(-\frac{25690}{1.98T}\right) \times U_m^{0.875} \times D_h^{-0.125}, \mu m/yr \quad (2.1)$$

Here, v is the material loss, T is the absolute temperature of the flowing PbLi, U_m is the mean flow velocity, and D_h is the hydraulic diameter.

With all liquid metals under non-isothermal conditions, deposition constitute are at least as serious concerns as material thinning. The accumulation of deposits can lead to flow restrictions that increase pumping power requirements and affect heat transport. In the worst case scenario, the loop can be completely plugged with the corrosion products deposited on the wall. In nuclear fusion applications, deposition of radioactive species outside the primary reactor area can necessitate increased shielding and remote maintenance. The deposition processes are often considered as a kind of symmetric to corrosion processes. Namely, it is often believed that the amount of material that corroded in the hot section of the liquid-metal loop will be deposited in the cold section once the temperature drops below the saturation limit. This analogy is based on a simple mass transfer equation that describes the net mass flux J_i of element i at loop position r:

$$J_i(r) = k_i^z(r)\left[C_i^0(r) - C_i^b(r)\right] \quad (2.2)$$

here, k_i^z is the effective rate constant for dissolution ($z = s$) or deposition ($z = p$) of element *i*, C_i^0 is the solubility of this element in the liquid metal, and C_i^b is the local bulk concentration of this element. Normally, in the higher temperature region of the loop $C_i^0 > C_i^b$ and dissolution occurs, while in the colder part of the circuit $C_i^0 < C_i^b$ and weight is gained on the solid surfaces. Such solubility-driven transport can be monitored by measurements of weight changes of coupons arrayed around the loop, which typically produce mass transfer profiles. While Eq. 2.2 yields a qualitative understanding of corrosion/deposition in liquid metal systems, it cannot, in many cases, explain the quantitative aspects of deposition caused by additional kinetic and thermodynamic factors compared to corrosion.

Experiments on deposition in a PbLi loop are described in [23]. In these experiments both corroded and deposited amounts of material were measured and compared in the thermal convection loop with the maximum temperature 500 °C and the minimum temperature in the cold section 370 °C. The loop was constructed of type 316 stainless austenitic steel. Data analysis indicated that the corroded amount of material is sufficiently higher than the deposited amount. This can be explained with the fact that there can be a significant amount of the corroded material in the form of solid particles suspended in the liquid (particularly those containing nickel). The deposition of chromium at the same time correlated well with the temperature dependence of solubility. There was also some evidence of physical detachment of deposits. These observations allow for the following mass balance equation for the entire loop:

$$\Delta m^s = \Delta m^p + \Delta m^f + \Delta m^d \tag{2.3}$$

Here, Δm^s is the mass of corroded material, Δm^p is the mass of deposit, Δm^f is the mass of particles that formed and stayed suspended in the PbLi, and Δm^d is that of detached deposits

suspended in the liquid metal. The suspended particles rich in Ni can deposit anywhere in the loop because of their poor solubility in PbLi, particularly at longer times when their density and size in the liquid would be much greater. If such deposition of Ni-containing particles occurs, the deposition rate is not governed by Eq. 2.2, which is based on the solubility mechanism, but rather by hydrodynamic factors and sticking coefficients. A distinct dependence of deposit composition on loop position was also observed. Similar results for corrosion/deposition for austenitic steel, showing significant difference between corroded and deposited masses (by about a factor of 2) have been reported in [17].

Deposition processes in near-stagnant PbLi in the presence of linear temperature variations along the tested tube from 250 to 650 ^{o}C were studied experimentally in [24] for the system entirely composed of austenitic type 316 steel. Two types of deposit have been identified depending on the temperature. In the temperature range between 400 and 550 ^{o}C, large dendrite crystals, composed mainly of iron and chromium were found. At lower temperatures, the crystals are chromium-rich, while at higher temperatures they are iron-reach. Neither iron nor chromium is deposited as a single element. Below 350 ^{o}C, the composition of this deposit is generally nickel-rich with some iron and chromium. Pure nickel only deposits if the alloy is at near saturation in nickel (~600 ^{o}C).

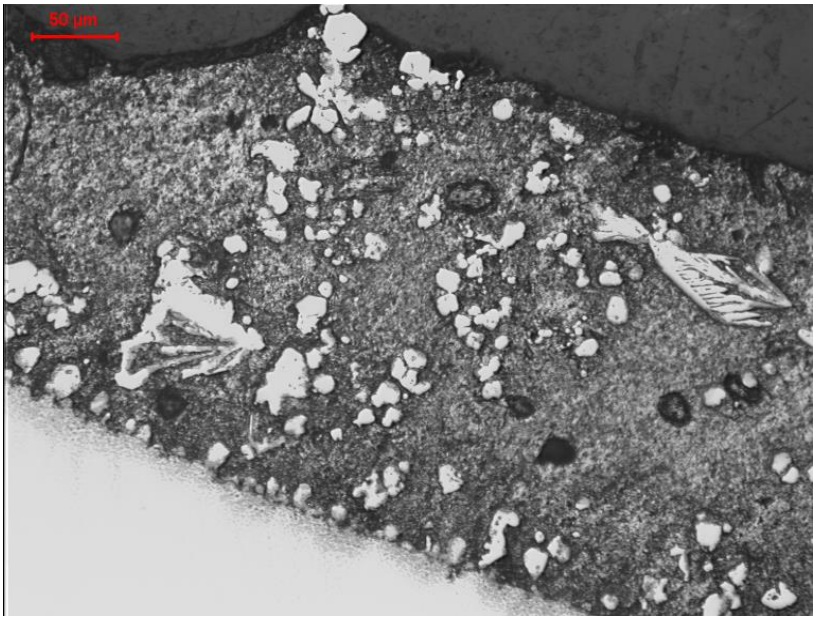

Figure 2.1: Drained tube section with adherent PbLi scale [9].

In contrast with austenitic steels, corrosion/deposition analysis for ferritic steels in PbLi performed in [25] does not demonstrate such a big difference between the weight loss and the weight gain showing that in such systems solubility-driven deposition governed by Eq. 2.2 is probably the most important factor for mass transfer. The small imbalance between Δm^s and Δm^p can be related to formation of Fe-Cr particles that stay suspended in the liquid. All these observations show that predictive capability for modeling and controling of mass transfer in PbLi will be more difficult for austenitic (Fe-Ni-Cr) alloys than for ferritic (Fe-Cr) steels.

Figure 2.2: Precipitations in adherent PbLi scale [9].

Precipitation effects were analyzed in the corrosion experiments in the EUROFER-PbLi system using PICOLO loop in Germany [9] at 550°C in the hot section and 350°C in the cold section. The analyzed tube was located in the cold section of the loop at about 380°C during normal operation. It was cut off from the loop after about 77,000 hours of operation and then analyzed. Coating of the inner wall surface by precipitated Fe/Cr – the opposite of the dissolution process found in the hot zone – is not observed. Instead, the wall is covered (after draining) by a PbLi scale with embedded precipitations in various shapes (Fig. 2.2). The performed EDX scans confirm that the observed particles are formed from the steel components Fe and Cr.

Many of those particles exhibit a dendrite-like structure as shown in Fig. 2.2 with a length more than 100 μm. The large size indicates that they were not formed during the short time of cooling down. Rather than that, the precipitation effect seems to be caused by over-saturation of the melt. However the performed analysis does not indicate the loop position where the precipitations were growing. The large amount of the material extracted from the magnetic trap

in the course of the experiment may also indicate that a significant amount of corroded material does not deposit on the walls but is transported through the entire loop with the flowing liquid in the form of particles suspended in the PbLi. These observations seem to be different form the conclusions of the deposition analysis in [25], which mostly confirms a solubility-driven deposition mechanism. As applied to liquid-metal blankets, all these experimental observations indicate that there can be different scenarios of deposition from a near-uniform deposition on the walls of the cold leg driven by a solubility-driven mechanism, to clogging small orifices by large-size particles staying in the bulk liquid. In the latter case, the driving deposition mechanism is of more hydrodynamic nature, which also involves sticking of particles on the solid surface.

2.2 Theoretical and Modeling Results on Corrosion/Deposition

A few numerical codes, mostly 1D, have been developed in the recent past to simulate transport of corrosion products in big multi-component industrial-type water-cooled and liquid-metal-cooled loops [26-27] for cooling fusion and fission reactor systems. A typical example of the 1D codes is the MATLIM code developed at FZKA [9,22], where the mass transfer equation is reduced to the 1D form by integrating the original 3D equations over the cross-sectional area of the duct. The code had demonstrated a good match with the experimental data for the mass loss in hydrodynamic turbulent flows obtained in the past (see, *e.g.*, [16-17] and more recently [9,19-20]). The range of applicability of the code is however limited due to the uncertainties in the input data, such as the diffusion coefficient, the solubility of iron in PbLi, and the mass transfer coefficient (private communication with J. Konys, Sept. 2011). Of them, the saturation concentration seems to be the most uncertain parameter, demonstrating scattering up to four orders of magnitude. The code also lacks MHD effects and detailed representation of the velocity field

due to its 1D nature. There are also a few multi-dimensional research codes [28-29] that address special effects associated with the flow geometry, for example, those due to the insulating flow channel insert (FCI) in a dual-coolant DCLL blanket [30], where PbLi is used as a breeder and a coolant, while the helium gas is used for cooling the RAFM steel structure.

The PACTITER code, developed by CEA, [31] on the earlier developed PACTOLE code is used for predicting activated corrosion products in ITER primary cooling water systems. The physical model involves transport of corrosion products generated by corrosion-release phenomenon or by oxide dissolution. When the coolant becomes supersaturated in corrosion products, ions can precipitate on the walls or in the bulk of the fluid to form particles. Particles are also generated by erosion processes. Transported by the primary coolant, particles are deposited inside the circuits or they can agglomerate. Two types of radioactive corrosion product formation coexist. On the one hand, the activation of corrosion products occurs when they are deposited on surfaces under neutron flux. On the other hand, the corrosion of structural materials under neutron flux is accompanied by a release of radioactive corrosion products. The PACTOLE and the PACTIFER codes are based on a control volume approach, the primary circuit is represented by an arrangement of several volumes in which transient mass balance equations are solved:

$$\frac{\partial m_i}{\partial t} + (\dot{m}_s - \dot{m}_e) = \sum_{Source} Q_m - \sum_{Sink} Q_m \qquad (2.4)$$

Where m_i the mass of the *i*-th isotope is in a considered medium, *t* is the time, $\dot{m}_s - \dot{m}_e$ is the convective term (balance between input and output), Q_m is the exchange mass rate between two different media.

Code TRAP (Transport of Activation Products) is the general purpose transport and deposition code to predict the behavior of activation products in a liquid-metal cooling loop of a fusion power

plant [32]. The code has been written from the first principles in order to include all possible gaseous or liquid coolants encountered in fusion devices. The code has the capability to treat an unrestricted number of stable and active species and allows for treatment of time dependent effects. Application to the liquid lithium cooling loop demonstrated the versatility of the code to cope with any material and coolant but also pointed to the lack of reliable data for other than water cooling environments. TRAP solves the time dependent coupled coolant transport and bulk solid diffusion mass transfer equations in the following form:

$$\frac{\partial N}{\partial t} + U\frac{\partial N}{\partial x} = P - L, \quad \frac{\partial N}{\partial t} = \frac{\partial}{\partial s}\left(D_{eff}\frac{\partial N}{\partial s}\right) + P - L. \tag{2.5}$$

Here, N (atoms/m^3) is the species density, U (m/s) is the flow velocity, t (s) is the time, x (m) is the length along the flow direction, s (m) is the radial length (across the wall), D_{eff} (m^2/s) is the effective diffusion coefficient of atoms/ions into the bulk solid, and P (atoms/m^3-s) and L (atoms/m^3-s), the species production and loss rates respectively.

2.3 Effect of a Magnetic Field on Corrosion/Deposition

All the above reviewed experimental studies have been performed without a magnetic field and in no-irradiation conditions. The effect of neutron irradiation on corrosion behavior is very difficult to study in experiments. The effect of the applied magnetic field can, however, be addressed experimentally using available MHD facilities.

Only a few experimental studies [5,33-35] have been performed in the presence of a magnetic field, predicting significant increase in the wall mass loss, up to 2-3 times, if a magnetic field is

applied. These results still need to be explained and/or reexamined. This necessitates further experimental and modeling efforts, including development and testing of phenomenological models and boundary conditions followed by new numerical codes and multi-parameter computations. General discussion of possible effects of a magnetic field on the liquid-metal corrosion and deposition in PbLi is given in [36]. The main effect of the magnetic field on corrosion/deposition processes seems to be due to changes in the velocity profile, mostly due to steeper velocity gradients in the near-wall region, and associated changes in the temperature distribution in the flow and at the material interface with the solid metal. Significant changes can occur due to turbulence modification (suppression of 3D turbulence and appearance of Q2D turbulent pulsations) by a strong magnetic field. Some modifications in both corrosion and deposition processes are also possible due to induced electric currents crossing the interface, as these currents may have an effect on the corrosion/deposition kinetics. As currently shown (private communication with Prof. Rene Moreau), the electric current can be responsible for the so-called electromagnetic migration, which seems to be as important as the simple dissolution mechanism. Solubility of a solid metal in the liquid metal is the important parameter in corrosion/deposition processes as directly seen from Eq. 2.2. Some experiments on the effect of a magnetic field on solubility of nickel in the PbLi alloy are described in [37]. In these experiments a container was filled with the PbLi containing a fixed quantity of dissolved nickel. After exposure at 300°C under a 10 T magnetic field over 5 days, no significant variation of the nickel solubility was observed. Nevertheless, the distribution and size of deposited nickel crystals was found to be affected. Typically, the size of crystals was larger when the magnetic field was applied. Influence of a magnetic field on the crystallization in liquid metals has not been studied intensively yet. However, in aqueous media, it has been observed that the rate of nucleation and crystal growth

can be increased or decreased if a magnetic field is applied [38-40]. We have not found any experimental data on agglomeration of deposited particles in the presence of a magnetic field.

Special tests on deposition of corrosion products in PbLi were performed in [37] for two materials: austenitic stainless steel type 316L and martensitic steel type 56T5. In the 316L steel system, deposits composed of nickel, manganese, and tin were found at temperatures below 370 °C. In the temperature range 400-500 °C, crystals mostly composed of iron and chromium were found. As it was discussed before, they were chromium-rich at lower temperatures and iron-reach at higher temperatures. No significant differences were observed between the two cases without and with a magnetic field (0.25 T). In the 56T5 steel system, different types of crystals were detected. They were found in various quantities and distributed all over the wall of the tube, the Fe/Cr ratio increased with the temperature. Strong evidences of the magnetic field effect on deposition were observed. The majority of precipitations were observed in the region inside the magnetic field, some adhering to the wall and some suspended in the PbLi. Only one type of this ferromagnetic deposit composed of Fe and Cr (92Fe-8Cr) was found. The magnetic field had no effect on the small amounts of deposits composed of Ni, Mn and Sn.

The effect of the magnetic field on corrosion rate in PbLi was studied experimentally in [9,33]. All these studies have demonstrated pronounced increase in corrosion rate in the presence of a magnetic field (up to two times). On the other hand, there are some experimental data showing no effect of a magnetic field on corrosion rate (private communication with S. Malang). This may indicate existence of various competing mechanisms of the magnetic field on corrosion, including purely hydrodynamic and kinetic effects. The influence of a magnetic field on the compatibility of 316L austenitic and 1.4914 martensitic steels with PbLi was studied in [33]. These experiments were performed at low PbLi velocities (in a thermal convection loop), significant radial thermal

gradients and short distances between hot and cold zones with (1.4 T) and without magnetic field. In the temperature range between 420 °C to 475 °C, the results show an increase of the corrosion rate of about 50% for 316L steel and 30% for 1.4914 martensitic steel. Moreover the magnetic field induces a loss of symmetry in the deposition process: the amount of recovered deposit is greater in the direction parallel to the magnetic field than in the perpendicular direction.

The corrosion of ferritic-martensitic EUROFER steel in PbLi in a strong uniform magnetic field (~2 T) was studied in the conditions of a fully developed MHD flow in a rectangular duct [9]. The exposition time in the hot PbLi at 550°C was 2000 hours. Two flow conditions were tested: at 2.5 and 5 cm/s. The experiments have revealed that the magnetic field significantly (almost twice) enhances the corrosion rate. Moreover, the effect of a magnetic field depends on its orientation with respect to the duct walls. The corroded samples at B=0 are very smooth, while the samples influenced by a magnetic field (surfaces perpendicular to the magnetic field) demonstrate wave patterns resembling grooves oriented in the melt flow direction (Fig. 2 3). At the same time surface parallel to the magnetic field still remain smooth.

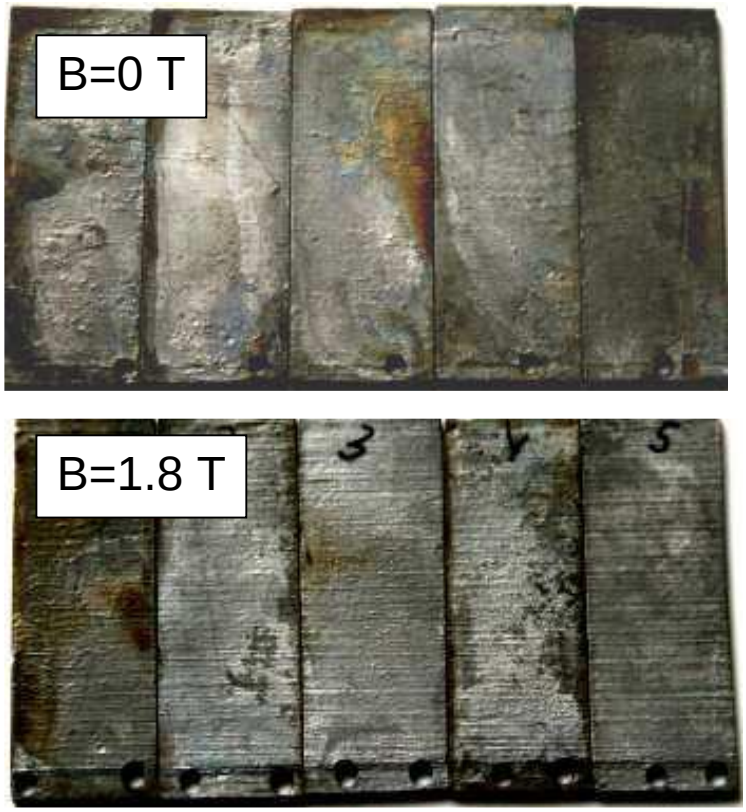

Figure.2.3: Macrostructure of the washed samples after contact with the PbLi flow [9,34].

CHAPTER 3

NEW CORRELATION FOR THE SATURATION CONCENTRATION AND ITS APPLICATION TO CORROSION IN LAMINAR MHD FLOW

3.1 Physical Model

Various experimental studies in the past [15-17,41-43] as well as more recent experimental data [9,18-20,22] have demonstrated two distinct phases in the corrosion process. First, relatively slow dissolution of the passivating oxide layer occurs, and then the corrosion rate is considerably increased due to dissolution of the main steel constituents, iron and chromium. The first phase is also known as the "incubation period". For blankets operating in a steady-state regime, the second phase is obviously more important than the incubation period.

The dissolution process in the second phase is linear in time indicating that the corrosion is uniform and the corrosion rate is constant. For this phase, metallographic examinations of the corroded samples performed in the studies cited above have not revealed any other pronounced corrosion mechanisms, such as formation of intermetallic compounds, penetration of liquid metal along grain boundaries or leaching of any particular steel constituents. This is different from the

nickel-rich austenitic steels where leaching of high-solubility nickel results in formation of a porous layer at the interface (see, *e.g.*, [17]). It should be noted that some new experimental data, nevertheless, indicate to some occurrence of other corrosion mechanisms rather than pure dissolution (see, *e.g.*, [44-45]), such as corrosion-erosion and grain/sub-grain boundary penetration. These mechanisms are not considered here. Since iron is the major ferritic/martensitic steel constituent (see Table 3.1), the considerations of corrosion processes at the interface and further transport of corrosion products with the flowing PbLi are often limited to iron only. In these conditions, the transport model can be reduced from the multi-phase flow to a one-phase flow, using a dilution approximation [46]. This approach is also accepted in the present study.

Table 3.1. Chemical composition of some ferritic/martensitic steels [9].

Steel	**C**	**Cr**	**Ni**	**Mn**	**W**	**V**	**Ta**
EUROFER	0.11	8.82	0.02	0.47	1.09	0.20	0.13
MANET I	0.13	10.6	0.87	0.82	-	0.22	-
Optifer IVa	0.11	8.50	-	0.57	1.16	0.23	0.16
F82H-mod.	0.09	7.70	-	0.16	1.95	0.16	0.02

The flow-induced corrosion processes of ferritic/martensitic steel in the PbLi involve several steps as discussed, for example, in [10]. Each step can be described with a simple mass transfer formula, which relates the mass flux of the dissolved iron with the associated concentration difference or concentration gradient. First, separation of atoms from the solid matrix into the liquid occurs due to the difference between the chemical activity (chemical potential) of a particular steel component in the solid and that in the liquid. An associated mass flux from the wall I (kg/m^{2}s) at the solid/liquid interface can be written (see, *e.g.*, [34,47]) as

$$I = k(C^s - C_w), \tag{3.1}$$

where C^s (kg/m^3) is the saturation concentration of iron in PbLi, C_w is its concentration in the LM at the interface (wall concentration), and k (m/s) is the dissolution rate constant. Second, the solute is transported due to diffusion and convection through the boundary layer in the liquid to the bulk flow, where the major transport mechanism is convection. The contribution of diffusion and convection to the transport of the dissolved material in the boundary layer can vary significantly depending on the flow conditions, such as the flow regime (laminar or turbulent), presence or absence of the magnetic field and the thickness of the concentration boundary layer compared to the thickness of the dynamic boundary layer. The diffusion-convection transport through the boundary layer is usually combined into one mass flux, which can be described with the following mass transfer equation:

$$I = K(C_w - C_b), \tag{3.2}$$

where C_b is the concentration of iron in the bulk and K (m/s) is the mass transfer coefficient. Due to mass conservation, the two fluxes are equal so that

$$I = k\ C^s - C_w\ = K(C_w - C_b) \tag{3.3}$$

The bulk concentration can be neglected in most cases compared to the wall concentration, thus

$$C_w = C^s(1 + K/k)^{-1}, \tag{3.4}$$

Eq. 3.4 shows that the wall concentration is close to the saturation concentration, providing the dissolution rate of iron in PbLi at the interface is much higher than the rate at which the dissolved iron is carried from the solid into the liquid bulk, *i.e.*, when $K/k<<1$. The last assumption has been confirmed in many experimental studies of the flow-induced corrosion of steels in lead alloys, including PbLi and PbWi (for references see, *e.g.*, [10]). In such a mass transfer controlled regime Eq. 3.4 can be simplified to

$$C_w = C^s \tag{3.5}$$

and then used as a boundary condition in the computations of the concentration field. More general third type boundary conditions can also be obtained by equating the mass fluxes:

$$D\frac{\partial C}{\partial n}\Big|_w = k\ C^s - C_w\ , \tag{3.6a}$$

$$D\frac{\partial C}{\partial n}\Big|_w = k\ C^s - C_b\ , \tag{3.6b}$$

Here, D (m^2/s) is the diffusion coefficient of iron in PbLi. Similarly to several other studies (see, *e.g.*, [28-29]), in almost all computations in the present study, first type boundary condition in the form of Eq. 3.5 has been applied.

3.2 Available Correlation for Saturation Concentration of Iron in PbLi

As seen from Eqs. 3.5 and 3.6 the saturation concentration of iron in PbLi is one of the most important parameters in the corrosion model, which needs to be specified with high enough accuracy. Although several empirical correlations are available, they suggest very different values of C^s, which vary by several orders of magnitude. All correlations have the same form of Arrhenius-type equation $C^s = e^{A-B/T}$, where T (K) is the absolute temperature, but the parameters A and B vary significantly. The data on the solubility of iron in PbLi proposed by Barker *et al*. [48] were obtained by immersion tests of pure iron in PbLi to determine the concentration of the dissolved metal in a liquid alloy using atomic absorption spectroscopy. These

experiments were carried out at different temperatures, such that an expression of variation of the iron solubility with temperature was established as follows:

$$C^s = e^{5.811172-1508.35/T} \tag{3.7}$$

Borgstedt *et al*. [41] deduced the iron solubility from dissolution tests in flowing PbLi using a certain correlation for the mass transfer coefficient and certain values for the iron diffusivity based on the Sutherland-Einstein equation. The solubility values by Borgstedt *et al.* are close to those in pure lead:

$$C^s = e^{24.7136-21517.7/T}. \tag{3.8}$$

The solubility of iron in Pb-17Li was also determined by Feuerstien *et al*. by dissolution tests in crucibles [49]. For tests done with alpha-iron the following correlation has been obtained:

$$C^s = e^{4.94-4292/T}. \tag{3.9}$$

Also a correlation for saturation concentration was proposed by Grjaznov *et al*.[47]:

$$C^s = e^{17.6562-17099/T} \tag{3.10}$$

Recently, Bucenieks *et al*. have proposed a correlation, using experimental data on the mass loss of EUROFER samples in a laminar flow with and without a magnetic field [5]:

$$C^s = e^{21.47-18000/T} \tag{3.11}$$

In all formulas in this section, the saturation concentration is in wppm. The correlations are illustrated in Fig. 3.1. Of them, one by Barker *et al*. [48] gives saturation concentration much

higher compared to others, making the difference between the lowest and highest predicted values about four orders of magnitude. Other correlations are closer to one another but the uncertainty is still unacceptably high, up to two orders of magnitude. This uncertainty significantly limits the reliability of any theoretical predictions of mass loss where these correlations are used.

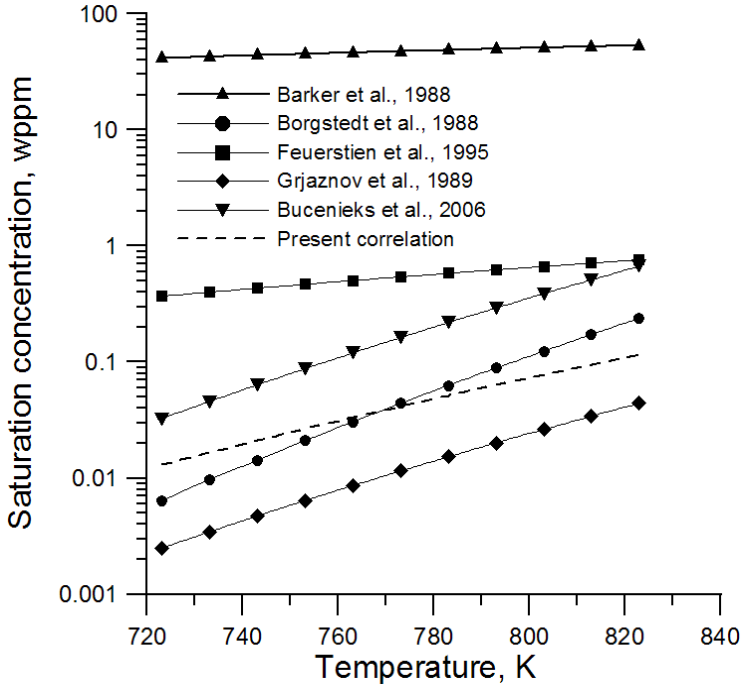

Figure 3.1: Several correlations for saturation concentration of iron in PbLi as a function of temperature, including a new correlation developed in the present study.

3.3 Mathematical Models and Numerical Codes

Three particular flow scenarios are considered and correspondingly two numerical codes are developed for: (i) turbulent hydrodynamic flow in a pipe or a plane channel with and without magnetic field, and (ii) laminar MHD flow in an electrically conducting rectangular duct. In all cases, the mathematical model includes the fluid flow equations, the energy equation and the mass transfer equation. The mass transfer equation is written in the dilution approximation, assuming all corrosion products are fully dissolved in the liquid metal.

In the case of the MHD flow in a rectangular duct, an additional induction equation is used to compute the induced magnetic field $B_x(T)$, which is further used in computations of the electromagnetic force acting on the liquid. The main assumptions of the models are discussed in section 3.1 and are also summarized here. The models deal with the flow induced corrosion, assuming uniform dissolution of iron in the flowing PbLi. The velocities are relatively low, such that the corrosion rate is mostly controlled by mass transfer processes. At high velocities, higher corrosion rates can be expected due to effect of erosion [10]. Most of the experimental studies performed in liquid metals (usually for turbulent flows) confirm that the corrosion process is controlled by mass transfer. However, the studied velocity range in these experiments is narrow, for instance in the case of PbLi flows, the maximum velocity didn't exceed 0.3 m/s. The present model can likely be applied to velocities higher than 0.3 m/s providing that erosion-corrosion doesn't occur or at least it is insignificant compared to the contribution of the dissolution mechanism. Based on these limitations, all computations for turbulent flows without a magnetic field in this study are limited to the maximum velocity of 0.3 m/s. The other parameters in the computations, the temperature and the channel size, are also comparable with those in experiments to assure model applicability. In the case of MHD flows, flow laminarization typically occurs due

to the effect of the applied magnetic field. In such MHD cases, the maximum velocity in the computations was increased to up to 1 m/s (see computations in Section 3.4.3) as erosion occurrence seems to be unlikely.

The initial iron concentration in all computations in the present study is always assumed to be zero: C=0 at x=0. In computations, the diffusion coefficient of iron in PbLi is calculated using the Sutherland-Einstein equation [9]. For example, using this equation at 550 °C, D=6.4x10^{-9} m^2/s. Other physical properties of PbLi at this temperature are density 9280 kg/m^3, kinematic viscosity 1.1x10^{-7} m^2/s and electrical conductivity 0.73x10^6 S/m. The computations are performed in the temperature range from 400 °C to 550 °C taking the temperature variations in the physical properties of PbLi into account based on the PbLi material database in [50]. The two codes have been combined into one computational package called "TRANSMAG" (TRANSport phenomena in MAGnetohydrodynamic flows). More capabilities, first of all those related to the effect of a magnetic field, will be added to TRANSMAG in the future.

3.3.1 Turbulent hydrodynamic flows

The transport model is written here in the boundary-layer approximation, which agrees well with the experimental conditions reported in almost all experimental studies, where corrosion specimens were placed inside a long host duct. In such conditions, the diffusion flux in the flow direction can be neglected compared to the convective transport in the same direction. The governing equations that utilize the boundary-layer approximation include the momentum (Eq. 3.12), continuity (Eq. 3.13), energy (Eq. 3.14), and mass transfer (Eq. 3.15) equations which are written in terms of the velocity components U and V (m/s), temperature T (K), pressure P (Pa) and iron concentration C (kg/m^3) in PbLi as follows:

$$\frac{\partial U}{\partial t}+U\frac{\partial U}{\partial x}+V\frac{\partial U}{\partial y}=-\frac{1}{\rho}\frac{\partial P}{\partial x}+\frac{1}{y^m}\frac{\partial}{\partial y}\left[y^m\left(\nu+\nu_t\right)\frac{\partial U}{\partial y}\right], \tag{3.12}$$

$$\frac{\partial U}{\partial x}+\frac{1}{y^m}\frac{\partial}{\partial y}\left[y^m V\right]=0, \tag{3.13}$$

$$\rho\, C_P\left(\frac{\partial T}{\partial t}+U\frac{\partial T}{\partial x}+V\frac{\partial T}{\partial y}\right)=\frac{1}{y^m}\frac{\partial}{\partial y}\left[y^m\left(\lambda+\lambda_t\right)\frac{\partial T}{\partial y}\right], \tag{3.14}$$

$$\frac{\partial C}{\partial t}+U\frac{\partial C}{\partial x}+V\frac{\partial C}{\partial y}=\frac{1}{y^m}\frac{\partial}{\partial y}\left[y^m\left(D+D_t\right)\frac{\partial C}{\partial y}\right]. \tag{3.15}$$

Here, t (s) is the time, x and y (m) are the coordinates along and across the flow. The integer parameter m is either 1 (plane channel) or 2 (circular pipe), ρ (kg/m^3), ν (m^2/s), λ (W/mK), and D (m^2/s) are the fluid density, kinematic viscosity, thermal conductivity and diffusion coefficient of iron in PbLi, while ν_t, λ_t and D_t are the turbulent transport properties, which are calculated using a well-known k-ε model of turbulence [51]. A numerical code that solves Eqs. 3.12-3.14 along with the transport equations for the turbulent kinetic energy k and dissipation rate ε (not shown here) was developed in [52]. A new code extends previous code [52] by solving in addition Eq. 3.15. All equations are approximated with the finite-difference formulas using a stretched grid, which clusters the grid points near the walls. To provide a proper resolution in the wall vicinity, the number of grid points across the flow is 50-200 depending on the Reynolds number, of which at least 10 points are placed within the viscous sub-layer. The solution is sought as a steady state of the original time-dependent problem using a Blottner-type finite-difference method [53].

3.3.2 Laminar flow in a rectangular duct with and without a magnetic field

The mathematical model describes coupled fluid flow, electromagnetic, and heat and mass transfer processes in laminar liquid metal MHD flows in an electrically conducting rectangular duct. Here, we assume fully developed flow conditions, so that 2D MHD equations can be used, while the heat transfer and mass transfer equations are 3D:

$$\frac{\partial^2 U}{\partial z^2}+\frac{\partial^2 U}{\partial y^2}+\frac{B_o^z}{\nu\rho\mu_0}\frac{\partial^2 B_x}{\partial z}-\frac{1}{\nu\rho}\frac{\partial P}{\partial x} \tag{3.16}$$

$$U\frac{\partial C}{\partial x}=D\left(\frac{\partial^2 C}{\partial x^2}+\frac{\partial^2 C}{\partial y^2}+\frac{\partial^2 C}{\partial z^2}\right) \tag{3.17}$$

$$\frac{1}{\mu_o}\frac{\partial}{\partial z}\left(\frac{1}{\sigma}\frac{\partial B_x}{\partial z}\right)+\frac{1}{\mu_o}\frac{\partial}{\partial y}\left(\frac{1}{\sigma}\frac{\partial B_x}{\partial y}\right)+\frac{B_o^z}{\nu\rho\mu_0}\frac{\partial U}{\partial z}=0, \tag{3.18}$$

$$\rho\, C_P U\frac{\partial T}{\partial x}=\frac{\partial}{\partial x}\left(k\frac{\partial T}{\partial x}\right)+\frac{\partial}{\partial y}\left(k\frac{\partial T}{\partial y}\right)+\frac{\partial}{\partial z}\left(k\frac{\partial T}{\partial z}\right), \tag{3.19}$$

Here, B_o^z is the applied constant (transverse) magnetic field, σ (S/m) is the electrical conductivity, and μ_0 (H/m) is the magnetic permeability of vacuum, x , y, z are axial, toroidal, and radial coordinates respectively. When solving the whole problem, the momentum Eq. 3.16 and the mass transfer Eq. 3.17 are solved in the liquid only, while the induction Eq. 3.18 and heat transfer Eq. 3.19 are integrated over the whole domain, including the conducting walls. The induced magnetic field enters the momentum equation through the flow-opposing Lorentz force term. The boundary condition on the velocity is a no-slip condition at the interface between the liquid and solid. The external boundary condition on the induced magnetic field at the interface between the duct wall

and the surrounding non-conducting medium is $B_x = 0$ to assure that the magnetic field doesn't diffuse into the outer region. .This mathematical model was previously used in computations of MHD flows, heat transfer and tritium transport in poloidal ducts of the DCLL blanket in [54] and [55].

The numerical code uses a control-volume technique based on non-uniform collocated Cartesian meshes. Both the velocity and magnetic field are defined at the center of the control-volume cell, while the fluxes are defined at the center of the cell side. The mesh is non-uniform, clustering points in the Hartmann layers at the walls perpendicular to the applied magnetic field and in the side layers at the walls parallel to the field. Typically, the total number of the mesh points in the cross-sectional area is 151 by 151, which includes about 25 points in the wall and at least 10 points within the Hartmann and side layers. The code solves finite-difference equations obtained from Eqs. 3.16 and 3.18 using the ADI (Alternative Direction Implicit) method [56] until a steady-state solution is reached. Then, the velocity distribution is used as an input data to solve the 3D mass and heat transfer equations using an explicit method.

3.4 Results and Discussion

3.4.1 Deriving new correlation for the saturation concentration

First, the code for turbulent flows described in Section 3.3.1 is applied to solve a one-parameter inverse problem to obtain a new correlation for the saturation concentration C^S of iron in PbLi by matching calculated and experimental data on corrosion of martensitic steels in the flowing PbLi. The experimental data used in this matching procedure are the corrosion rates v (μm/yr), which are summarized in [16] in the form of a semi-empirical correlation known as Sannier's equation:

$$v = 8 \times 10^9 \times Exp\left(\frac{-25690}{1.98T}\right) \times U_m^{0.875} \times D_h^{-0.125}, \mu m / yr \tag{3.20}$$

Here, T is the absolute temperature of the flowing PbLi in K, U_m is the flow velocity in m/s and D_h is the hydraulic diameter in m. This formula is based on the approximation of the experimental data obtained in [16] and also uses earlier experimental data cited in [16]. The equation is applicable to fully developed turbulent flows of PbLi. The effect of the position on the corrosion rate has also been addressed in [16]. It appears that over the major length of the hot zone where the temperature is uniform (1 m in [16]), the corrosion rate is uniform, except for a short 10-cm region at the channel inlet, where it is higher compared to the rest of the hot zone. Therefore, the formula is not applicable to the short inlet section. Some recent studies [22] have also confirmed the applicability of Sannier's equation to the temperatures as high as 550 °C.

The major steps in the solution of the suggested inverse problem are illustrated in Fig. 3.2. As a first step, the Borgstedt's correlation (Eq. 3.8) is used as an initial guess for the saturation concentration. After solving the transport problem, the calculated concentration field is used to

calculate corrosion rate ν_{cal}, which is then compared with ν_{exp} calculated with Eq. 3.22, and then C^s is adjusted to minimize the difference between ν_{cal} and ν_{exp}. This procedure is repeated several times until condition $\nu_{cal} = \nu_{exp}$ is matched. In agreement with the experimental observations, the corrosion rate computed numerically is higher over a short inlet section and then drops downstream to some value, which doesn't experience further changes with the distance. Some examples of such behavior typical to heat and mass transfer in long ducts can be seen in Fig. 3.7. This asymptotic value of the corrosion rate is used as ν_{cal}. Finally, the values of the saturation concentration that resulted in a good match between the experimental and numerical data in the reference temperature range are used to construct a new correlation for C^s versus the temperature in the form $C^s = e^{A-B/T}$.

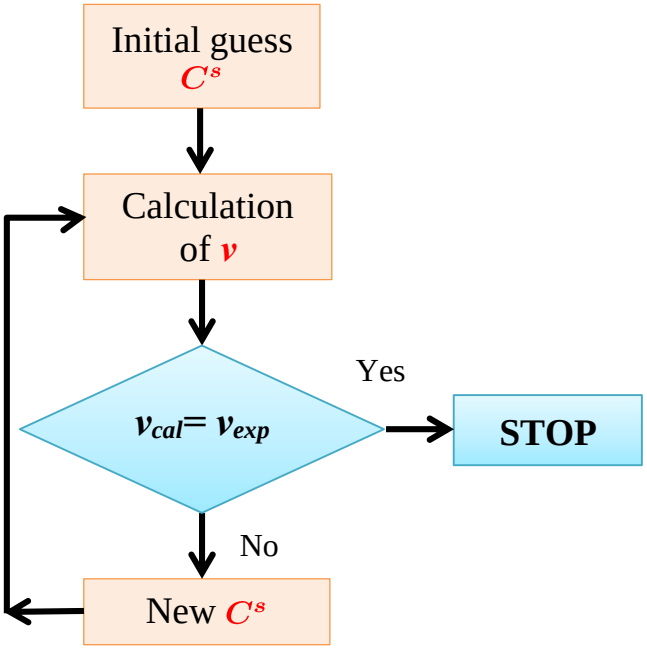

Figure 3.2: An algorithm for solving the one-parameter mass transfer problem to reconstruct the saturation concentration data from the experimental data.

In the present computations, when solving the inverse problem, the hydraulic diameter and the flow velocity are fixed to some values from the middle of the parameter range reported in the experimental studies. Namely, $D_h = 0.02$ m and $U_m = 0.11$ m/s, while the temperature is varied from 450 °C to 550 °C. The effect of D_h and U_m on corrosion is also addressed in further computations. Tuning C^s via comparisons between the computed mass losses and those from Sannier's equation as suggested in Fig. 3.1 has resulted in the following correlation:

$$C^s = e^{13.604 - 12975/T}, \tag{3.21}$$

which is also plotted in Fig. 3.1. Among all correlations plotted in this figure, the one from Borgstedt is the nearest to the new correlation. For temperatures below 500 °C the new correlation gives higher values of C^s compared to Borgstedt's correlation while for higher temperatures the new data are smaller. The correlation given by Grjaznov *et al*. is the second nearest to the new one but it predicts smaller values in the whole temperature range compared to Eq. 3.21. Fig. 3.3 shows the computed wall thinning (μm/yr) as a function of the PbLi temperature using three correlations, including the new one. The wall thinning is shown at some distance from the flow inlet where the corrosion rate is uniform to match the experimental conditions. Using either the empirical correlation for saturation concentration by Borgstedt or that by Grjaznov along with the first type boundary condition doesn't lead to a good fit with Sannier's equation. Some computations were also performed using a more general boundary condition of the third type, Eq. 3.21. In these computations the optimal values of two parameters *k* and C^s were sought to minimize the difference between the computed mass loss and that from Sannier's equation. In most of the cases, applying correlations 3.8 and 3.10 doesn't result in any reasonable match. In fact, using Borgstedt's correlation allows for the optimal values of *k* and C^s only for temperatures above 500 °C. Using both Borgstedt's correlation below 500 °C and Grijaznov's correlation in

the temperature range from 450 °C to 550 °C under predicts the corrosion rate regardless of k and C^s. In those cases where a good match was found using Borgstedt's correlation, the wall concentration was observed to be close to the saturation concentration with a maximum difference of about 20%. These observations are in fact indirect evidences in favor of the first type boundary condition.

The new correlation is then used in the computations of the mass transfer problem to calculate the wall thinning as a function of the velocity (Fig. 3.4), which is the second most important parameter in corrosion processes. Similarly to Fig. 3.3 the data in Fig. 3.4 are shown for the flow section far from the inlet where the corrosion rate is uniform. As seen from this figure, there is a good match between the computed values and those from Sannier's equation. A good match with Sannier's equation has also been confirmed in the whole range of the parameters (velocity and channel dimension) where this equation is valid, demonstrating a maximum difference of only a few percents.

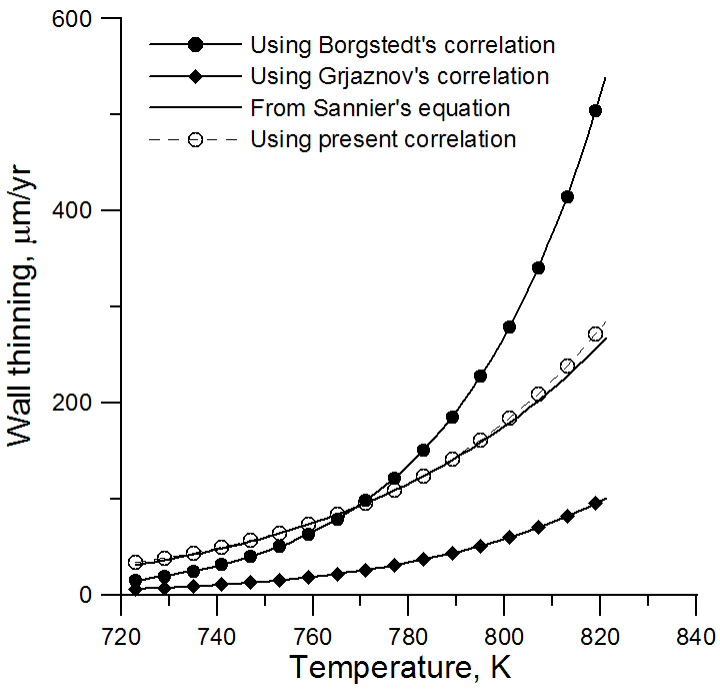

Figure 3.3: The wall thinning versus temperature with 3 correlations for the saturation concentration, including the present one, Eq. 3.21, at U_m=0.11 m/s, D_h=0.02 m.

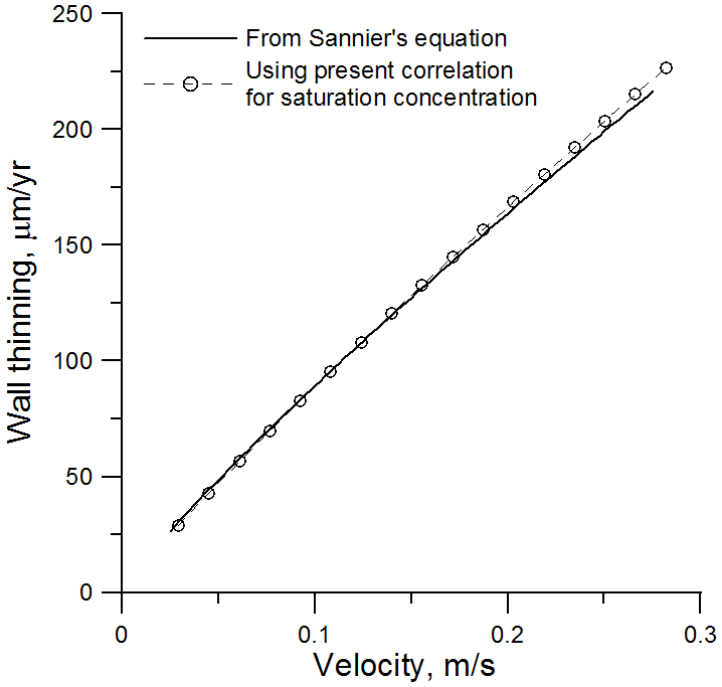

Figure 3.4: Wall thinning as a function of velocity at T=500°C, D_h=0.02 m compared to Sannier's equation. The present correlation for saturation concentration, Eq. 3.21, is used.

3.4.2 Laminar flows in a rectangular duct. Effect of a magnetic field

The velocity profile is computed first as described in Section 3.3.2 and then the velocity data are used as input data for the mass transfer code to solve the mass transfer problem applying the new correlation for the saturation concentration (Eq. 3.21) as a boundary condition. The main goal of these computations is to address the effect of the magnetic field on the wall thinning. To do this, fully developed flow of PbLi at 500 °C was considered in a conducting rectangular duct made of RAFM steel with the cross-sectional dimensions $2b$=$2a$=2 cm, length L=1 m and the wall thickness t_w=1 mm. The applied transverse magnetic field B_o^z is varied from zero to 6 T. This corresponds to $(Ha = B_0 b \sqrt{\sigma/(\nu\rho)})$ up to 1325. Notice that the Hartmann number is the dimensionless

strength of the magnetic field. On the other hand, in magnetohydrodynamics, *Ha* is considered as a similarity number such that the Hartmann number squared is the ratio between the electromagnetic (Lorentz) force and the viscous force [57]. In MHD duct flows, the Hartmann number can also be used to characterize the thickness of the MHD boundary layers. The MHD boundary layer at the duct walls perpendicular to the magnetic field, known as the Hartmann layer, has a thickness scaling as 1/*Ha*, while the boundary layer at the walls parallel to the magnetic field (side or Shercliff layer) scales in thickness as $1/\sqrt{Ha}$.

Within the MHD boundary layers, the velocity varies exponentially with the distance. The sharp velocity gradients in the MHD boundary layers can be responsible for intensification of transport processes in the liquid compared to purely hydrodynamic flows, where boundary layers are much thicker and the velocity gradients are correspondingly smaller. Three velocities are considered here: U_m=1, 2 and 3 cm/s, such that the maximum hydrodynamic Reynolds number ($Re = U_m 2a/\nu$) is 5580. This choice of parameters is typical for the conditions in corrosion experiments and also assures that the flow is laminar as it typically is under blanket conditions (not counting for possible quasi-2D turbulence). In addition to *Ha* and *Re*, the third dimensionless parameter in this problem is the wall conductance ratio $c_w = t_w\sigma_w/(b\sigma)$=0.2.

The computed velocity profiles (Fig. 3.5) demonstrate Hartmann layers and formation of high-velocity jets at the side walls, where the flow-opposing Lorentz force is smaller compared to that in the core flow. In this core bounded by the Hartmann layers and the jets, the flow is almost uniform. The peak velocity in the jets is known to scale with the Hartmann number as $\sqrt{Ha}$, while the core velocity, as seen in the figure, is close to the mean bulk velocity. In the figure, the velocity is scaled by the bulk velocity U_m. Such a velocity structure has strong impact on the corrosion processes. One can see a strong effect of the magnetic field on the mean bulk concentration (Fig.

3.6). The higher the magnetic field, the more wall material is dissolved in the flowing liquid. It is obvious that the observed increase in the mass loss with the magnetic field is related to the sharp velocity gradients and high-velocity jets. More detailed analysis of the corrosion mass loss (Fig. 3.7) shows that the side walls are more affected by corrosion than the Hartmann walls. This difference can be explained by significant differences in the velocity distribution in the near-wall region between the two walls as seen in Fig. 3.5.

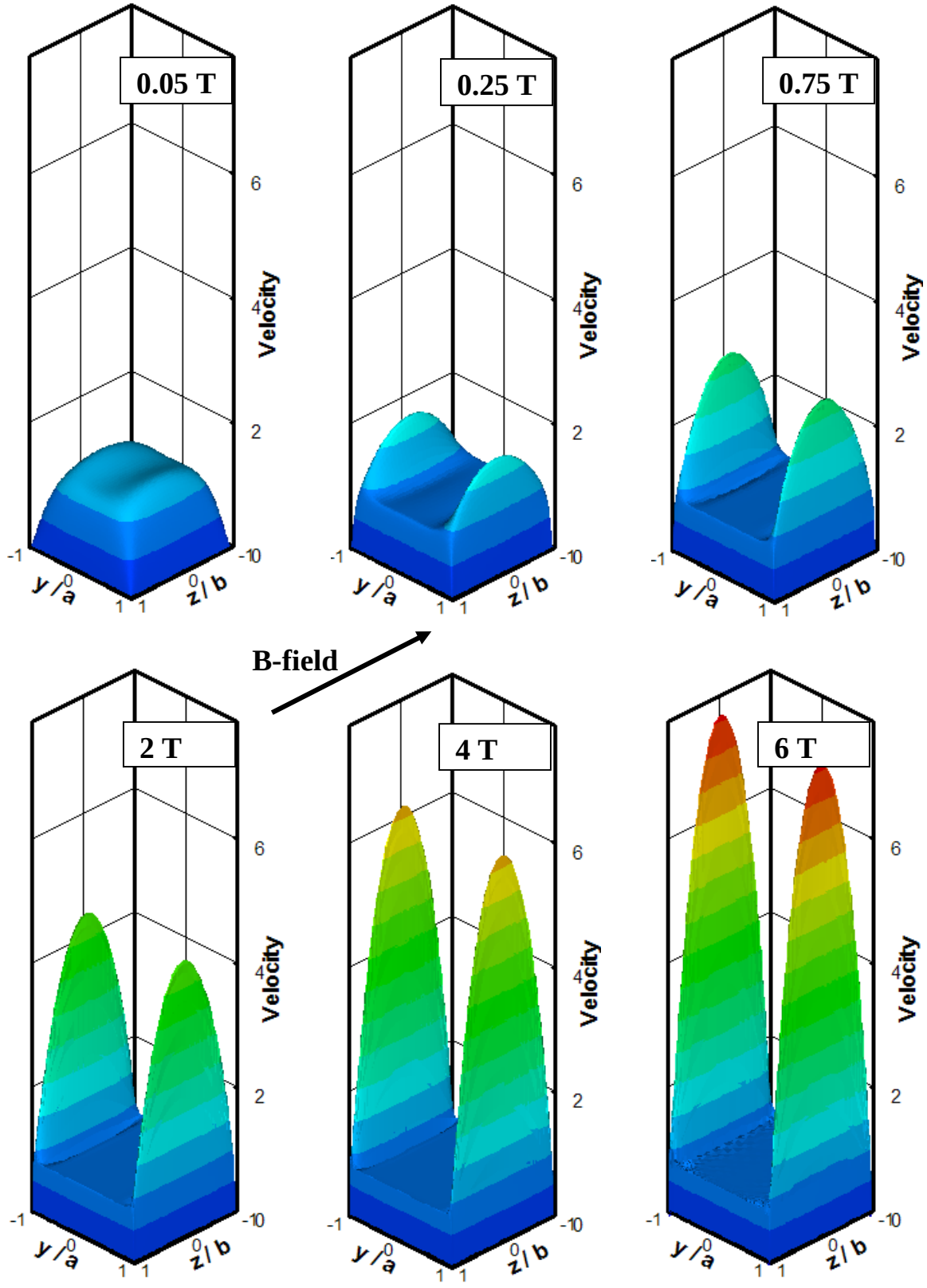

Figure 3.5: Effect of the magnetic field on the velocity profile in the reference fully developed MHD flow of PbLi in a square duct at c_w=0.2. *Ha* changes from 13 to 1325.

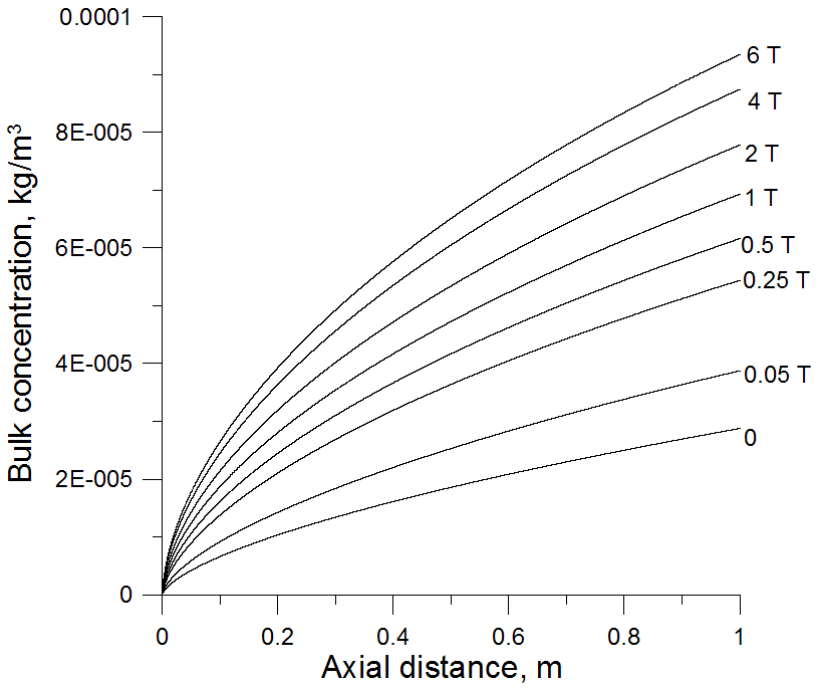

Figure 3.6: Increase in the bulk concentration with the axial distance for magnetic fields from 0 to 6 T in the reference MHD flow in a square duct at U_m=1 cm/s.

Although the Hartmann layer exhibits higher velocity gradients, the side layer has a higher velocity associated with the near-wall jet. For both walls, large changes in the wall thinning occur within the inlet section of the duct, which varies in length from several centimeters to about half a meter as the magnetic field is increased. Further downstream, variations in the wall thinning are insignificant. The difference in the mass loss between the Hartmann and the side wall is also illustrated in Fig. 3.8, where the wall thinning at the end of the 1 m duct section is shown as a function of the magnetic field. The mass loss from the Hartmann wall first increases with the field and then saturates at relatively small B_o^z of about 0.2-0.3 T, while the mass loss from the side wall continues to increase with the magnetic field. As a result, the difference in the wall thinning between the two walls increases continuously with the magnetic field up to 3 times at 6 T. To

better understand the observed differences in the wall thinning between the Hartmann and the side walls, more computations are plotted in Figs. 3.9 and 3.10. Fig. 3.9 shows the development of the concentration field along with the thickness of the concentration boundary layer at the Hartmann wall as the liquid proceeds downstream. This thickness is defined using a criterion based on a 1% difference between the local concentration in the liquid and that at the interface. Fig. 3.10 shows the development of the concentration boundary layer at both the Hartmann and side walls for several values of the applied magnetic field. The thicknesses of the MHD boundary layers are also shown in this figure for $B_o^z = 0.1$ T. One can see that the increase in the magnetic field results in thinning the concentration boundary layer at the side wall. As for the Hartmann wall, the effect of the magnetic field on the thickness of the concentration boundary layer is opposite. However the magnetic field has a very weak effect on the thickness of the concentration boundary layer at the Hartmann wall except for small values of B_o^z around 0.1-0.2 T.

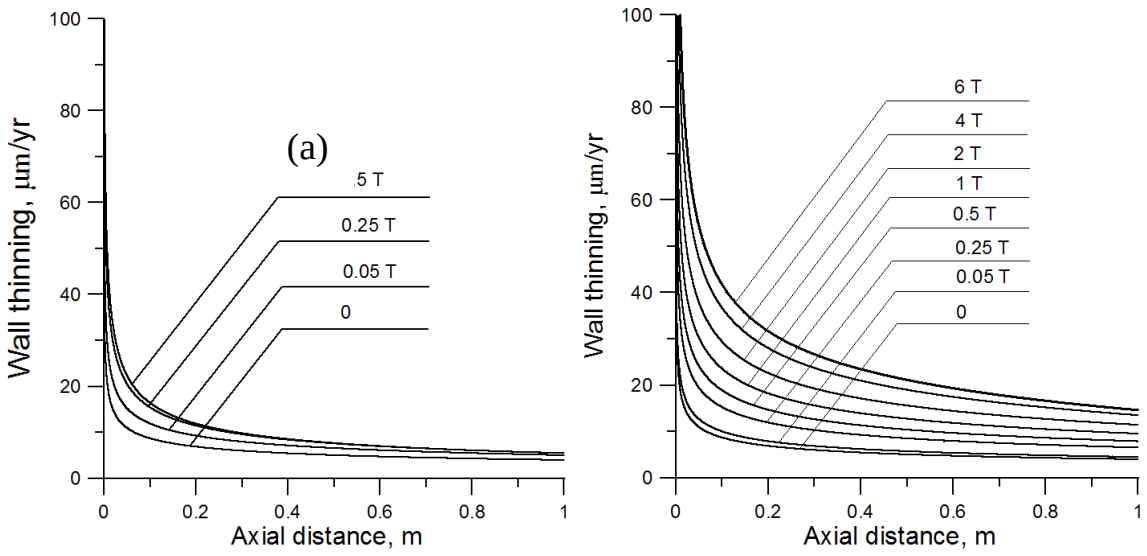

Figure 3.7: Wall thinning with the axial distance in the reference MHD flow in a square duct for: (a) Hartmann wall and (b) side wall at U_m=1 cm/s.

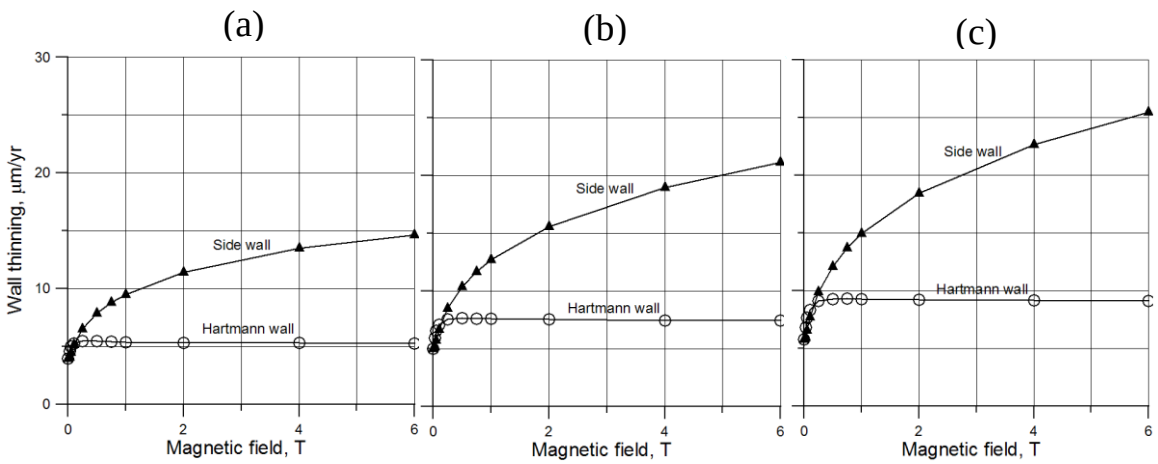

Figure 3.8: Difference in the wall thinning at the end of the 1-m section between the Hartmann and the side wall in the reference MHD square duct flow at: (a) 1 cm/s, (b) 2 cm/s and (c) 3 cm/s.

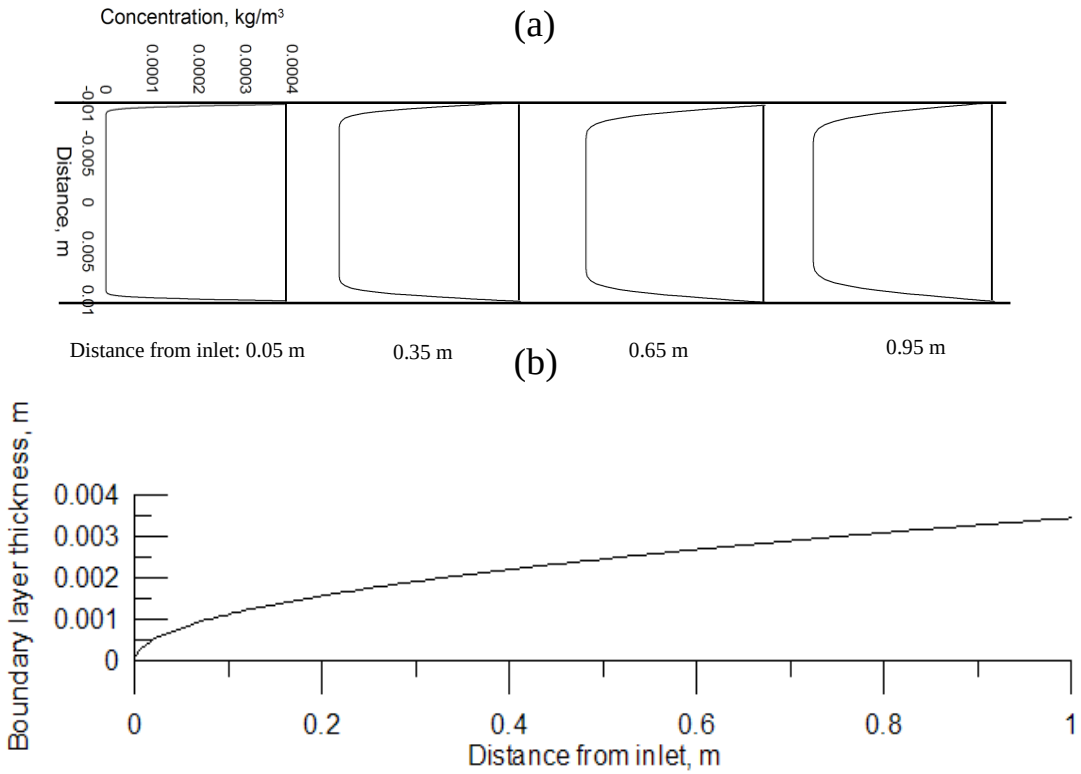

Figure 3.9: Concentration field in the reference MHD flow in a square duct at U_m=1 cm/s and B_o^z =1 T: (a) concentration profiles in the duct mid-plane y=0 parallel to the magnetic field and (b) thickness of the concentration boundary layer at the Hartmann wall.

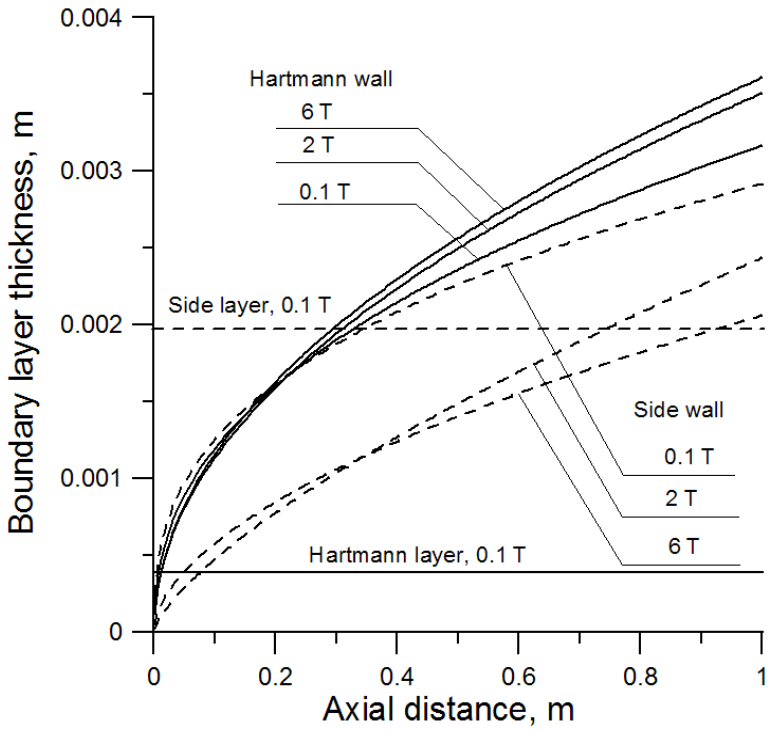

Figure 3.10: Thickness of the concentration boundary layer as a function of the axial distance in the reference MHD flow in a square duct at the Hartmann and the side wall at U_m=1 cm/s.

It is noticeable that the concentration boundary layer at the Hartmann wall is much thicker (except for the short inlet section of the duct) than the Hartmann layer. The last observation explains why the mass loss at the Hartmann wall saturates with the magnetic field as demonstrated in Fig. 3.8. The concentration boundary layer at the side wall is thinner than that at the Hartmann wall but it is comparable in thickness with its counterpart MHD boundary layer. That is why unlike the Hartmann wall no mass loss saturation at the side wall occurs as the magnetic field is increased. One more difference from the Hartmann wall is that the thickness of the concentration boundary layer at the side wall decreases as the magnetic field is increased.

It should be noticed that the present model doesn't capture some minor effects, such as formation of grooves at the Hartmann walls as reported in [5], which seem to be related to unsteady three-dimensional phenomena in the MHD flows as analyzed in [58].

3.4.3 Laminar flows in a rectangular duct in a strong magnetic field. Effects of temperature and velocity

In addition to the effect of the magnetic field on the mass loss, the effect of the temperature and the flow velocity in a rectangular duct, providing a strong magnetic field is applied was considered. As far as is known, this is the first time such an analysis was done. In all previous studies the magnetic field was not considered and/or the temperature and the flow velocity were not varied. The reference duct has dimensions $2b$=$2a$=20 cm, L=2 m and t_w=5 mm. The applied transverse magnetic field is 5 T, which matches the toroidal magnetic field in the outboard region of a fusion reactor. The associated Hartmann number is 13,230 and the wall conductance ratio is 0.1. These parameters are relevant to self-cooled blanket conditions. It should be noted that a self-cooled PbLi blanket concept was considered in the past and found promising (see, *e.g.*, [59]), however, currently DCLL and HCLL (Helium-Cooled Lead-Lithium [60]) blanket concepts receive more attention. The flow conditions in these two blankets are different from the self-cooled blanket such that special analysis of the corrosion processes may be needed for them. In particular, in the DCLL blanket, most of the corrosion processes occurs in poloidal flows in a thin gap between the SiC FCI and the host steel duct.

In the present analysis, the velocity and the temperature are used as parameters and varied from 0.1 m/s to 1 m/s and from 400 °C to 550 °C, correspondingly. The computational procedure is similar to that in the previous section. The computed velocity profile has distinguished high-

velocity jets at the side walls similar to Fig. 3.5. All conclusions on the effect of a magnetic field made in the previous section also apply to the reference flow. The results for the wall thinning averaged over the duct length as $L^{-1}\int_0^L v(x)dx$ are plotted in Figs. 3.11 and 3.12 separately for the Hartmann wall and for the side wall. The side wall thinning is always higher compared to the Hartmann wall. As seen from the figures, the difference is typically about 2 times. Fig. 3.11 illustrates the effect of the temperature. As expected, the wall thinning varies exponentially as the temperature is increased. At a velocity of 0.5 m/s the value of 20 μm/yr is exceeded if the temperature is higher than 430 °C. The effect of the velocity at 500 °C is illustrated in Fig. 3.12. As seen from this figure, the wall thinning increases with the velocity as a power function, *i.e.*, the velocity has a weaker effect on corrosion of both the Hartmann wall and the side wall compared to the temperature. However the velocity effect is still significant. The increase in the velocity from 0.2 m/s to 1 m/s results in doubling the mass loss. These observations suggest scaling laws for the mass loss: $ML \sim e^{pT}U_m^q B_0^s$ for the side wall, and $ML \sim e^{pT}U_m^q$ for the Hartmann wall, where $q, s \sim 0.5$.

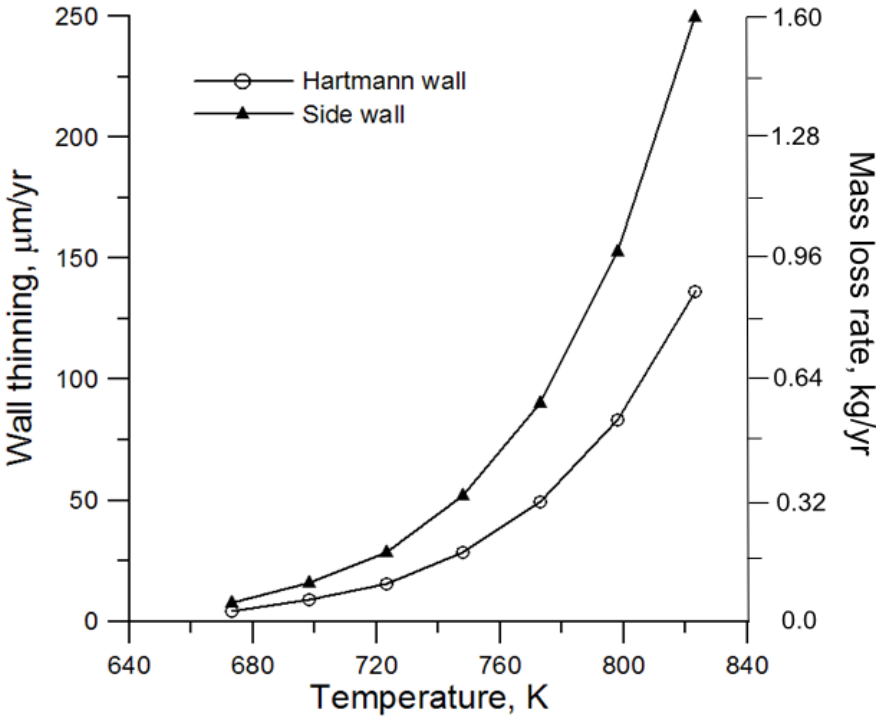

Figure 3.11: Effect of the temperature on wall thinning averaged over the duct length L at U_m=0.5 m/s. Other parameters are given in the text.

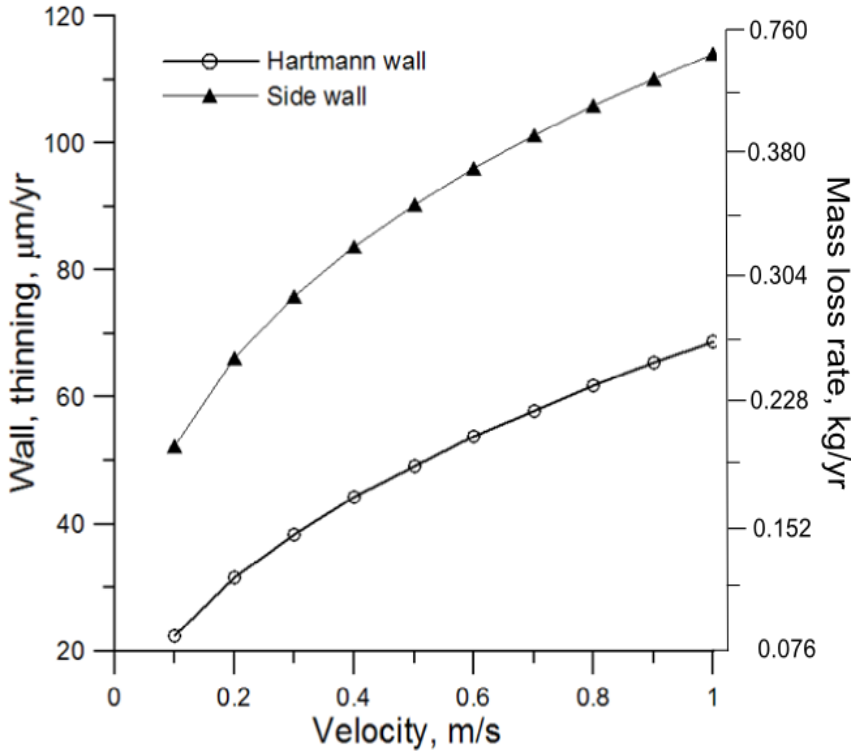

Figure 3.12: Effect of the velocity on the wall thinning averaged over the duct length L at T=500 °C. Other parameters are given in the text.

3.5 Concluding Remarks

Acomputationalsuite called TRANSMAG (TRANSport phenomena in MAGnetohydrodynamic flows) has been developed to address mass transfer processes associated with corrosion of ferritic/martensitic, in particular RAFM, steels in the flowing eutectic alloy PbLi with and without a magnetic field. The new tool combines two numerical codes: (i) turbulent hydrodynamic flows in a pipe or a plane channel, and (ii) laminar MHD flows in an electrically conducting rectangular duct. First, computations were performed to solve a one-parameter inverse mass transfer problem to reconstruct saturation concentration data from the experimental results on corrosion rates in turbulent flows without a magnetic field. These data are then approximated with a new correlation, Eq. 3.21, which gives the saturation concentration of iron in PbLi as a function of the temperature of the liquid in the form of the Arrhenius-like equation. Using this correlation in computations of corrosion processes has resulted in fair prediction of the wall mass loss for a wide range of flow parameters. The applicability of this correlation has been demonstrated in the temperature range from 450 °C to 550 °C. A good match with the experimental data also suggests the adequacy of the proposed model assumptions, including: mass transfer controlled regime, dilution approximation, one-phase flow and eventually the first type boundary condition in the form of Eq. 3.5.

Second, the new correlation was used to analyze mass losses in laminar fully developed rectangular duct flows in the presence of a transverse magnetic field. It was found that the corrosion rate under the effect of a strong magnetic field can be a few times higher compared to pure hydrodynamic flows. However, the computations have revealed significant differences in the corrosion behavior between the Hartmann and the side walls. Namely, the side walls are more affected by the corrosion attack due to formation of high-velocity jets in the flow. The observed

differences in the mass loss between these two walls are up to 2-3 times. In both cases, the mass loss increases with the magnetic field. However, the mass loss from the Hartmann wall first increases and then saturates, while the mass loss from the side wall is always increasing. This behavior has been explained by the difference in the thickness of the concentration boundary layer at the Hartmann and side walls. In the case of the Hartmann walls, the thickness of the Hartmann boundary layer is smaller than that of the concentration boundary layer, while in the case of the side walls both boundary layers are comparable in thickness. The observed differences in the corrosion behavior between the Hartmann and side walls suggest that in MHD rectangular duct flows, most of the mass loss occurs from the side walls, whereas all experimental studies [5,34-35] have focused on the Hartmann walls.

In another set of computations for laminar flows in a rectangular duct, the effects of the flow velocity and the temperature were analyzed under conditions of a strong, 5 T, transverse magnetic field. For a 0.5-m/s flow in a 2-m long, 20-cm by 20-cm square duct, the wall thinning increases exponentially from 5 to 140 μm/yr for the Hartmann wall and from 8 to 250 μm/yr for the side wall as the temperature is increased from 400° to 550 °C. This analysis suggests scaling laws for the mass loss in rectangular ducts in the form: $ML \sim e^{pT} U_m^q B_0^s$ for the side wall, and $ML \sim e^{pT} U_m^q$ for the Hartmann wall, where q, $s \sim 0.5$.

The observations made on the effect of a magnetic field on corrosion rate in laminar MHD flows in a rectangular duct are in good qualitative agreement with the experimental data obtained at the Institute of Physics, Latvia (Riga experiment) [5,34-35]. Namely, the increase of the corrosion rate by factor of 2-3 when the magnetic field is applied and much higher corrosion rates at the inlet section can be seen in both experimental and present numerical data. Quantitative comparisons with the experimental data demonstrate, however, significant differences (up to 50%)

even for hydrodynamic flows, always showing smaller corrosion rates in computations. These differences may indicate some mismatch between the modeling assumptions and experimental conditions. Taking into account that the available experimental data on corrosion in MHD flows are very limited, and the flow measurements and detailed comparison between the PbLi composition before and after the experiment in these studies were not done, it is difficult to explain these differences. Therefore, more experimental studies of MHD flow induced corrosion and comparisons with modeling predictions seem to be necessary in the future.

CHAPTER 4

SELF-SIMILAR SOLUTION FOR THE CORROSION PROBLEM FOR HARTMANN FLOW

4.1 Introduction

In the previous study of corrosion [section 3.4.2], computations were performed for MHD laminar flows in a rectangular duct with thin conducting walls made of RAFM steel. It was found that corrosion is qualitatively and quantitatively very different between the Hartmann walls of the duct (walls perpendicular to the applied magnetic field) and the side walls (walls parallel to the applied magnetic field) because of significant differences in the velocity profile. Namely, at the side walls, the corrosion rate is higher. Here, the corrosion rate always increases with the Hartmann number due to formation of high-velocity jets, whose peak scales as $\sqrt{Ha}$.

At the Hartmann walls, the corrosion rate first increases and then doesn't change as the Hartmann number is increased. As noticed in [section 3.4.2], this effect is related to the fact that for high enough Hartmann numbers, the Hartmann layer thickness becomes smaller (or much smaller) than the thickness of the concentration boundary layer over the major duct length, so that the resistance of the thin Hartmann layer to diffusion becomes negligibly small compared to that of a much thicker concentration boundary layer. The thickness of the Hartmann layer δ_{Ha} in a

strong magnetic field is $\delta_{Ha} = b/Ha$. The concentration boundary layer thickness δ_C can also be affected by the Hartmann number and by other parameters such as the Reynolds number and the Schmidt number: $\delta_C = \delta_C(Ha, Re, Sc)$. Therefore the effect of a magnetic field on corrosion can be studied indirectly by comparing b/Ha with. $\delta_C(Ha, \mathrm{Re}, Sc)$. To do this comparison, an analytical solution for $\delta_C(Ha, \mathrm{Re}, Sc)$ is required. In this study such a solution was derived and then corrosion analysis was completed for the case of the Hartmann flow (the flow between two parallel walls in a wall-normal magnetic field).

4.2 Analytical Solution

The mass transfer problem for corrosion in a 1D flow between two parallel walls is described with the following mass transfer equation, which is written here in dimensionless form:

$$\tilde{U}(\tilde{z})\frac{\partial \tilde{C}}{\partial \tilde{x}} = \frac{1}{Pe_D}\frac{\partial^2 \tilde{C}}{\partial \tilde{z}^2}. \tag{4.1}$$

In this equation, the velocity is scaled with the mean bulk velocity: $\tilde{U} = U/U_m$. The dimensionless concentration is written using the inlet concentration C_0 and the saturation concentration C^S as follows: $\tilde{C} = \frac{C - C_0}{C^s - C_0}$. The axial coordinate x and the cross coordinate z are scaled using half of the width of the channel b: $\tilde{x} = x/b$, $\tilde{z} = z/b$. The Peclet number for diffusion is $Pe_D = Re \times Sc = U_m b/D$. The initial condition at the inlet is $\tilde{C} = 0$. The boundary condition at the walls $\tilde{z} = 0;2$ is $\tilde{C} = 1$. The velocity profile is the Hartmann velocity profile:

$$\tilde{U}(\tilde{z}) = \frac{Ha}{Ha - \tanh(Ha)}\left[1 - \frac{\cosh[Ha \times (\tilde{z} - 1)]}{\cosh(Ha)}\right]. \quad (4.2)$$

For Ha>>1 and $0 \le \tilde{z} \le 2$,

$$\tilde{U}(\tilde{z}) = 1 - e^{-Ha \times \tilde{z}}. \quad (4.3)$$

Solving this mass transfer problem with the velocity profile Eqs. 4.2 or 4.3 analytically can be difficult. However, there are two particular cases (see Fig. 4.1) when the analytical solution can be found. The first particular case corresponds to the initial section of the boundary layer where the Hartmann layer is thicker (or much thicker) then the concentration boundary layer (Zone I in Fig. 4.1). Here, within the boundary layer, the velocity profile can be written as a linear function of $\tilde{z}$: $\tilde{U}(\tilde{z}) = Ha \times \tilde{z}$. The second particular case corresponds to the section of the boundary layer, where the concentration boundary layer is thicker than the Hartmann layer (Zone III in Fig. 4.1). In the Zone III, the velocity profile can be approximated as $\tilde{U}(\tilde{z}) = 1$. In the Zone II, which is located between the Zone I and III, the thickness of the concentration boundary layer is comparable with the thickness of the Hartmann layer so that neither $\tilde{U}(\tilde{z}) = Ha \times \tilde{z}$ nor $\tilde{U}(\tilde{z}) = 1$ can be used. In this Zone II, the full formula for the velocity profile Eq. 4.2 or Eq. 4.3 should be applied.

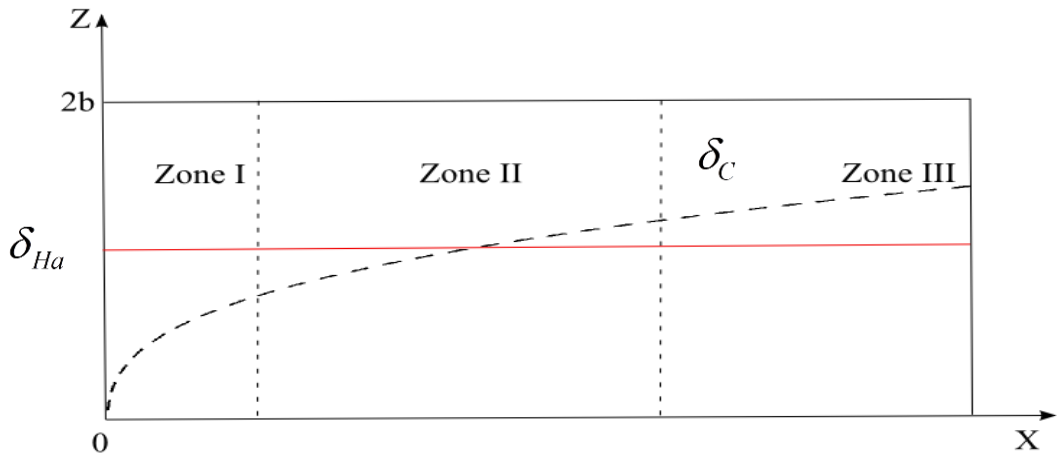

Figure 4.1: Development of concentration boundary layer in the reference corrosion problem. There are three characteristic zones. Zone I: concentration boundary layer is thinner than the Hartmann layer. Zone II: concentration boundary layer thickness and that of the Hartmann layer are close. Zone III: Concentration boundary layer is thicker than the Hartmann layer.

The new dimensionless coordinates was introduced: $\xi = x/b$ and $\eta = z/\delta_C$. As a matter of fact the axial coordinate ξ coincides with $\tilde{x}$. Using the new coordinates, the original mass transfer problem in the Zone I near the Hartmann wall can be rewritten as follows:

$$\ddot{\tilde{C}} + Pe_D Ha(\tilde{\delta}_C^2 \tilde{\delta}_C')\eta^2 \dot{\tilde{C}} = 0, \tag{4.4}$$

$$\eta = 0: \ \tilde{C} = 1, \tag{4.5}$$

$$\eta = 1: \ \tilde{C} = 0. \tag{4.6}$$

Here, the upper "dot" symbol is used for the η derivative, while symbol "prime" is used for ξ derivative.

The boundary condition Eq. 4.6 suggests that at the outer boundary of the concentration boundary layer the concentration is equal to that in the channel inlet. Eqs. 4.4-4.6 allows for a self-similar solution independent of the axial coordinate ξ providing

$$Pe_D \times Ha \times \tilde{\delta}_C^2 \tilde{\delta}_C' = Const_1 . \tag{4.7}$$

Solving Eq. 4.7 gives a formula for the thickness of the concentration boundary layer in Zone I:

$$\tilde{\delta}_C(\xi) = Const_1^{1/3} \left(\frac{3\xi}{PeHa} \right)^{1/3} . \tag{4.8}$$

The concentration profile in Zone I obtained by integration of Eq. 4.4 , is

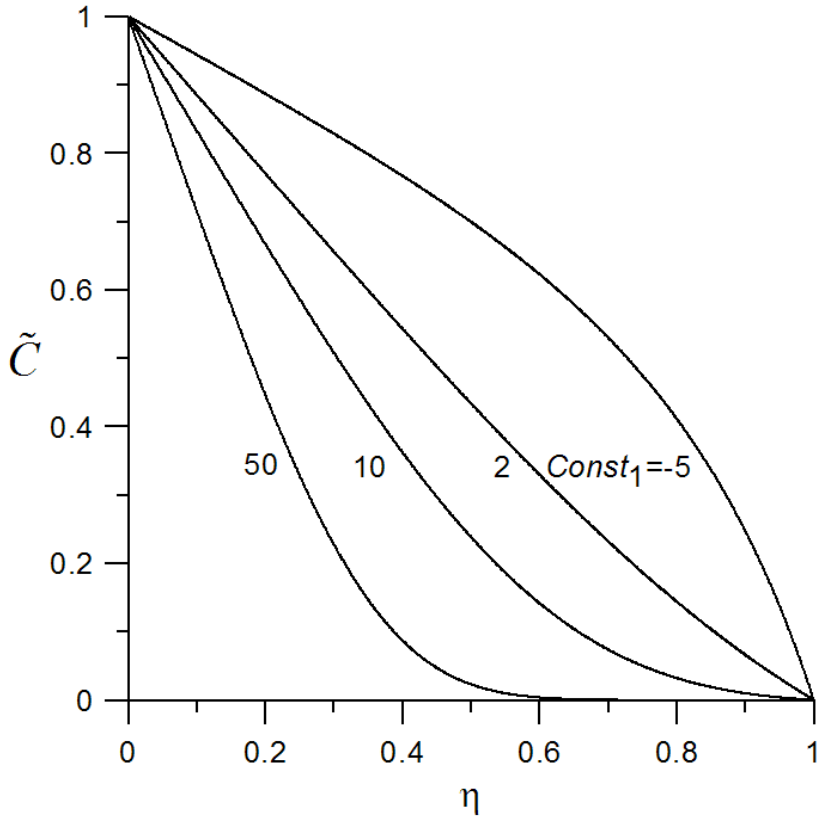

Figure 4.2: Concentration profile in Zone I computed from Eq. 4.9 for several $Const_1$.

$$\tilde{C}(\eta) = -\frac{\eta^2\Gamma\left(\frac{1}{3},\frac{Const_1}{3}\right) - \frac{\Gamma\left(\frac{1}{3},\frac{Const_1\eta^3}{3}\right)\left(Const_1\eta^3\right)^{2/3}}{const_1^{2/3}}}{\eta^2\Gamma\left(\frac{1}{3}\right) - \eta^2\Gamma\left(\frac{1}{3},\frac{Const_1}{3}\right)} \quad . \tag{4.9}$$

where $\Gamma(a)$ is Gamma function and $\Gamma(a,b)$ is incomplete gamma function.

The constant $Const_1$ entering Eq. 4.9 needs to be defined. Fig. 4.2 shows the concentration profiles computed for several $Const_1$ from -5 to 50. As seen from the figure, at $Const_1$ of -5, 2 and 50 the concentration profiles do not look realistic. The "right" value of the constant was found to be 10, which provides expected asymptotic behavior of the concentration profile near the edge of the boundary layer. This concentration profile obtained analytically is compared with the numerical computations based on the solution of Eq. 4.1 in Fig. 4.3. In the numerical computations, the thickness of the boundary layer was defined using a 1% criterion (*i.e.* at the edge of the boundary layer the concentration is 1% of the saturation concentration). A good agreement between the analytical and numerical data confirms the adequacy of the analytical approach.

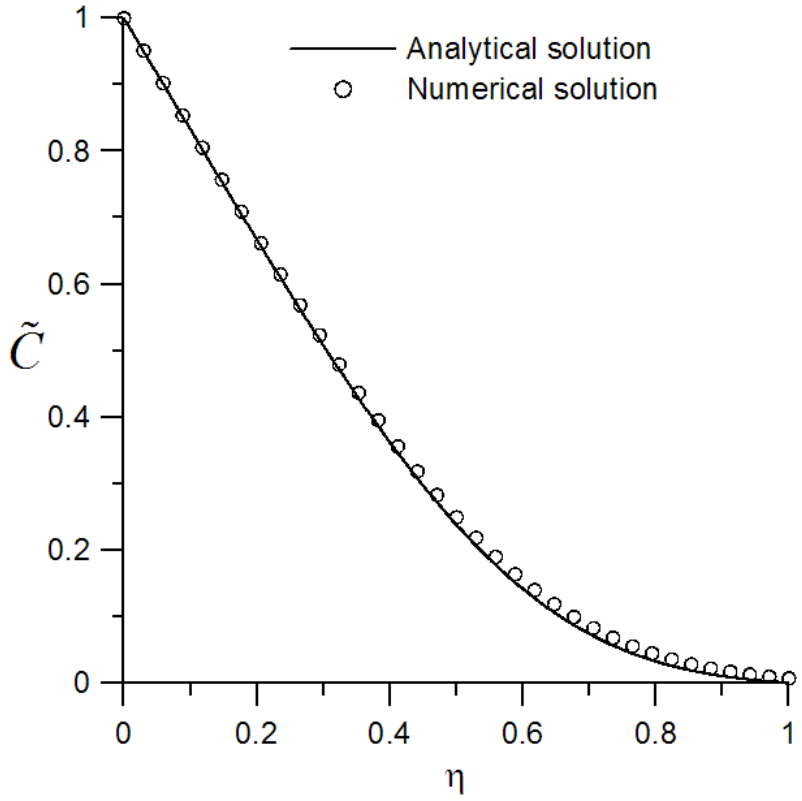

Figure 4.3: Comparison between analytical and numerical solution for Zone I. In numerical computations of the concentration field, Ha=50, Pe_D=10^8, ξ =100.

More comparisons between the analytical and numerical data are shown in Fig. 4.4 for the thickness of the concentration boundary layer. These comparisons also demonstrate a very good match between the two approaches.

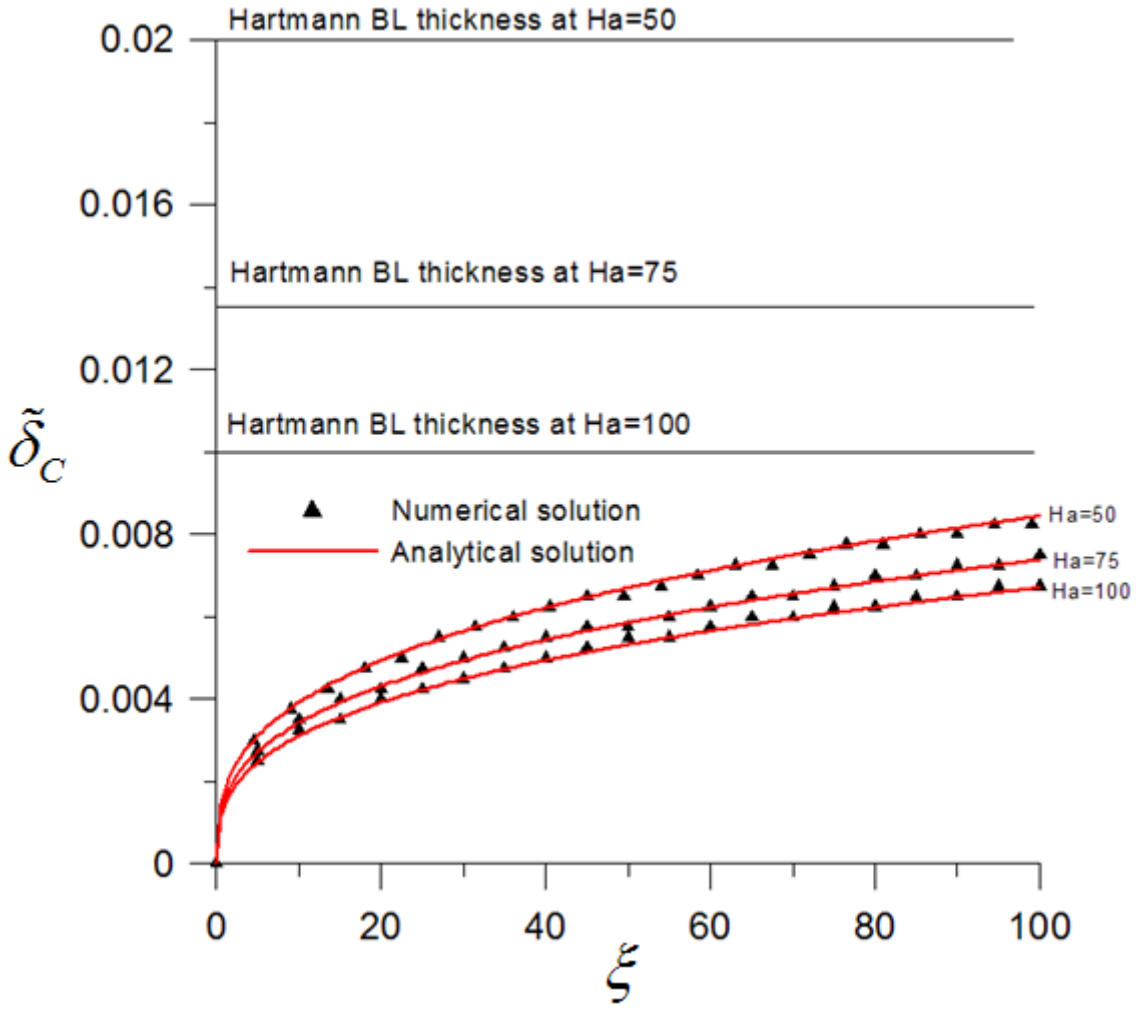

Figure 4.4: Comparison for the thickness of the boundary layer in the Zone I between analytical and numerical solutions at $Pe_D = 10^8$.

Similar analysis has been performed for the Zone III where the Hartmann layer is thinner than the concentration boundary layer. Taking into account that in the Zone III the velocity profile can be approximated as $\tilde{U}=1$, the mass transfer problem includes the following equation and boundary conditions:

$$\ddot{\tilde{C}}+Pe_D(\tilde{\delta}_C\tilde{\delta}'_C)\eta\dot{\tilde{C}}=0,$$
$$\eta=0:\ \tilde{C}=1,$$
$$\eta=1:\ \tilde{C}=0. \qquad (4.10)$$

A self-similar solution for this problem is possible providing

$$Pe_D\times\tilde{\delta}_C\tilde{\delta}'_C=Const_3. \qquad (4.11)$$

Integrating Eq. 4.11 with respect to ξ from ξ_0 to ξ results in the following formula for the thickness of the concentration boundary layer in the Zone III:

$$\tilde{\delta}_C(\xi)=\sqrt{\tilde{\delta}_C^2(\xi_0)+\frac{2Const_3}{Pe_D}(\xi-\xi_0)}. \qquad (4.12)$$

Once condition (4.11) is satisfied, the self-similar solution for problem (4.10) can be found as follows:

$$\tilde{C}(\eta)=1-\frac{erf\left(\frac{\sqrt{Const_3}\eta}{\sqrt{2}}\right)}{erf\left(\frac{\sqrt{Const_3}}{\sqrt{2}}\right)} \qquad (4.13)$$

where *erf* stands for error function.

In formulas (4.12) and (4.13), $Const_3$ and ξ_0 and $\tilde{\delta}_C(\xi_0)$ need to be defined. The constant was found in the same way as described above for the Zone I. The numerical value of this constant is $Const_3$=11. The two other parameters can be found from the numerical solution. The coordinate ξ_0 was chosen such that $\tilde{\delta}_C(\xi_0)=1/Ha$, *i.e.* at $\xi=\xi_0$ the thickness of the concentration boundary layer is equal to the Hartmann layer thickness.

Consequently, mass transfer rate expresses as *J* (kg m^{-2}s^{-1}):

$$J = k\left(C^s - C^b\right) = -D\frac{\partial C}{\partial z} \tag{4.14}$$

with C^s being the saturation concentration (kg m^{-3}) at the wall which was derived in section 3.4.1 , and C^b is the bulk concentration (kg m^{-3}) which is $C^b = 0$ since the finite duct length was considered where the concentration boundary layer is much thinner than the duct dimension. k is mass transfer coefficient (m s^{-1}). Mass transfer rate can also be expressed in a dimensionless form by the Sherwood number

$$Sh = \frac{k2b}{D} = -2\frac{\partial \tilde{C}}{\partial \tilde{z}}\bigg|_{\tilde{z}=0} \tag{4.15}$$

where $\frac{\partial \tilde{C}}{\partial \tilde{z}}$ for zone I is:

$$\frac{\partial \tilde{C}}{\partial \tilde{z}}\bigg|_{\tilde{z}=0} = \frac{\partial}{\partial \eta}\left(\tilde{C}(\eta)\right)\bigg|_{\eta=0}\frac{\partial \eta}{\partial \tilde{z}} = -\frac{3^{2/3}\sqrt[3]{Const_1}}{\Gamma\left(\frac{1}{3}\right)-\Gamma\left(\frac{1}{3},\frac{Const_1}{3}\right)}\left(\tilde{\delta}_c\right)^{-1} \tag{4.16}$$

And for zone III is:

$$\left.\frac{\partial \tilde{C}}{\partial \tilde{z}}\right|_{\tilde{z}=0} = \frac{\partial}{\partial \eta}\left(\tilde{C}(\eta)\right)\Big|_{\eta=0} \frac{\partial \eta}{\partial \tilde{z}} = -\frac{\sqrt{\frac{2}{\pi}}\sqrt{Const_3}}{erf\left(\frac{\sqrt{Const_3}}{\sqrt{2}}\right)}\left(\tilde{\delta}_c\right)^{-1} \tag{4.17}$$

The analytical solution for *Sh* for Zone I is attained by evaluating Eq. 4.8 using the value obtained for $Const_1$ and substituting the result in to Eq. 4.16. The resulting expression for *Sh* is:

$$Sh = \frac{2\times 3^{2/3}}{\Gamma\left(\frac{1}{3}\right) - \Gamma\left(\frac{1}{3}, \frac{10}{3}\right)}\left(\frac{3\xi}{Pe_D Ha}\right)^{-1/3} \tag{4.18}$$

and for Zone III after substituting the value obtained for $Const_3$ and Eq. 4.12 for the concentration thickness, the *Sh* is:

$$Sh = \frac{2\sqrt{\frac{22}{\pi}}}{erf\left(\sqrt{\frac{11}{2}}\right)}\left(\tilde{\delta}_C^2(\zeta_0) + \frac{22}{Pe_D}(\zeta - \zeta_0)\right)^{-1/2} \tag{4.19}$$

Fig. 4.5 illustrates the comparison between the obtained solution for *Sh* for Zone I and the numerical results. The results are in great agreement. Fig. 4.6 illustrates the obtained solutions for the Zones I to III. In the Zones I and III, there is a very good agreement between the analytical solution and the numerical computations. In the Zone II, both analytical solutions start deviating from the numerical data.

Eq. 4.8 can be used to estimate the dimensionless coordinate ξ_* where the concentration boundary layer and the Hartmann layer are of the same thickness:

$$\xi_* = \frac{Pe_D}{30Ha}\,. \tag{4.20}$$

Correspondingly, for $\xi < \xi_*$ the concentration boundary layer is thinner and for $\xi > \xi_*$ thicker than the Hartmann layer. It is useful to calculate ξ_* for PbLi blankets and then compare it with the blanket length. Based on this comparison one can decide what sections of the entire blanket length should be treated as Zone I, II or III.

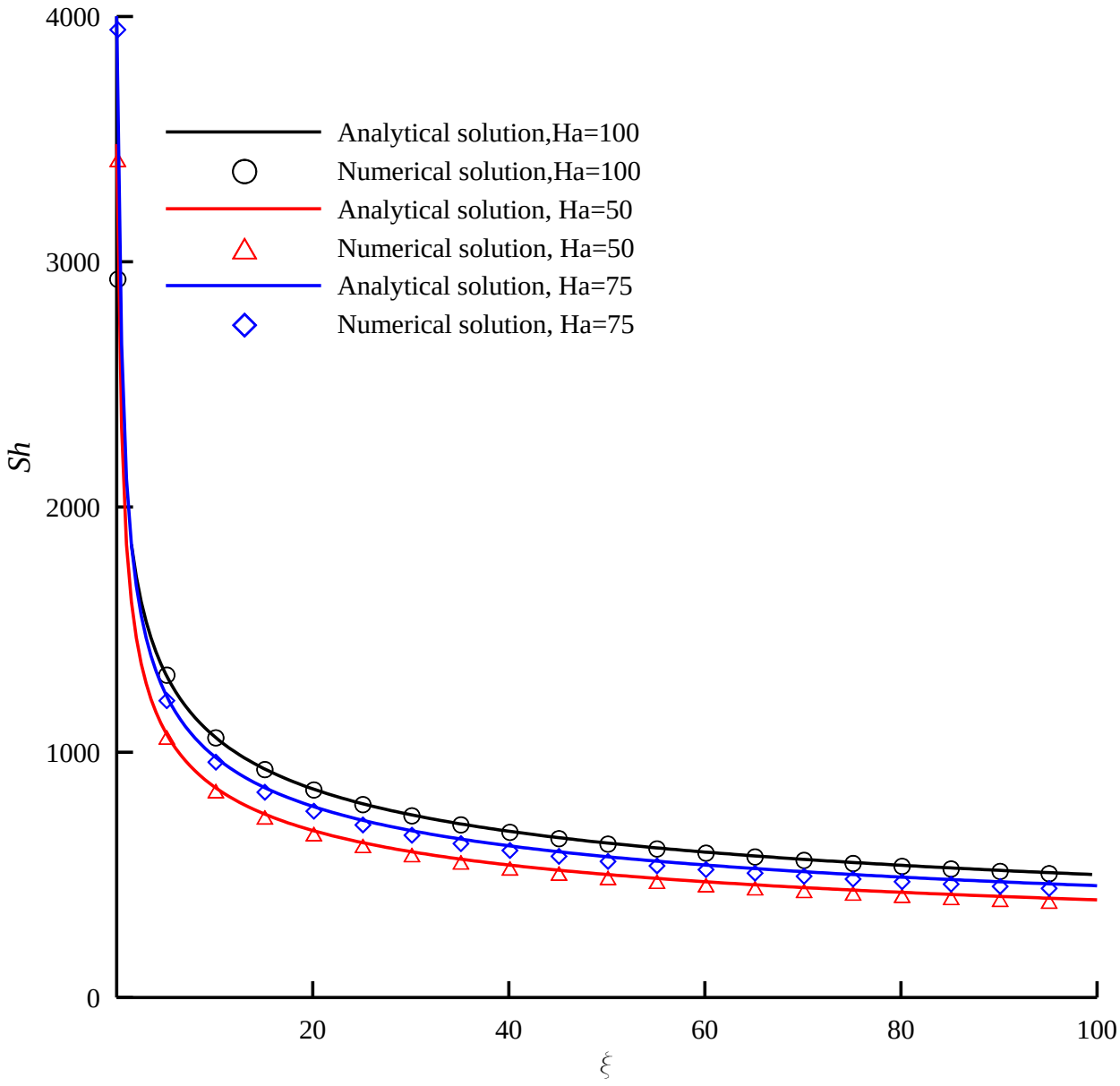

Figure 4.5: Comparison between the numerical solution and the analytical solutions for *Sh* for Zone I for *Ha*=50,75,100, $Pe_D=10^8$.

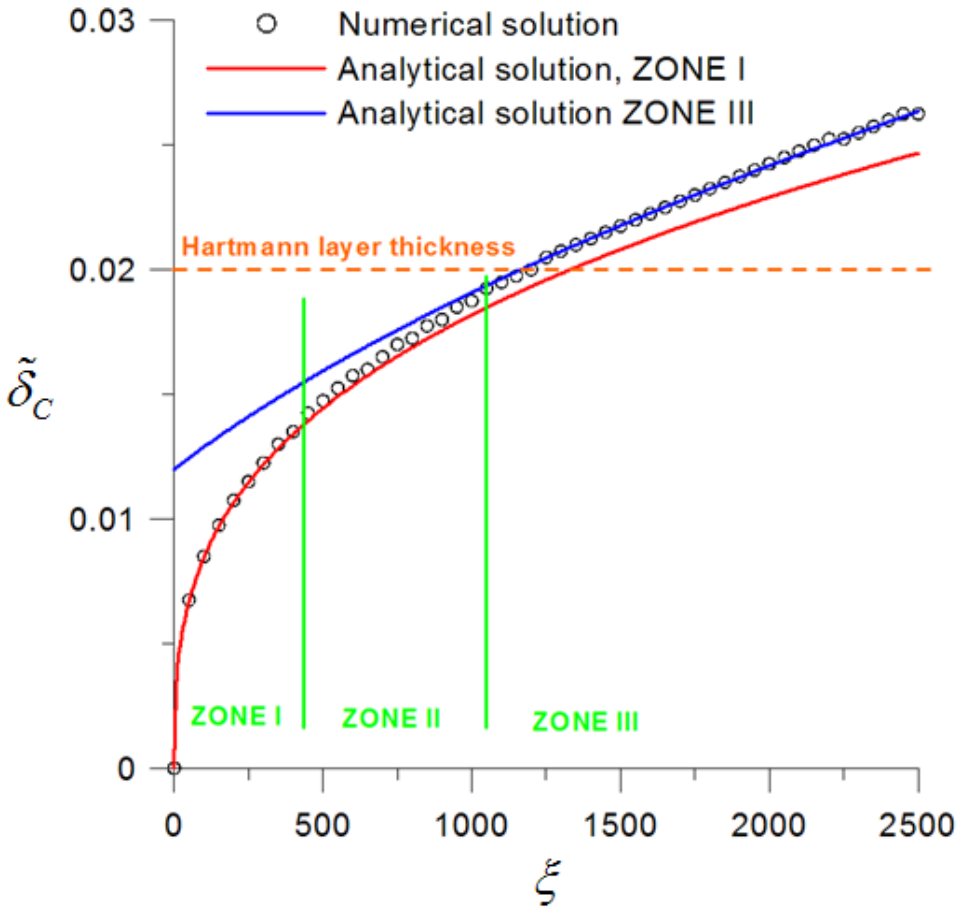

Figure 4.6: Comparison between the numerical solution and the analytical solutions for Zones I and III for Ha=50, Pe_D=10^8.

4.3 Application to a PbLi Blanket

The obtained solutions can be applied to conditions of a PbLi blanket. Two types of PbLi blankets are of interest here. In a self-cooled PbLi (SCLL) blanket [29], the liquid metal flows perpendicular to the lines of the plasma-confining (toroidal) magnetic field in long rectangular ducts. The cross-sectional dimension of such a duct is about 0.2 m (b=0.1 m). The length of a PbLi blanket duct is assumed to be 2 m. The PbLi velocity can be in the range from 0.4 to about 1 m/s depending on the blanket operation parameters. To avoid corrosion problems, the PbLi temperature is typically limited to about 470 °C. In such flows, formation of Hartmann layers occurs at the duct walls perpendicular to the toroidal magnetic field.

In a dual-coolant PbLi (DCLL) blanket, corrosion occurs in the thin ~ 2-mm gap between the structural wall and the SiC flow channel insert. The corrosion processes in the gaps perpendicular to the magnetic field can be analyzed using the present theory since the PbLi flow in such a gap is of the Hartmann type. Here, due to a very small gap width and strong flow opposing electromagnetic forces, the velocities are very small, on the order of 1 mm/s. The maximum temperature of PbLi in the DCLL blanket at the interface between the structural wall and the flowing PbLi in the gap is also restricted to about 470 °Cto guarantee that the corrosion losses are not too high.

The relevant dimensionless parameters, which enter the analytical solution (Hartmann number, Peclet number for diffusion and the dimensionless duct length L/b) along with the dimensionless length ξ_*, for these two PbLi blanket concepts are summarized in Table 4.1. Two blanket scenarios are considered: an inboard (IB) blanket at magnetic field of 10 T and outboard (OB) blanket at 4 T. The physical properties of PbLi used in evaluation of the flow parameters were taken at 500 °C.

Table 4.1. Evaluation of ξ_* for DCLL and SCLL blankets.

Parameter	SCLL IB (B=10 T)	SCLL OB (B=4 T)	DCLL IB (B=10 T)	DCLL OB (B=4 T)
Ha	26500	10600	265	106
Pe_D	(6-15) 10^6	(6-15) 10^6	150	150
L/b	20	20	2000	2000
ξ_*	7.5-18.9	18.9-47.2	0.02	0.03

As seen from the table, in the conditions of the DCLL blanket $\xi_* << L/b$ such that over almost entire blanket length the concentration boundary layer at the Hartmann wall is thicker than the Hartmann layer except for a very short length at the blanket inlet. Therefore the entire blanket should be considered as Zone III. An opposite tendency can be observed for the SCLL OB blanket, where $\xi_* \geq L/b$ such that the concentration boundary layer is always thinner than the Hartmann layer. The entire blanket can be treated as Zone I. In the case of the SCLL IB blanket, the concentration boundary layer is first thinner and then thicker than the Hartmann layer. For the lower velocity range, the transition occurs closer to the blanket inlet, while for the higher velocity range such transition can be observed close to the blanket outlet. Therefore all three zones I, II and III can be present over the SCLL IB blanket length.

CHAPTER 5

NUMERICAL STUDY OF THE EFFECT OF A MAGNETIC FIELD ON CORROSION OF FERRITIC/MARTENSITIC STEEL IN A TURBULENT PbLi FLOW

5.1 Introduction

It is well known from experiments that the corrosion rate of RAFM steels in purely hydrodynamic turbulent PbLi flows is higher compared to laminar flows. This trend is however not so obvious if a magnetic field is applied, since the turbulence properties and associated flow dynamics, as well as the temperature distribution in the flowing liquid metal, can be strongly modified due to magnetohydrodynamic (MHD) [61-63]. Gardner [61] examined the influence of a transverse magnetic field on the structure of a turbulent flow of mercury and observed that the turbulence intensity decreased to a laminar level over a broad range of Reynolds numbers and magnetic fields. He also reported that the influence of a transverse magnetic field on heat transfer was to inhibit the convective mechanism in the field direction through damping of the turbulent velocity fluctuations, resulting in up to a 70% reduction in Nusselt number. Also, the results from studies in [64] show that the influence of the transverse magnetic field on turbulent heat transfer is to suppress the temperature fluctuations and to steepen the mean temperature gradient in the direction parallel to the magnetic field in the near-wall region.

In addition to heat transfer, mass transfer associated with corrosion is another important transport process in liquid metals, but these two phenomena are not necessarily similar as in the analogy well established for hydrodynamic flows [46]. In contrast to the studies of the effect of a magnetic field on the flow and heat transfer in liquid metals, there have been very few experimental attempts to study liquid metal corrosion of steels in the presence of a magnetic field [13]. The obtained characteristics of mass transfer processes in MHD flows are nevertheless not identical to those for heat transfer. In fact, with the magnetic field some experimental data suggest increase in the corrosion rate while others demonstrate a decrease [5,65-66].

The effect of a magnetic field on liquid metal corrosion was studied in experiments [65] using 316L and 1.4914 steels in facilities called CELIMENE and ALCESTE, which were designed to account for special features of the water-cooled PbLi blanket. The test section was placed in a homogeneous 1.4-T magnetic field, perpendicular to the module axis. It was concluded that the corrosion mechanism is a uniform dissolution of the steel matrix by PbLi, and this mechanism is not changed when a magnetic field is applied. However, the corrosion rate in the presence of a magnetic field was found to be higher compared to that obtained in the absence of a magnetic field. Similar observations were made in the experimental studies of corrosion of EUROFER samples [5], where an increase in the corrosion rate by more than a factor of two was found at the Hartmann walls (walls perpendicular to the magnetic field) of a rectangular duct when a 1.7-T magnetic field was applied. Even higher corrosion rates caused by the effect of a magnetic field were predicted in numerical computations in [67] for the side walls (walls parallel to the applied magnetic field) of a rectangular duct due to formation of near-wall high-velocity jets.

An opposite tendency (reduction of the corrosion rate as the magnetic field is applied) was observed in experimental studies in [66], where samples made of 316L austenitic steel were

exposed to hot PbLi at 480 ^{o}C in a cylindrical cavity with a rotating disk. The morphology and the nature of the corrosion layer in conditions with and without a magnetic field in these experiments were similar. However, the corrosion layer thickness on the specimen tested under a magnetic field was thinner than the one developed on the specimen tested without a magnetic field. As explained in [66], this is due to the fact that the turbulent bulk flow dominated by radial and axial velocity components when a magnetic field is not applied, and it is significantly reduced under a magnetic field. As a result, the mass transfer rate becomes much smaller than that in the case without a magnetic field.

Considering these opposite tendencies with regard to the effect of a magnetic field on the corrosion rate, it is evident that extrapolation of the present experimental data to fusion blanket conditions without a careful examination of the effect of a magnetic field on the flow structure and heat and mass transfer may result in misleading estimates for corrosion of structural materials in a blanket. The contradicting conclusions about the effect of a magnetic field on the corrosion rate seem to be related to the lack of analysis of the relation between the MHD flow (primarily turbulence effects in the PbLi flow) and mass transfer. That is why the main goal of this study is to address the corrosion phenomena under the influence of a magnetic field in turbulent flows of PbLi in conditions (geometry, velocity, temperature) similar to those in the experiments.

The study focuses on MHD turbulent flows of PbLi in a channel with a magnetic field applied in one of three directions with respect to the main flow (Fig. 5.1): wall-normal, spanwise, and streamwise magnetic fields. After proper modification of the turbulent code [52], it is applied here to investigate the effect of a magnetic field strength and its direction on corrosion processes. The computed results are then analyzed in view of turbulence modification by a magnetic field and formation of the Hartmann boundary layers.

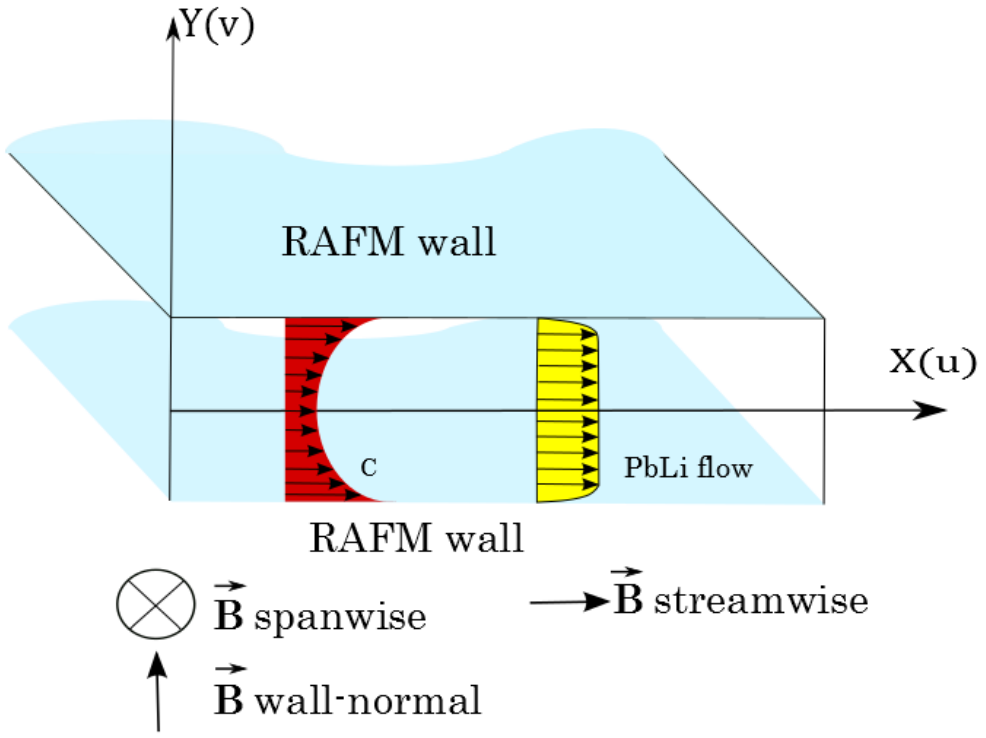

Figure 5.1: To the formulation of the problem. MHD PbLi flow between two RAFM walls in a magnetic field. Three orientations of the magnetic field are considered: wall-normal, streamwise and spanwise.

5.2 Mathematical Model and Computational Code

The mass transfer model used in this study, which describes corrosion of RAFM steel and transport of corrosion products in flowing PbLi in the presence of a magnetic field is adopted from [67]. The main assumptions of this model are the following. First, it is assumed that the principal corrosion mechanism is uniform dissolution of the steel matrix by the flowing PbLi. Second, the corrosion processes are controlled by mass transport of corrosion products across the turbulent boundary layer at the solid-liquid interface. Third, the corrosion products dissolved in the liquid metal consist mostly of iron, which is the main component of RAFM steels. Fourth, all corrosion products are fully dissolved in the liquid metal. It is also assumed that the PbLi alloy does not contain any significant amounts of metallic or other impurities or dissolved gasses that may affect the corrosion mechanism. These assumptions allow for only one mass transfer equation for concentration of dissolved iron C written in the dilution approximation and for implementation of the first type boundary condition at the interface, where the concentration of iron in the PbLi at the solid-liquid interface is taken to be its saturation concentration C^s.

The corresponding mathematical model for corrosion transport processes in MHD flows in a channel (Fig. 5.1) is based on the boundary-layer approximation, which agrees well with the experimental conditions reported in almost all experimental studies, where corrosion specimens were placed inside a long host duct. In such conditions, the diffusion flux in the flow direction can be neglected compared to the convective transport in the same direction. Then the RANS (Reynolds-averaged Navier-Stokes) equations that govern the problem include the momentum Eq. 5.1, continuity Eq. 5.2, energy Eq. 5.3 and mass transfer Eq. 5.4 equations written in terms of the averaged velocity components U and V, temperature T, pressure P and concentration C as follows:

$$\frac{\partial U}{\partial t}+U\frac{\partial U}{\partial x}+V\frac{\partial U}{\partial y}=-\frac{1}{\rho}\frac{\partial p}{\partial x}+\frac{\partial}{\partial y}\left[\left(\nu+\nu_t\right)\frac{\partial U}{\partial y}\right]+\frac{1}{\rho}f_{em} \quad , \tag{5.1}$$

$$\frac{\partial U}{\partial x}+\frac{\partial V}{\partial y}=0, \tag{5.2}$$

$$\rho C_p\left(\frac{\partial T}{\partial t}+U\frac{\partial T}{\partial x}+V\frac{\partial T}{\partial y}\right)=\frac{\partial}{\partial y}\left[\left(k+k_t\right)\frac{\partial T}{\partial y}\right], \tag{5.3}$$

$$\frac{\partial C}{\partial t}+U\frac{\partial C}{\partial x}+V\frac{\partial C}{\partial y}=\frac{\partial}{\partial y}\left[\left(D+D_t\right)\frac{\partial C}{\partial y}\right] \quad . \tag{5.4}$$

The third term f_{em} on the RHS of the momentum equation (5.1) is the mean Lorentz force (see [52]):

$$f_{em}=\begin{cases}0 & \text{spanwise or streamwise magnetic field,}\\ -\sigma B_0{}^2(U-U_m) & \text{wall-normal magnetic field.}\end{cases}$$

In the above equations, t is the time, x and y are the coordinates along and across the flow, while ρ, ν, k, σ, and D are the fluid density, kinematic viscosity, thermal conductivity, electrical conductivity and diffusion coefficient of iron in PbLi. The counterpart turbulent transport properties are ν_t, k_t, and D_t. They are calculated using a special form of the K-ε model of turbulence, which takes into account MHD effects of turbulence suppression by a magnetic field implemented for all three reference directions of the applied magnetic field [52]. The mean PbLi velocity in the channel is U_m, while B_0 is the strength of the applied magnetic field.

The boundary condition on the concentration of iron at the material interface is of the first type, $C_w=C^s$. The iron concentration at the flow inlet in all computations in the present study is always assumed to be zero: $C=0$ at $x=0$. The diffusion coefficient of iron in PbLi is calculated using the Sutherland-Einstein equation [68]. For example at 550 ºC, $D=6.4\times10^{-9}$ m^2/s. Other

physical properties of PbLi at this temperature are density 9280 kg/m^3, kinematic viscosity 1.1×10^{-7} m^2/s, and electrical conductivity 0.73×10^6 S/m. The computations are performed in the temperature range from 400 ^{o}C to 550 ^{o}C taking the temperature variations in the physical properties of PbLi into account based on the PbLi material database in [69]. The correlation for saturation concentration is taken from the study in chapter 3 as follows: $C^s = e^{13.604-12975/T}$. In this formula, the saturation concentration is in wppm and the temperature T is in K.

A numerical code TRANSMAG, which solves Eqs. 5.1-5-4 along with the transport equation for the turbulent kinetic energy K and dissipation rate ε (not shown here), was developed in [52]. In the code, the low-Reynolds number variant of the K-ε model is used to provide accurate results when integrating through the viscous sub-layer. The details of the low-Reynolds number model are given in [52]. The effect of the magnetic field in each of the three cases of the magnetic field orientation are introduced via specially adjusted model coefficients in equations for K and ε. All equations are approximated with the finite-difference formulas using a stretched grid, which clusters the grid points near the walls. To provide a proper resolution in the wall vicinity, the number of grid points across the flow is 50-200 depending on the Reynolds number, of which at least 10 points are placed within the viscous sub-layer. The solution is sought as a steady state of the original time-dependent problem using a Blottner-type finite-difference method [53].

5.3 Characterization of the Effect of a Magnetic Field on the Flow

It is most likely that a strong magnetic field affects corrosion indirectly by modifying the flow near the material interface. One of the most important MHD effects in the liquid metal, which seems to modify corrosion significantly, is laminarization of the originally turbulent flow by a magnetic field, caused by dissipation losses in the flow due to induced electric currents and associated Joule heating. Based on the experimental data [70], laminarization in MHD channel flows occurs if $Ha/Re > (Ha/Re)_{cr}$, where the Hartmann number, $Ha = B_0 h\sqrt{\sigma/(\nu\rho)}$, and the hydrodynamic Reynolds number, $Re = U_m h/\nu$, are constructed using the channel half-width *h*. A strong enough external magnetic field suppresses the turbulent fluctuations in the liquid metal regardless of the magnetic field orientation. As summarized in [70], $(Ha/Re)_{cr} = 2.5\times10^{-2}$ for a streamwise magnetic field, 4.5×10^{-3} for a wall-normal magnetic field, and 8.0×10^{-3} for a spanwise magnetic field. As seen from Fig. 5.2, present computations confirm flow laminarization and accurately predict the transition to a laminar regime. They also match the experimental data well for the friction coefficient C_f as a function of the Ha/Re parameter, showing first some decrease in the friction coefficient as Ha/Re is increased and then an increase in C_f due to formation of the Hartmann layers.

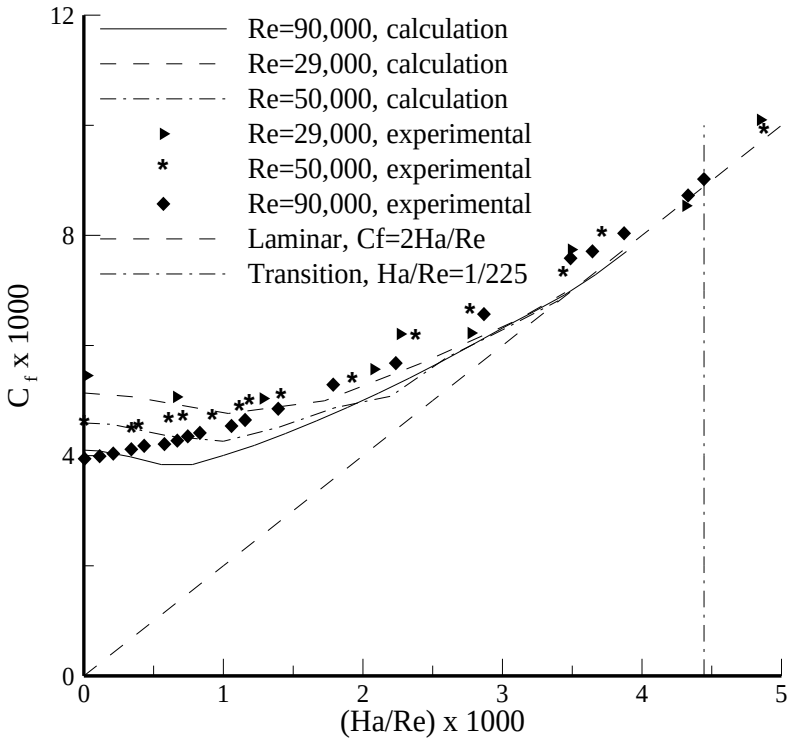

Figure 5.2: Experimental [70] and computed friction factor for a wall-normal magnetic field.

Although a magnetic field leads to turbulence suppression in all three cases, the degree and the nature of suppression can vary. It is well known that in the case of a wall-normal magnetic field, the field interacts with both the mean and pulsating flow. In the other two cases, such interaction occurs only with the pulsating flow. These variations can be seen in the kinetic energy distribution (Fig. 5.3), which shows turbulence reduction with the magnetic field. In the case of a wall-normal magnetic field such reduction is stronger compared to the other two cases, especially in the bulk region because of flattening of the velocity profile due to the Hartmann effect. To summarize, the wall-normal magnetic field has the strongest effect on the flow laminarization. The spanwise magnetic field has a weaker effect. The weakest effect on the flow laminarization is in the case of

a streamwise magnetic field. These observations agree very well with the major conclusions on the effect of a magnetic field on turbulence in previous numerical [52] and the experimental [70] studies.

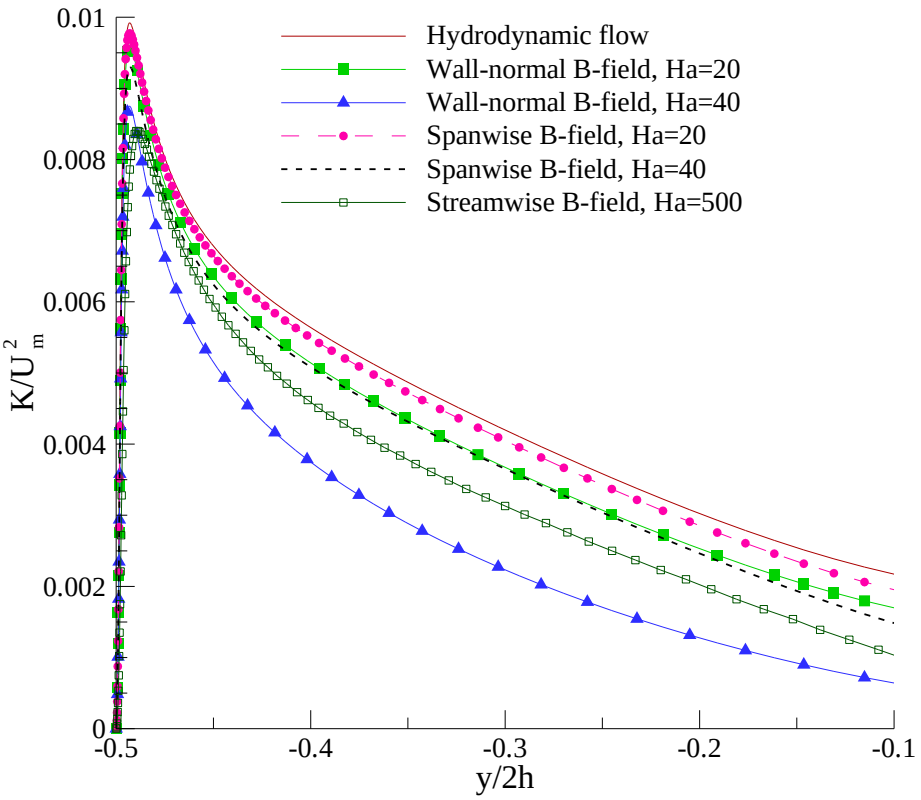

Figure 5.3: Turbulent kinetic energy distribution for three magnetic field orientations at *Re*=75,000.

5.4 Characterization of the Effect of a Magnetic Field on Corrosion

The velocity profiles are computed first as described earlier, and then the velocity data are used as the input for the mass transfer solver. The main goal of this analysis is to address the effect of a magnetic field orientation and its strength on the RAFM wall thinning in a PbLi turbulent flow. To do this, computations are performed for a fully developed flow of PbLi at 500 ^{o}C between two parallel walls of RAFM steel with a channel width of 2 cm and a length of 1 m. These conditions are relevant to many experimental studies, *e.g.* [71]. Three typical magnetic field orientations are considered: a wall-normal magnetic field, a spanwise magnetic field, and a streamwise one. The strength of the applied magnetic field is changed such that the Hartmann number varies from zero to its critical value when turbulence can no longer be sustained.

The relevant dimensionless parameters are the Reynolds number and the Hartmann number as defined above. Another important parameter is the Schmidt number (*Sc*) of the liquid metal. The Schmidt number is defined as the ratio of fluid viscosity (ν) and mass diffusivity (D). Taking the diffusion coefficient of iron in PbLi $D = 6.4\times10^{-9}$ m^2/s and the fluid viscosity $\nu = 1.1\times10^{-7}$ m^2/s (both at 500 ^{o}C), the Schmidt number is *Sc* ~17.

5.4.1 Effect of a magnetic field orientation

Four velocities are considered, 14.6, 29.3, 43.9, and 58.5 cm/s, such that the hydrodynamic Reynolds numbers are: 25,000, 50,000, 75,000 and 100,000. The maximum Hartmann number is: 370 for the case of the wall-normal magnetic field, 280 for the spanwise, and 2350 for the

streamwise magnetic field to capture the most interesting features of the flow when it transitions from full turbulence to a laminar state.

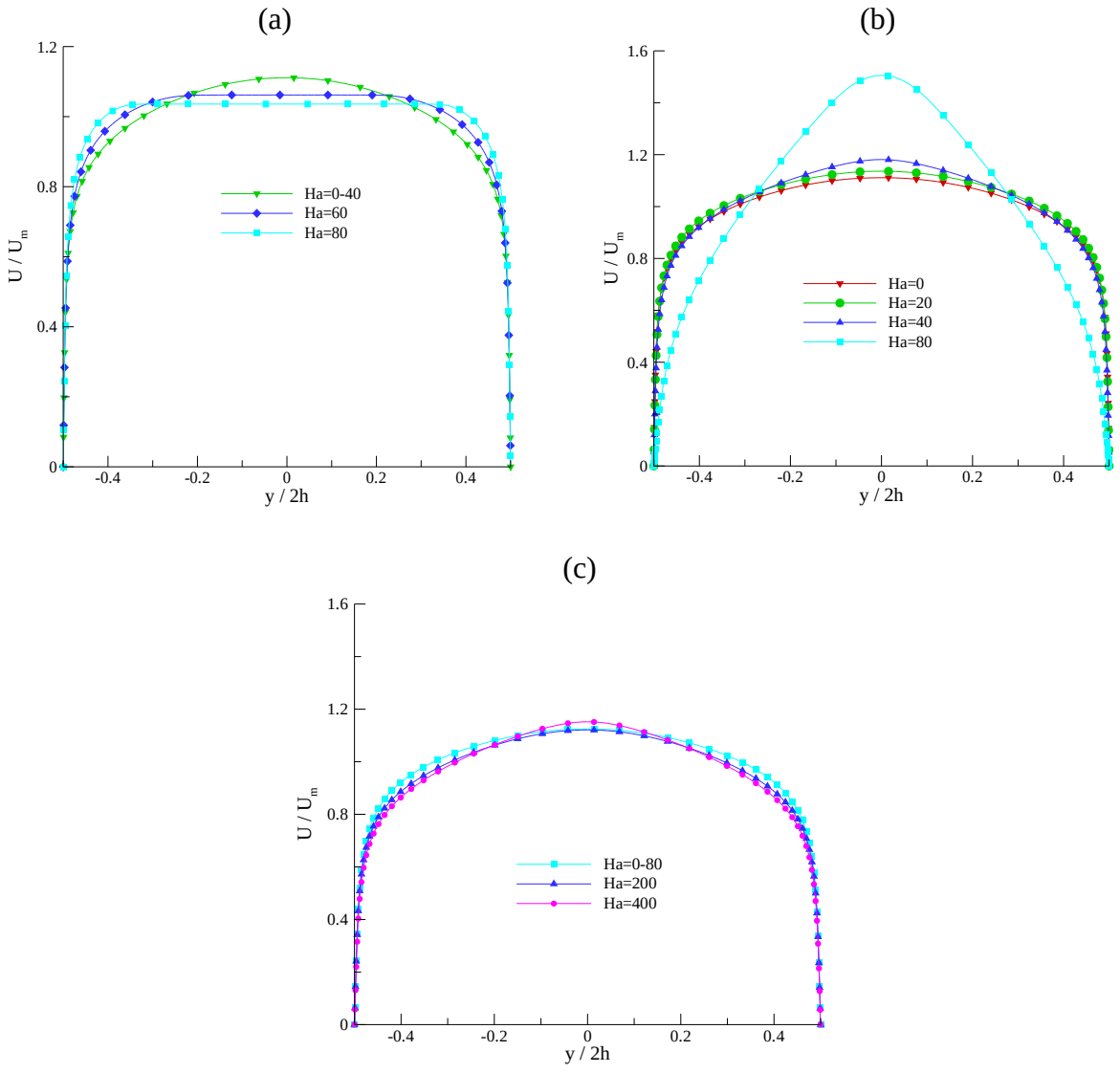

Figure 5.4: Velocity profiles in a turbulent MHD flow in a channel for three magnetic field orientations at *Re*=50,000: (a) wall-normal, (b) spanwise and (c) streamwise magnetic field.

Fig. 5.4 demonstrates velocity profiles in the MHD flows for *Re*=50,000 for all three magnetic field orientations. In the case of a wall-normal magnetic field, the electromagnetic Lorentz force results in the Hartmann effect such that the mean flow near the walls within the Hartmann layers is accelerated, while the flow in the bulk is slowed down resulting in a flattened velocity profile at *Ha* numbers greater than about 50 (Fig. 5.4a). No special MHD boundary layers are formed at the walls in the case of a streamwise or spanwise magnetic field. The streamwise magnetic field has the least effect on the flow of the three field orientations. As shown in Fig. 5.4c, for this magnetic field orientation, a strong magnetic field (*Ha* >200) has to be applied in order to have visible changes in the velocity profile. The observed changes in the mean velocity profile in Fig. 5.4 and also changes in the transport properties, *i.e.*, effective viscosity and diffusivity, with the magnetic field due to reduction of the turbulent kinetic energy (Fig. 5.3) suggest that the magnetic field has a strong effects on corrosion processes. These effects are addressed by computing the concentration field, the mass transfer coefficient k , and the mass transfer rate.

In Fig. 5.5, computed data on the mass transfer rate are plotted as the wall thinning versus the axial distance. In all three cases of the magnetic field orientation, significant changes in the wall thinning occur in the inlet section of the flow and then the wall thinning changes just slightly with the axial distance. The mass transfer rate can also be expressed in a dimensionless form using the Sherwood number (*Sh*) as follows:

$$Sh = kh/D\,. \tag{5.5}$$

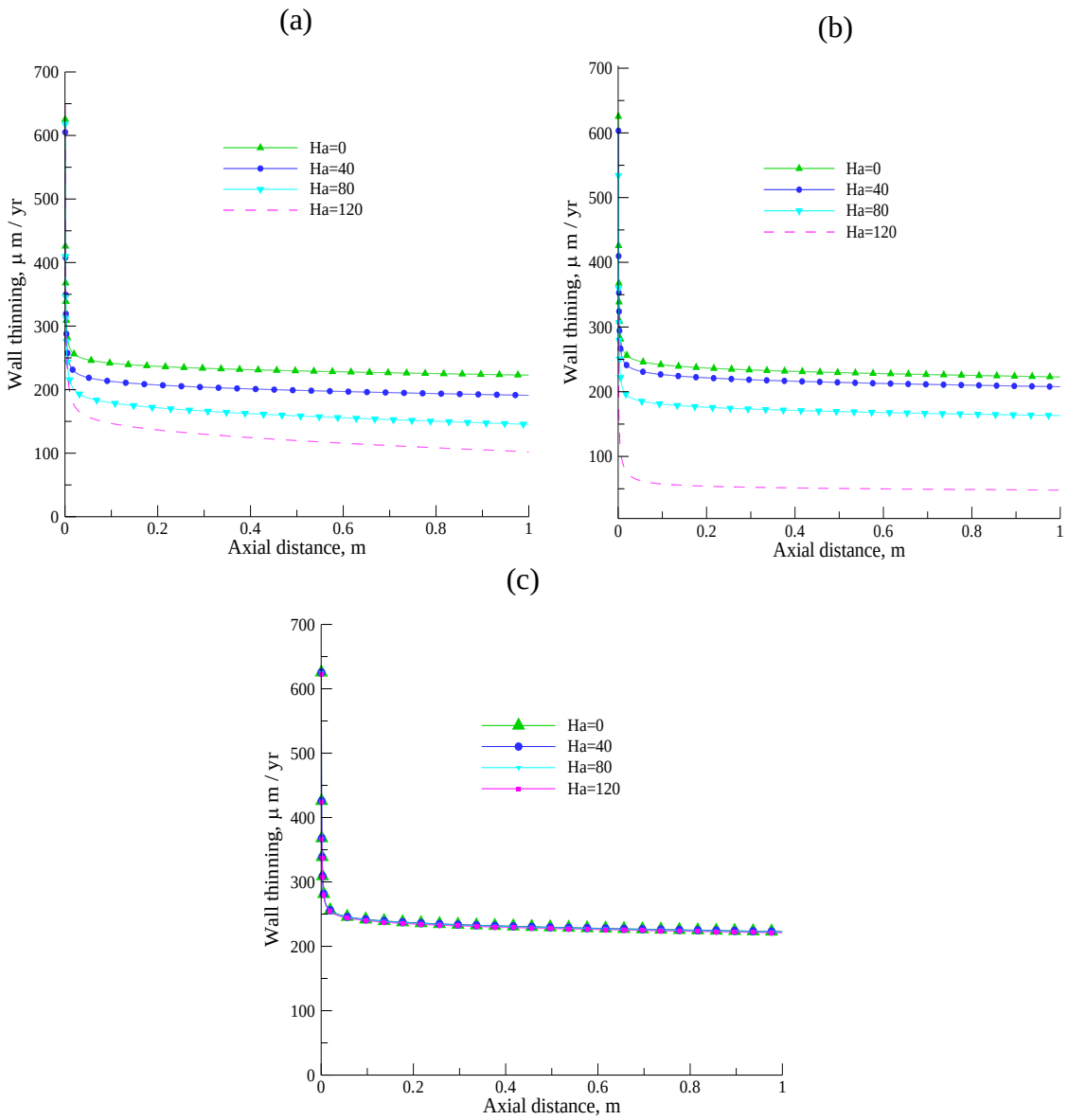

Figure 5.5: Wall thinning with the axial distance *x* in the reference MHD flow at *Re*=50,000: (a) wall-normal, (b) spanwise and (c) streamwise B-field.

Fig. 5.6 illustrates the effect of the parameter *Ha/Re* on the Sherwood number computed at the axial location of 1 m (x/h=100). This parameter plays an important role in the theory of MHD turbulence as its reciprocal can be interpreted as the Reynolds number based on the thickness of the Hartmann layer. When the flow is turbulent, the Sherwood number decreases with the magnetic field due to turbulence suppression and then reaches its laminar value in all three cases of the magnetic field orientation. Similarly to the results presented in the previous section, the strongest effect of the applied magnetic field on corrosion rate in a turbulent flow occurs in the case of a wall-normal magnetic field and the weakest one is in the case of the axial field orientation. In the case of a spanwise magnetic field, lower corrosion rates can be seen at higher *Ha*/*Re* as the flow in a wall-normal magnetic field is already laminar while it is still turbulent in the case of the spanwise magnetic field.

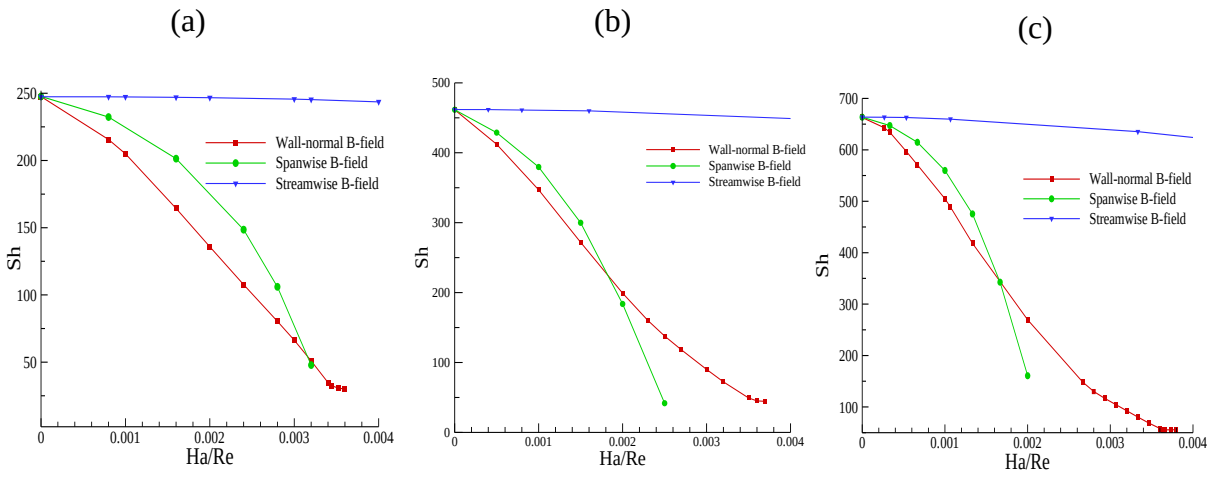

Figure 5.6: Sherwood number as a function of the parameter *Ha/Re*: (a) *Re*=25,000, (b) *Re*=50,000, and (c) *Re*=75,000.

5.4.2 Case of a wall-normal magnetic field

This case is the most interesting of all three cases of the magnetic field orientation as both suppression of turbulence and formation of the Hartmann boundary layer occurs due to the applied magnetic field. Moreover, this particular case is important for applications where there is always a magnetic field component normal to the wall. That is why this case is analyzed in more detail.

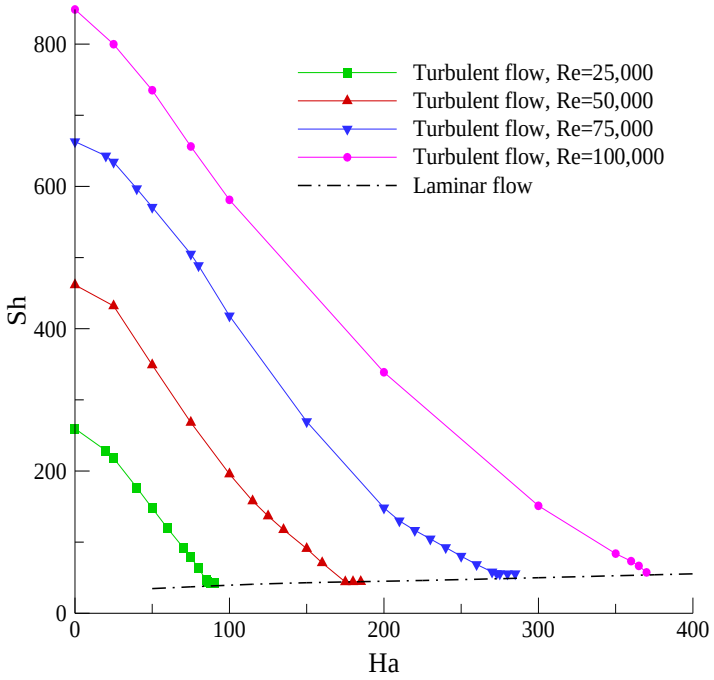

Figure 5.7: Sherwood number as a function of the Hartmann number in the case of a wall-normal magnetic field.

For this magnetic field orientation, Fig. 5.7 shows the Sherwood number versus the Hartmann number for the Reynolds numbers from 25,000 to 100,000. As long as the flow is turbulent, the Sherwood number decreases with the magnetic field. Upon reaching the laminar state, the tendency is changed. Namely, *Sh* starts growing but its increase is less pronounced compared to the fast reduction of the corrosion rate in a turbulent flow. This increase in the corrosion rate in the laminar flow regime is related to steep velocity gradients in the Hartmann layer. The observed

tendencies are similar to the effect of the magnetic field on the friction factor (see Fig. 5.2). However, the friction factor in the laminar MHD flow changes as $2Ha/Re$, while variations of Sh with Ha are obviously different. This confirms that there is no direct analogy between momentum and heat and mass transfer once the magnetic field is applied. The effect of the Hartmann layer on corrosion in laminar MHD flows was studied numerically in [67]. It was shown that the corrosion rate at the Hartmann wall is affected by the magnetic field as long as the concentration boundary layer is thinner than the Hartmann layer. If the Hartmann layer becomes thinner than the concentration boundary layer as the Hartmann number is increased, further increase in the magnetic field does not affect the corrosion rate anymore. Present results are consistent with these earlier observations.

In Fig. 5.8, the computed wall thinning at the end of the section (x=1 m) are compared with the predictions from the so-called Sannier equation [16], which was constructed using experimental data on corrosion of ferritic/martensitic steels in hydrodynamic turbulent PbLi flows. This equation predicts the wall thinning as a function of the velocity, channel dimension and the temperature. Sannier's equation was used in the past to predict corrosion rates in PbLi blankets. From the present comparison, it is obvious that application of this equation to conditions of a fusion blanket or even to experimental conditions (once a magnetic field is present) can result in misleading conclusions since the magnetic field changes the corrosion rates significantly as demonstrated in the figure. On the other hand, present numerical data computed without a magnetic field match very well those from Sannier's equation.

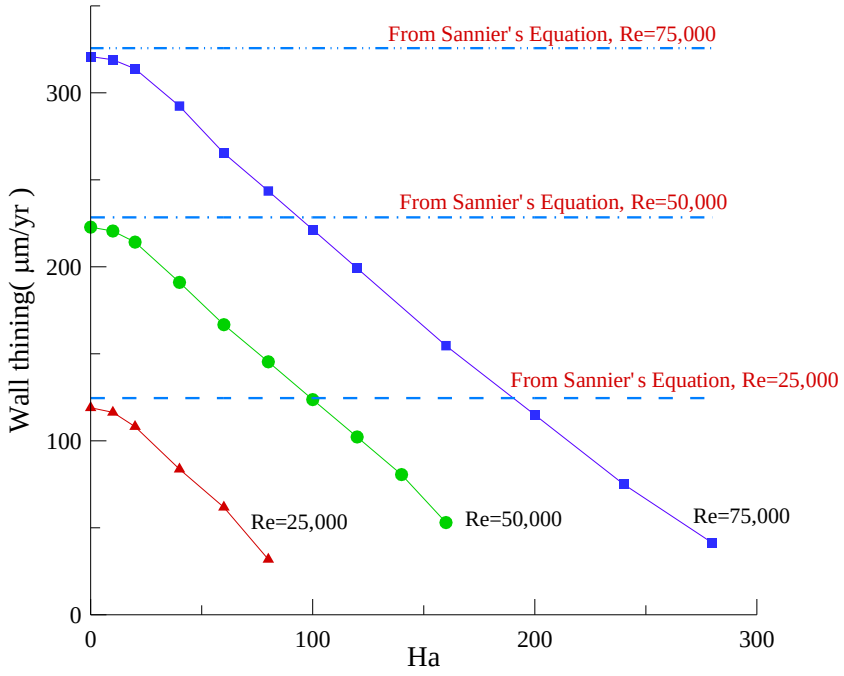

Figure 5.8: Comparison of the computed wall thinning with the predictions from Sannier's equation [16] for the case of a wall-normal magnetic field at 500°C.

The numerical data for the mass loss in the case of a wall-normal magnetic field can be approximated using a specially constructed dimensionless correlation. In this correlation, the Sherwood number is expressed as a function of both Hartmann number and Reynolds number. Such a correlation for the Sherwood number in hydrodynamic flows is usually obtained from experimental or numerical data within certain limits and are typically of the form $Sh = a\ \mathrm{Re}^b\ Sc^c$, where a, b, and c are empirical constants. Taking into account that in the reference MHD flow of PbLi there is an additional dimensionless parameter, the Hartmann number, the correlation can be recommended in the form of

$$Sh = a\ Re^b Sc^c Ha^d . \qquad (5.6)$$

The obtained numerical data for the Sherwood number can be used for evaluation of constants *a*, *b* and *d*. Evaluation of constant *c* in the reference corrosion case is not possible since all

corrosion data are limited to PbLi, meaning that *Sc* number cannot be varied. In fact, for PbLi at temperature 500°C *Sc*~17. Therefore, the desired correlation should be sought in the form of

$$Sh = a\ Re^{b} Ha^{d}\ . \tag{5.7}$$

This correlation should also include the effect of temperature. This can be done by introducing the temperature effect via the parameter *a*: $a = f(T)$. It is obvious that the function *f* should be in the exponential form since the effect of the temperature in the liquid metal corrosion is always of Arrhenius type. For consistency with the way of presenting the data in a dimensionless form, the temperature should also be introduced as a dimensionless parameter, such as $T/[T]$. The temperature scale $[T]$ should be chosen in relation to physics of the corrosion process. However, it is also possible to introduce a reference temperature, for example $[T] = T_0 = 500°\text{C}$ since in PbLi blanket applications temperatures around 500° are very typical.

It should be mentioned that the semi-empirical Sannier's equation (Eq. 5.8) on corrosion of ferritic/martensitic steels in hydrodynamic turbulent PbLi flows, was constructed in terms of dimensional parameters, such as velocity, temperature, and channel dimension. [16]. The use of correlation is limited to PbLi for which $Sc \sim 17$ and $Pr \sim 0.01$:

$$\nu = 8 \times 10^{9} \times Exp\left(\frac{-25690}{1.98T}\right) \times U_m^{0.875} \times D_h^{-0.125}, \mu m / yr\ . \tag{5.8}$$

This correlation can be used, however, to calculate the Sherwood number Sh_0 in a hydrodynamic PbLi flow. Simple analysis shows that for 500°C, $Sh_0 = 0.03704 \times \left(Re^{0.875}\right)$.

Although Eq. 5.6 seems to be a proper basis to construct a correlation for the Sherwood number in the case of MHD PbLi flows, the special shape of curves in Fig. 5.7 suggests slightly different approach. Namely, all curves in this figure are of the same shape, such that the desired correlation can be sought in the form of

$$Sh - Sh_o = c\ Ha^d\ . \tag{5.9}$$

The main advantage of Eq. 5.9 over Eq. 5.7 is that only two parameters, *c* and *d*, need to be evaluated. An additional advantage is that the effect of temperature is already introduced via Sh_0. The coefficients *c* and *d* have been evaluated from the numerical data shown in Fig. 5.7. As a result the correlation for the Sherwood number takes the following form:

$$Sh = Sh_0 - 0.792 \times \left(Ha^{1.289} \right). \tag{5.10}$$

To calculate Sh_0, Sannier's correlation Eq. 5.8 can be used. Eq. 5.10 has the same applicability limits as Sannier's equation itself: velocity 0.01 – 0.3 m/s, temperature 450-550 °C, duct dimension 0.005-0.05 m. Maximum magnetic field can be found from $Ha/Re=(Ha/Re)_{cr}$ to assure that the flow is still turbulent. The critical value of this parameter for the case of a wall-normal magnetic field is about 1/225 [70]. These dimensional limits can also be converted in dimensionless ones: Reynolds number 5,000-100,000, dimensionless temperature 0.81-1.00 (here temperature 500 °C is used as the temperature scale), $Ha<Re/225$. Fig. 5.9 illustrates the obtained Sherwood number as a function of *Ha* number using the derived correlation and that computed with the numerical code.

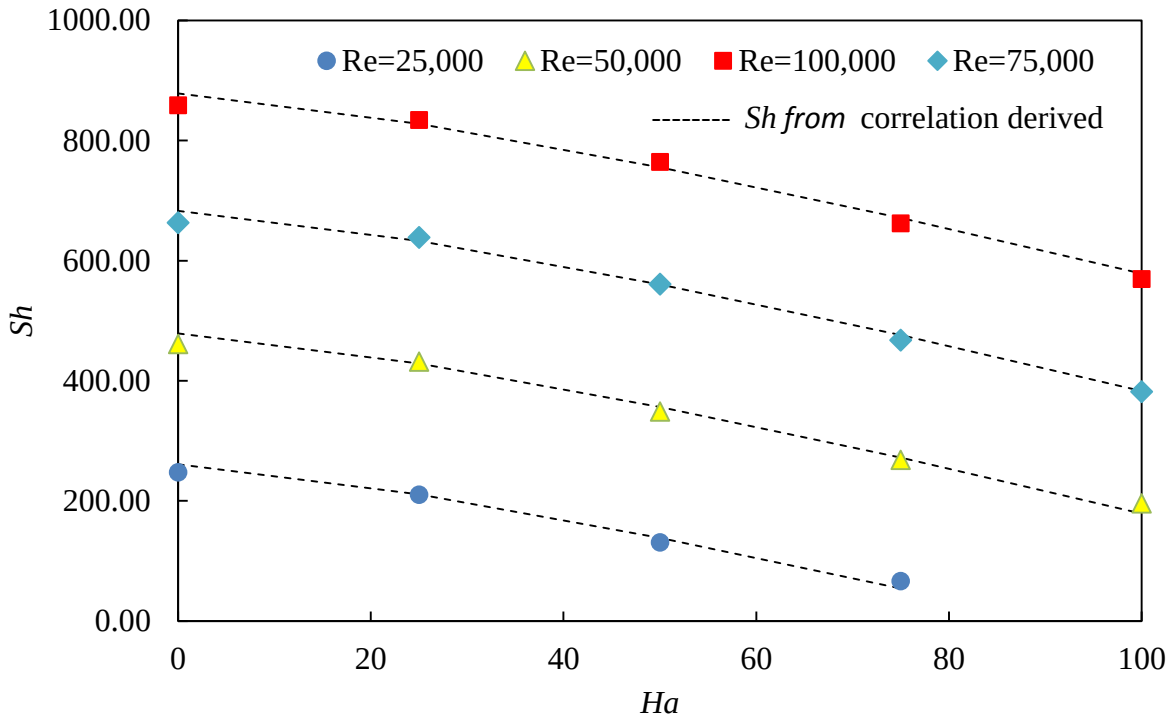

Figure 5.9: Comparison between Sherwood numbers obtained with the correlation (dotted lines) and those computed (symbols).

Senstivity test was conducted for the obtained correlation for *Sh*, using C_s correlation from the Brogstedt correlation from literature. Brogstedt correlation predicts the saturation concentration at 500 ^{o}C to be 5% different from the reconstructed saturation concentration proposed in this study which was used in computation of *Sh* and deriviation of the proposed correlation for *Sh* for turbulent flow including the effect of a magnetic field. The Sh_0 (purely hydrodynamic flow, no MHD effect) computation using Brogstedt differs only by 1% from the Sh_0 obtained using the Sannier's equation or/and the numerical data for the turbulent flow accompanied in this study, however the computed values for *Sh* (using Brogstedt correlation) which included the effect of magnetic field, differ from the result obtained by proposed

correlation up to 15% for some higher values of *Re* and *Ha* (*Re*=100,000 and *Ha*=100). Figure 5.10 shows the effect of *Ha* number on *Sh* for both results obtained from the proposed correlation and the numerical data obtained using the Brogstedt saturation concentration. The data obtained from Brogstedt correlation is fairly within the 10% difference range for the most range of *Ha* and *Re*, however at higher *Ha* values, the deviation exceed the 10% difference. Average deviation was estimated to be less than 7%.

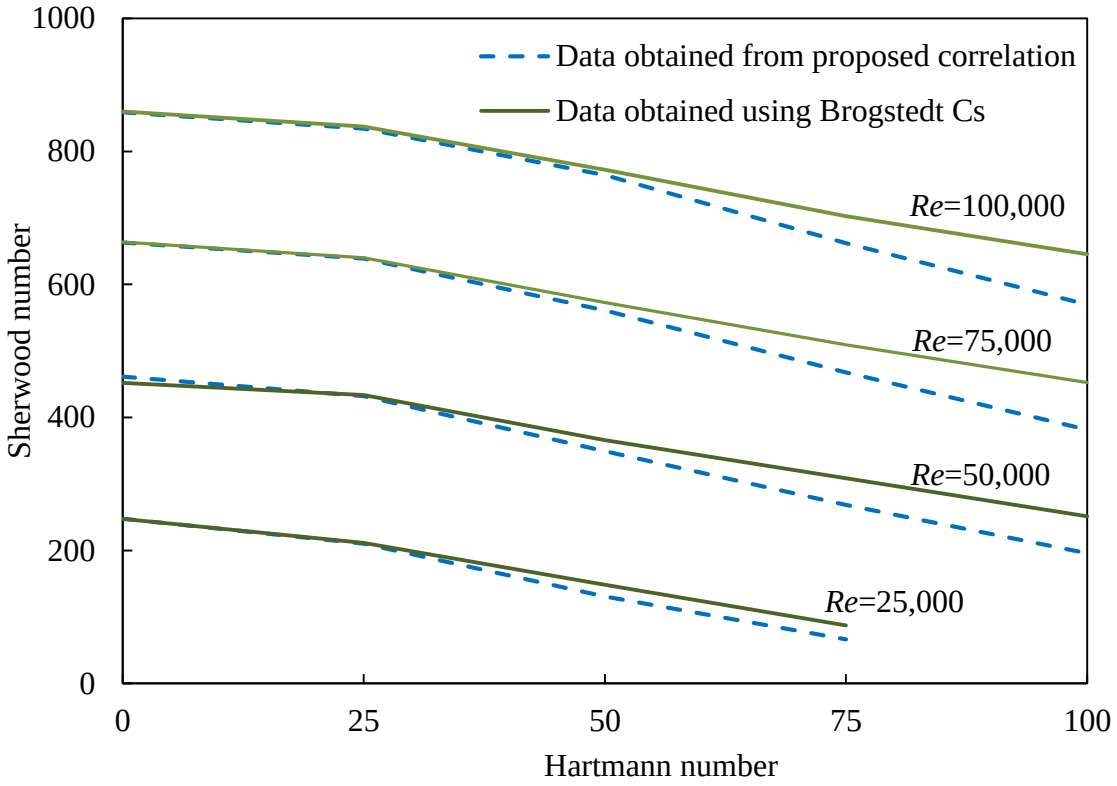

Figure 5.10: Sensitivity test on obtained correlation for Sherwood using C_s obtained from Brogstedt correlation

5.5 Influence of Temperature on Corrosion in the Presence of a Magnetic Field

In addition to the effect of magnetic field on the mass loss, the effect of temperature is considered, providing a magnetic field is applied. For illustration purposes, the Hartmann number and the Reynolds number are set at 40 and 50,000. Three different orientations of the magnetic field are considered. In this analysis, the temperature is varied from 400^{o} C to 550^{o} C.

Fig. 5.11 illustrates the effect of the temperature on the average wall thinning. Averaging was performed over the whole channel length. As expected, the wall thinning varies exponentially as the temperature increases. This exponential increase in the corrosion rate is consistent with previous experimental observations for corrosion of ferritic/martensitic steels in turbulent PbLi flows [5]. Physically, such a strong influence of the temperature on corrosion is explained by its effect on saturation concentration, which conforms to the exponential Arrhenius law. However, in the case of the wall-normal magnetic field, the wall thinning is always smaller compared to other two magnetic field orientations. In fact, the flow in the case of a streamwise magnetic field shown in the figure is almost the same as the purely hydrodynamic flow as the Hartmann number is relatively small. Correspondingly, the wall thinning in the case of the streamwise magnetic field is the highest because of the weakest effect of the magnetic field on turbulence. The observed tendencies are qualitatively the same even at higher Hartmann numbers, providing the flows are still turbulent.

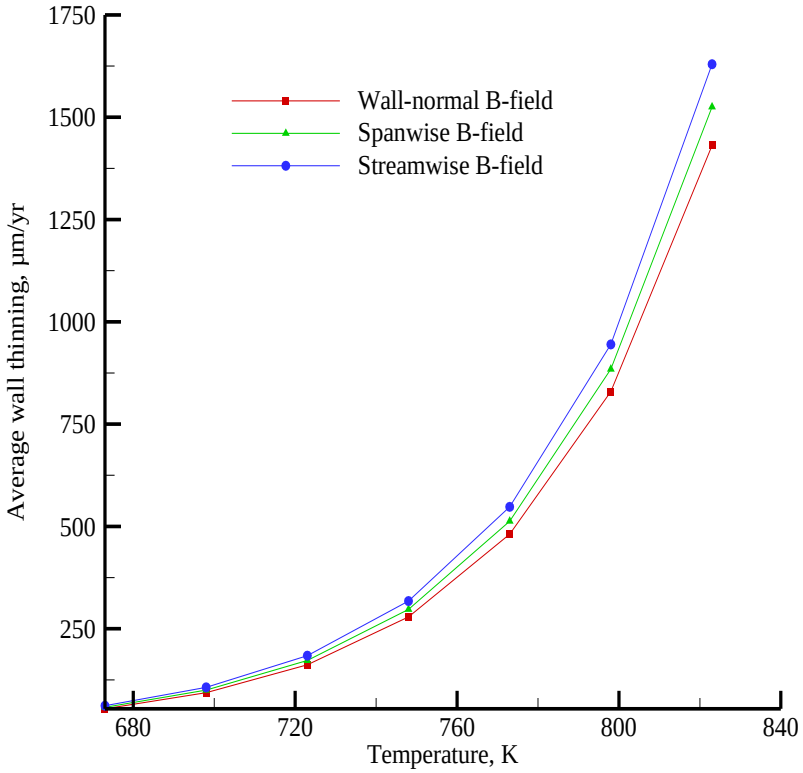

Figure 5.11: Effect of the temperature on the average wall thinning at *Re*=50,000 and *Ha*=40 for three magnetic field orientations.

5.6 Concluding Remarks

The effects of a magnetic field on corrosion of ferritic/martensitic steels in a turbulent PbLi flow in a magnetic field were studied for three magnetic field orientations. For the studied cases, the magnetic field always suppresses turbulence resulting in smaller corrosion rates compared to hydrodynamic flows. However, the wall-normal magnetic field has the strongest effect on reduction of the corrosion rate due to more intensive suppression of turbulence compared to the spanwise and axial field orientation. The weakest effect is observed in the case of the axial magnetic field. Of these three magnetic field orientations, the case of a wall-normal magnetic field is the most interesting as both turbulence suppression and formation of the Hartmann layer occur. Once the flow in a wall-normal magnetic field becomes laminar, the corrosion rate increases slightly due to steeper velocity gradients in the Hartmann layer. This behavior resembles variations of the friction factor in the MHD flow in a wall-normal magnetic field but is quantitatively different. This stresses that there is no direct analogy between momentum and heat and mass transfer once a magnetic field is applied.

Comparisons with predictions from Sannier's equation have demonstrated that this equation cannot be applied to fusion blanket applications to predict the corrosion rates, as MHD effects in the PbLi flows are dominant in a blanket. The results obtained for turbulent flows and also the earlier analysis of corrosion of RAFM steels in laminar PbLi flows [67] explain contradictive observations about the effect of a magnetic field on corrosion rates. In fact, in turbulent flows (the special case of the so-called quasi-two-dimensional turbulence [72] is not considered here), the corrosion rate always drops as a magnetic field is increased. In laminar flows, however, the tendency is opposite. Namely, in rectangular duct MHD flows, much stronger corrosion rates can be observed at the Hartmann walls (doubling the corrosion rates compared to hydrodynamic flows

[5] and at the side walls (2-3 times stronger corrosion rates compared to the Hartmann wall). As applied to experimental studies, this suggests that the corrosion data must always be analyzed, taking effects of the magnetic field on the velocity structure into account. These new results also suggest that the presently accepted corrosion limits (maximum corrosion rate and maximum allowable temperature at the solid-liquid interface) for a PbLi blanket have to be revisited. It should also be mentioned that the present studies of corrosion are limited to thin conducting walls. The limitations come from the fact that the K-ε model used in computations was derived assuming that induced currents are all closing within the liquid metal domain [52].

In the case of a wall-normal magnetic field this assumption is well justified if the wall conductance ratio defined as $c_w = t_w\sigma_w/b\sigma$ (t_w is the wall thickness) is smaller than $1/Ha$. In the other two cases of the magnetic field orientation, the electrically conducting walls may result in further turbulence suppression with the magnetic field as demonstrated in Ref. [73] for a spanwise magnetic field and in Ref [74] for a streamwise magnetic field. However, in these studies the flow-confining walls were treated as perfectly conducting. Therefore, the flow effects associated with the finite-thickness electrically conducting walls and their influence on corrosion processes should be further addressed.

CHAPTER 6

Application to US DCLL Blanket

6.1 Introduction

The Dual-Coolant Lead-Lithium (DCLL) blanket concept, which is at present under development in the US, evolved from the ARIES studies [75]. The DCLL blanket is considered for testing in ITER (International Thermonuclear Experimental Reactor) (Fig. 6.1) and as a primary candidate for a DEMO reactor (Fig. 6.2) [76-77]. Use of eutectic alloy PbLi in DCLL can lead to tritium self-sufficiency without an additional neutron multiplier. The alloy has high resistance to irradiation damages. It has higher thermal conductivity in comparison to ceramic breeders [78]. Besides, PbLi has demonstrated lower chemical reactivity with water, air and concrete compared to pure lithium. These all make PbLi to be a very attractive candidate for blanket applications as breeder/coolant.

The corrosion of structural blanket materials in the flowing PbLi, transport of activated corrosion products and their deposition in the cold section of the liquid-metal loop are, however, important technical and safety issues, which need to be carefully addressed when developing a PbLi blanket concept [79]. At present, the deposition processes in the cooler parts of a loop are believed to be more critical to the safe blanket operation than reduction of strength by wall thinning in the hotter parts. However, the corrosion data are required to address transport of corrosion products throughout the liquid metal loop, and to address their deposition in the cold section.

The main goal of this analysis is to perform analysis of corrosion losses in poloidal flows (about 90% of the entire blanket volume) of a DCLL blanket using an integrated mathematical model that incorporates all key phenomena, such as MHD, heat and mass transfer. The analysis is done for a multi-material domain that includes the bulk and gap flow regions filled with PbLi, the flow channel insert (FCI) made of silicon carbide composite (SiC), and the RAFM wall. The analysis presented below is a parametric study, where corrosion losses are evaluated for several electrical conductivities of the FCI and several liquid metal temperatures. The computational procedure involves three steps. First, the velocity distribution is calculated using an MHD code. Second, the computed velocity field is used as an input data in the calculations of the temperature field using a heat transfer code. Finally, the velocity and temperature data are used in the computations of the concentration field and the mass loss using the TRANSMAG code.

6.2 US DCLL Blanket

The DCLL blanket concept, which is used here as a reference blanket to calculate corrosion losses, is the US DCLL DEMO blanket (Fig. 6.2) proposed in [77]. In this blanket, eutectic alloy PbLi circulates slowly in poloidal ducts (~ 10 cm/s) for power conversion and tritium breeding. Reduced activation ferritic steel (RAFM) is used as the structural material and helium (He) is used to cool the first wall and blanket structure. The poloidal length of each module is ~2 m, while the radial depth is ~ 40 cm. The poloidal ducts in the row next to the first wall are referred to as "front" ducts, while the ducts in the second or third rows are referred to as "return" ducts. The blanket module is located in the outboard (OB) region, where the magnetic field is about 4 T. The liquid metal enters the inlet manifold at the bottom of the blanket module from the annulus of the concentric pipe and then it is distributed into three front poloidal ducts where it flows upwards.

At the top of the module, the PbLi makes a 180^{o} turn and then flows downwards through the return ducts. At the bottom of the module, the liquid is collected and leaves the module from the outlet manifold through the internal tube of the concentric pipe.

A key element of the DCLL concept is the FCI made of SiC, either as a composite or as foam, which serves as an electrical insulator to reduce the impact from the MHD pressure drop of the circulating liquid metal, and as thermal insulator to separate the high temperature PbLi from the ferritic structure. Using FCIs allow for high exit temperature (700 ^{o}C or even higher) and may lead to high blanket efficiency [80]. The FCI is separated from the ferritic wall by a thin (~ 2 mm) gap also filled with PbLi. The flow inside the FCI is referred to as "bulk flow", and that in the gap as "gap flow". The gaps oriented perpendicular to the applied magnetic field are referred to as Hartmann gaps, and the other two gaps, parallel to the magnetic field are called side gaps. Both the gap flow and that bulk flow are driven by the same pressure head. The gap and the bulk flows can be connected through small openings in one of the FCI walls (either holes or a slot). The opening may be needed for equalizing the pressure on both sides of the FCI. The parameters related to the reference DCLL DEMO blanket are summarized in [79] and shown here in Table 6.1. Each particular duct (front or return) is characterized by own set of parameters. Table 6.1 also shows the main dimensions for the front poloidal duct of the reference blanket, which are used here in the computations.

TABLE 6.1

Operation Parameters for the Reference DCLL DEMO Blanket and Basic Dimentions for the Front Poloidal Duct [79]

Operation Parameters

Toroidal magnetic field (outboard)	4 T
PbLi mean flow velocity	0.064 m/ s
Inlet/Outlet He temperature	400/600^{o} C
Inlet/Outlet PbLi temperature	500/700^{o} C
Average Neutron wall loading	2.13 MW/m^2
Peak outboard neutron wall loading	3.72 MW/m^2
Average first wall heat flux	0.8 MW/m^2

Basic Dimentions for the Front Poloidal Duct

Channel sizes	2b=0.211 m (toroidal), 2a=0.207 m (radial)
Poloidal length	2 m
FCI thickness	0.005 m
Gap width	0.002 m
Ferritic wall thickness	0.005 m

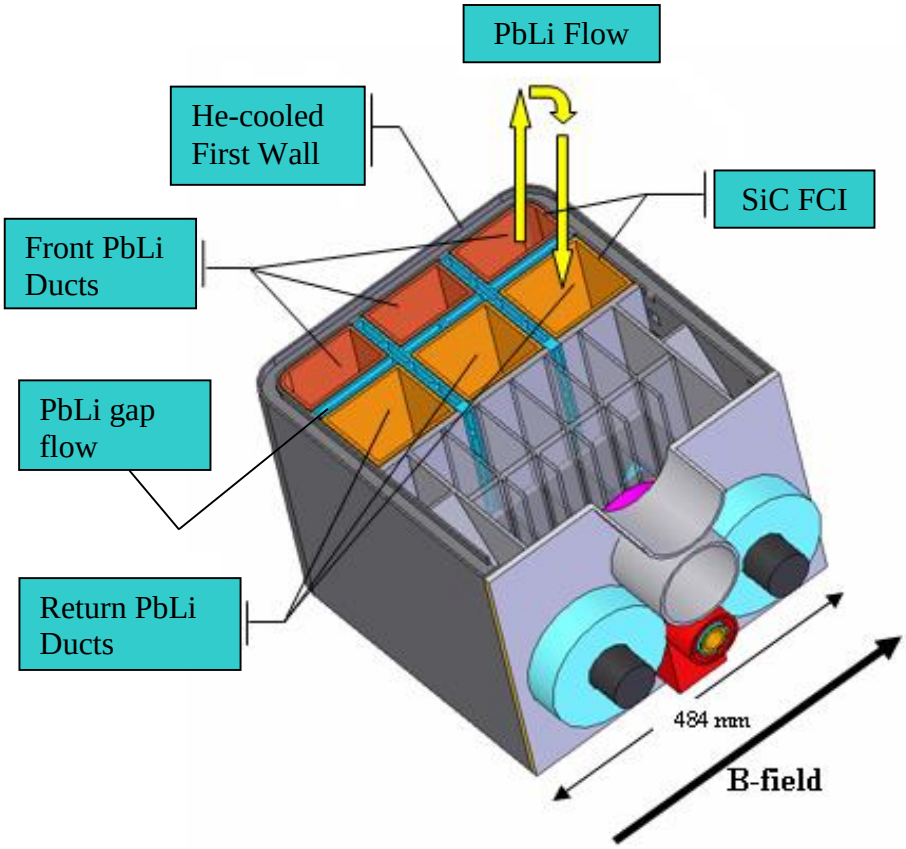

Figure 6.1: Sketch of the US ITER DCLL Test Blanket Module [76].

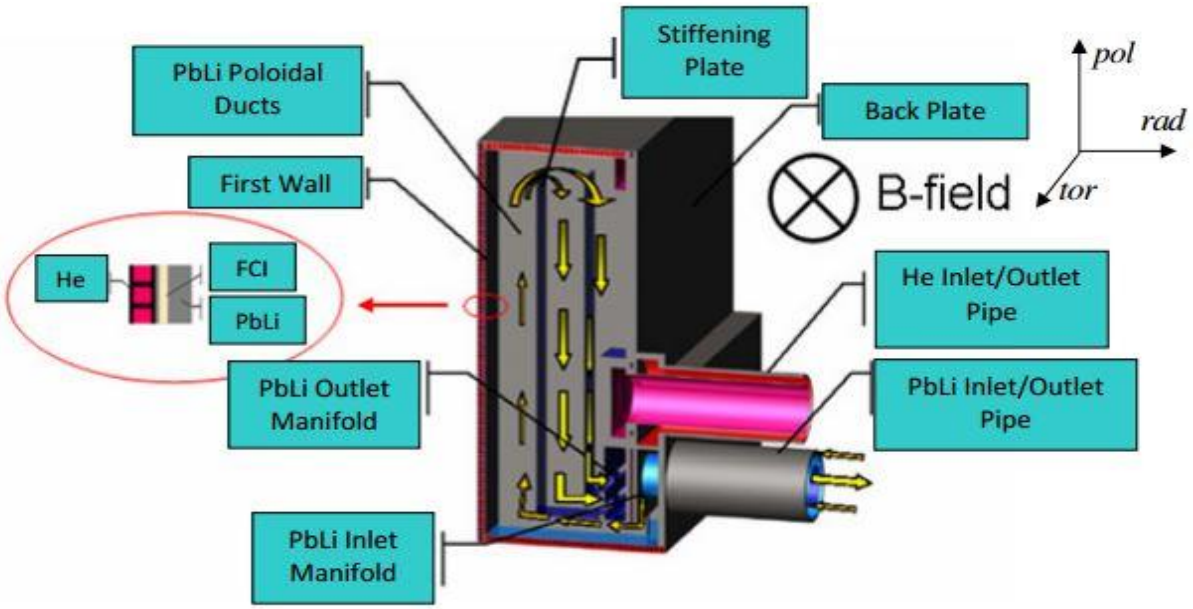

Figure 6.2: Sketch of the US DCLL DEMO blanket module [77].

6.3 Mathematical Model and Computer Code

In a strong reactor magnetic field, the hydrodynamic entry length is strongly reduced in comparison with non-MHD flows [81]. This provides grounds for the exception that at a distance of a few characteristic channel dimensions from the inlet, the flow becomes fully developed or at least close enough to a fully developed state, so that the fully developed flow model seems to be applicable. Three different codes are used in this study. First, the momentum (Eq. 6.1) and induction equation (Eq. 6.2) are solved. Details of the mathematical model and computer code are explained in [82]. After completing the MHD calculation, the velocity distribution is used as input data for solving the energy equation (Eq. 6.3). The temperature distribution at the RAFM walls was used to specify the saturation concentration that is later used in the mass transfer code. The velocity and temperature data are used in order to solve the mass transfer problem using the TRANSMAG code which was described in chapter 3.

The mathematical model assumes laminar 2D fully developed flow and 3D heat transfer. The problem is formulated in terms of the flow velocity (U), induced magnetic field (B_x), temperature (T) and mass concentration(C). The governing equations that describe the problem are:

$$\nu\left(\frac{\partial^2 U}{\partial z^2}+\frac{\partial^2 U}{\partial y^2}\right)-\frac{1}{\rho}\frac{dp}{dx}+\frac{B_z^o}{\rho\mu_o}\frac{\partial B_x}{\partial z}=0 \quad , \tag{6.1}$$

$$\frac{1}{\mu_o}\frac{\partial}{\partial z}\left(\frac{1}{\sigma_y}\frac{\partial B_x}{\partial z}\right)+\frac{1}{\mu_o}\frac{\partial}{\partial y}\left(\frac{1}{\sigma_z}\frac{\partial B_x}{\partial y}\right)+B_z^o\frac{\partial U}{\partial z}=0 \quad , \tag{6.2}$$

and

$$\rho\, C_P U\frac{\partial T}{\partial x}=\frac{\partial}{\partial x}\left(k_x\frac{\partial T}{\partial x}\right)+\frac{\partial}{\partial y}\left(k_y\frac{\partial T}{\partial y}\right)+\frac{\partial}{\partial z}\left(k_z\frac{\partial T}{\partial z}\right)+q_T''' \quad . \tag{6.3}$$

Here μ_o is the magnetic permeability of vacuum, ν the kinematic viscosity, ρ the density, k the thermal conductivity, and σ the electrical conductivity. The notation σ_y and σ_z are introduced to represent possible anisotropy in σ. The mass transfer equation for concentration C of iron in PbLi has already been introduced in Chapter 3 and thus is not repeated here. The coordinates x, y, and z in denote the poloidal, radial and toroidal distance (Fig. 6.2). The x-axis coincides with the channel axis. The coordinate origin is located in the bottom plane, at the flow inlet. In Eq. 6.3, the source term q_T''' stands for volumetric heating, and it is determined independently from neutronics calculation using the code DANTSYS [83]. The results for the volumetric heating are then approximated as a function of radial depth as proposed in [84].

The distinctive feature of the DCLL blanket compared to other PbLi blankets (*e.g.* to self-cooled PbLi blanket) is that corrosion of RAFM in the flowing PbLi occurs in a thin gap between the RAFM wall and the FCI structure. This implies special boundary condition on the concentration. These boundary conditions are illustrated in Fig 6.3 for a front duct. At the inlet of the front duct (point C in Fig. 6.3), the concentration has been set to zero, and for the two return ducts it has been set to the outlet concentration of the front duct. At the interface between the RAFM wall and the liquid metal flowing in the gap (point A in Fig. 6.3), the wall temperature distribution is obtained from the heat transfer computations and then the saturation concentration is evaluated as a function of temperature using the correlation for saturation concentration obtained in Chapter 3. The boundary condition at the interface between the SiC FCI and PbLi (point B in Fig. 6.3) assumes that there is no corrosion and also no diffusion of iron from the PbLi flow into the SiC material, such that $\partial C / \partial y = 0$ here. This zero mass flux boundary condition has been justified in experimental studies in [85-86]. It was observed that there was no chemical or physical interaction between PbLi and silicon carbide at high temperatures up to 900^o C. Thus, it was

concluded that SiC does not corrode in PbLi, and neither PbLi nor corrosion products does not permeate into SiC. The boundary condition on the velocity is a no-slip condition at the interface between the liquid and solid. The external boundary condition on B_x requires no induced magnetic field at the outer boundary of the integration domain.

The electrical conductivity of SiC, which is an important parameter in the proposed corrosion model, depends on SiC structure (composite or foam) and fabrication technique. It can vary in a wide range. The values used in this study were 0.01 and 10 S/m. The lower value represents a particular case when the FCI acts as an ideal electrical insulator. The higher value is more realistic and typical to SiC composites. Results of calculations for MHD flow using the flow channel insert are computed at $\sigma_z = \sigma_y = \sigma_{SiC}$ since the effect of anisotropy was found to be small [84]. No anisotropy in k was also assumed such that $k_x = k_y = k_z = k_{SiC}$. The electrical conductivities of the RAFM wall and that of PbLi are 1.4×10^6 and 0.7×10^6 S/m, respectively. The dynamic viscosity of PbLi is 0.001 Pa s. The applied magnetic field is 4 T.

To solve Eqs. 6.1 and 6.2., a numerical code [82] was used. The code has been specially designed for channels with a "sandwich" structure of several materials with different material properties. The code includes a finite volume formulation, automatically generated Hartmann number sensitive meshes, and an effective convergence acceleration technique [84]. In the computations, the momentum equation (Eq. 6.1) is solved in the liquid only, while the induction equation (Eq. 6.2) and energy equation (Eq. 6.3) are solved over the whole domain, including all liquid and solid sub-domains. The computational mesh includes 215×215 points (101×101 points in the bulk flow, 27 across the gap, 15 across the wall, and 15 mesh points across the FCI). The mesh generation procedure used in the code places from about one-fourth to one-third of all

grid points across the Hartmann layer, so that each Hartmann layer is resolved with about 15 points [82].

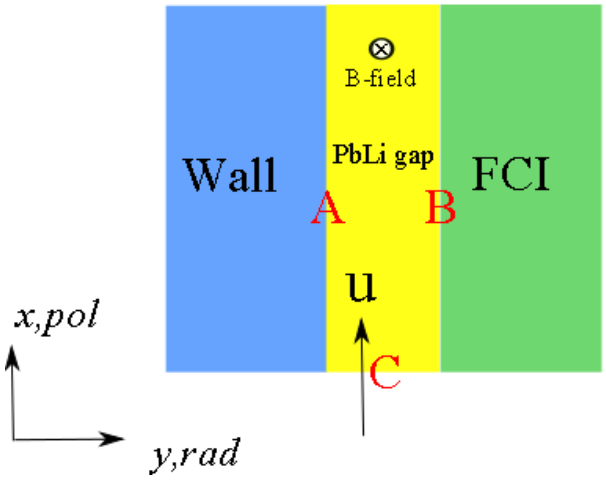

	BOUNDARY CONDITIONS
	c_{Fe}
C	$C_0 = 0$ (front duct), $C_0 = C(out_{frontduct})$ (both return ducts)
A	$C_{sat}(t_w)$ Saturation values
B	$\partial C/\partial \eta = 0$ No flux

Figure 6.3: Sketch showing 2D gap geometry and boundary conditions used for iron concentration applied in the calculation.

6.4 Characterization of MHD Flow and Heat Transfer in the DCLL Blanket

Two parameters that might have the strongest effect on the corrosion as demonstrated in the previous studies and also in Chapter 3 of this dissertation are: velocity distribution and temperature distribution. Thus, it is necessary to consider the velocity and the temperature field in the poloidal flows of the DCLL blanket first. In this section the results of the MHD and heat transfer computations are presented, and the most important features of the velocity and temperature field from the perspective of their effect on corrosion processes are summarized.

The present MHD analysis is applied to the entire cross-sectional area of the blanket duct, which includes not only the bulk flow but also the FCI, the ferritic wall, and the gap. A typical velocity profile is shown in Fig. 6.4. A characteristic feature of the flow in the bulk (major part of the flow bounded by the FCI structure) is two high-velocity jets near the side walls, which carry most of the volumetric flow rate. This flow in the bulk region induces electrical currents, which cross the FCI and then close their circuit through the gap and the RAFM wall. The current distribution in the gap affects significantly the flow distribution here and thus has a strong impact on corrosion processes. In the analysis, it is important to distinguish between the Hartmann gap (at the wall perpendicular to the magnetic field) and the side gap (at the wall parallel to the magnetic field) because velocity, temperature and the corrosion rate are very different between these two gap sections.

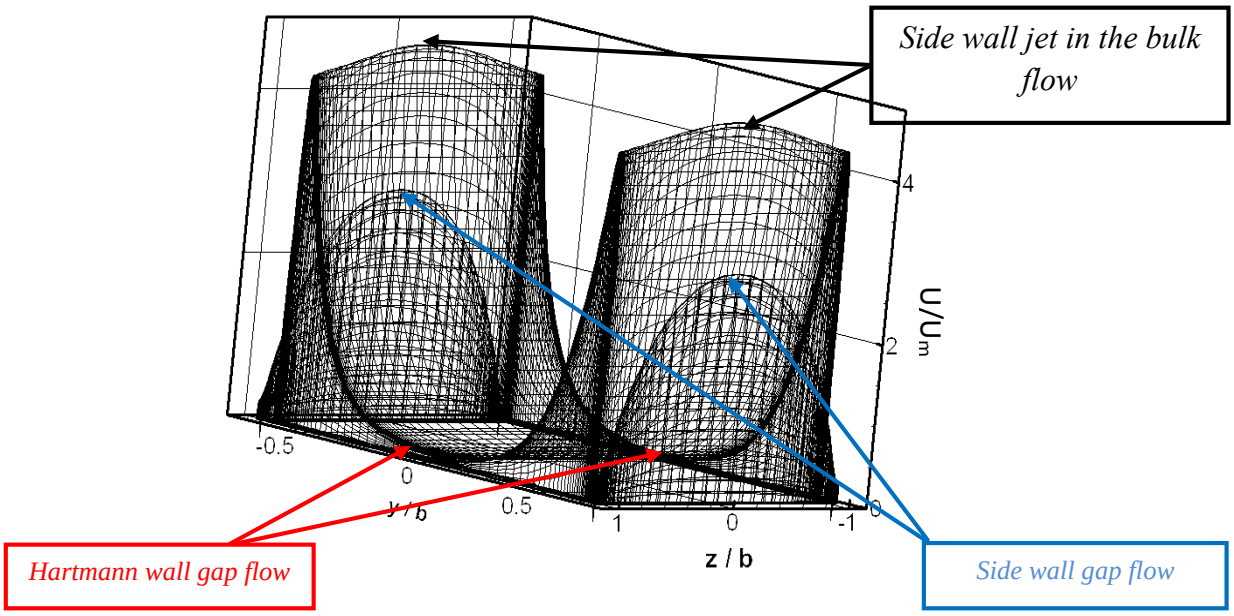

Figure 6.4: Velocity distribution in the front poloidal duct of the DCLL blanket. Geometrical and flow parameters are shown in Table 6.1. The FCI electrical conductivity in the computation is 100 S/m.

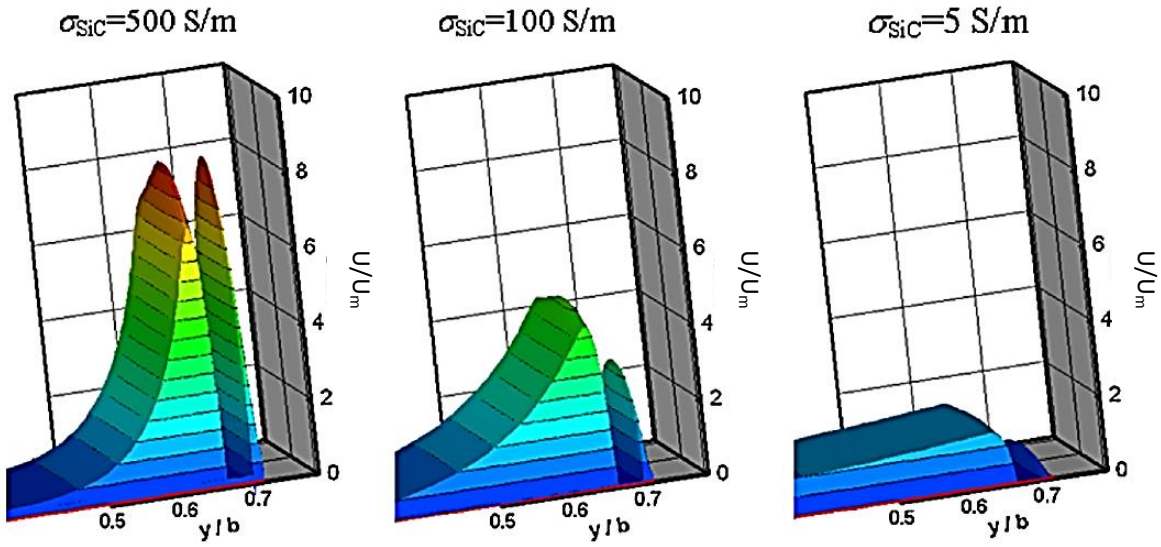

Figure 6.5: Effect of the SiC electrical conductivity on the jet flow [87].

In the side gap, where the electric current is mostly parallel to the magnetic field, the velocity is comparable (0.18 m/s) with the near-wall jets (0.21 m/s), and the velocity profile is close to parabolic. As shown in Fig. 6.4 in the Hartmann gap, the velocity is of a Hartmann type, and the flow is almost stagnant (0.0025 m/s). The velocities in both gap and bulk flow depend on the electrical conductivity of silicon carbide. The effect of the SiC electrical conductivity on the jets is analyzed in Ref. [87] and illustrated here in Fig. 6.5. As the electrical conductivity decreases, the induced electric current decreases, resulting in more uniform velocity distribution and lower jet velocity. Also the decrease in electrical conductivity of the silicon carbide reduces the electromagnetic coupling between the flow in the gap and the bulk flow. The velocity in the gap drops relative to the mean velocity in bulk region. Concurrently, the electrical conductivity of the FCI will have a strong effect on the mass transport via changes in the velocity, especially in the 2-mm gap.

The other parameter that affects corrosion strongly is the temperature distribution. Three-dimensional heat transfer simulations were performed in Ref. [84] to analyze the effect of σ_{SiC} and k_{SiC} on heat transfer in a domain that includes the bulk and gap flow, FCI, and the ferritic wall. The main goal of the study in Ref. [84] was to optimize heat transfer in the blanket flows. The key considerations in these heat transfer optimizations are: (a) minimization of heat losses from the liquid metal into helium flows, (b) reduction of thermal stresses associated with the temperature gradient across the FCI, and (c) control of the temperature at the interface between the RAFM wall and the flowing PbLi in the gap below its corrosion limit of ~470^{o} C. As seen from Fig. 6.6 the characteristic feature of the temperature distribution in the duct is the intense temperature variations in the radial directions. Changes in the temperature field in the toroidal direction are small in the central region but very large at the edge of the domain, where the ferritic structure is

cooled by the helium flows. The temperature also changes in the poloidal direction due to the transport of heat by the liquid metal flow. Maximum temperatures are achieved at the flow exit. Temperatures at the edges of the domain are mostly controlled by the helium flows, while in the central part of the domain by the liquid metal flow.

Both thermal conductivity and electric conductivity of silicon carbide have a strong effect on the temperature field. Fig. 6.6 shows the effect of k_{SiC} and σ_{SiC} on the radial temperature distribution at the channel top in a narrow region facing the first wall. The effect of thermal conductivity is thermal insulation of the bulk flow region, *i.e.* the reduction of heat exchange between the bulk and gap flows. The influence of electrical conductivity on heat transfer is not so obvious, since its variations result in significant changes in heat transfer through modification of the liquid metal flow. Reduction in σ_{SiC} causes a larger temperature difference across the FCI, and hence may lead to higher thermal stresses. It also leads to higher interface temperatures between the ferritic wall and liquid metal. At the same time, reduction of σ_{SiC} is desirable because of smaller pressure losses.

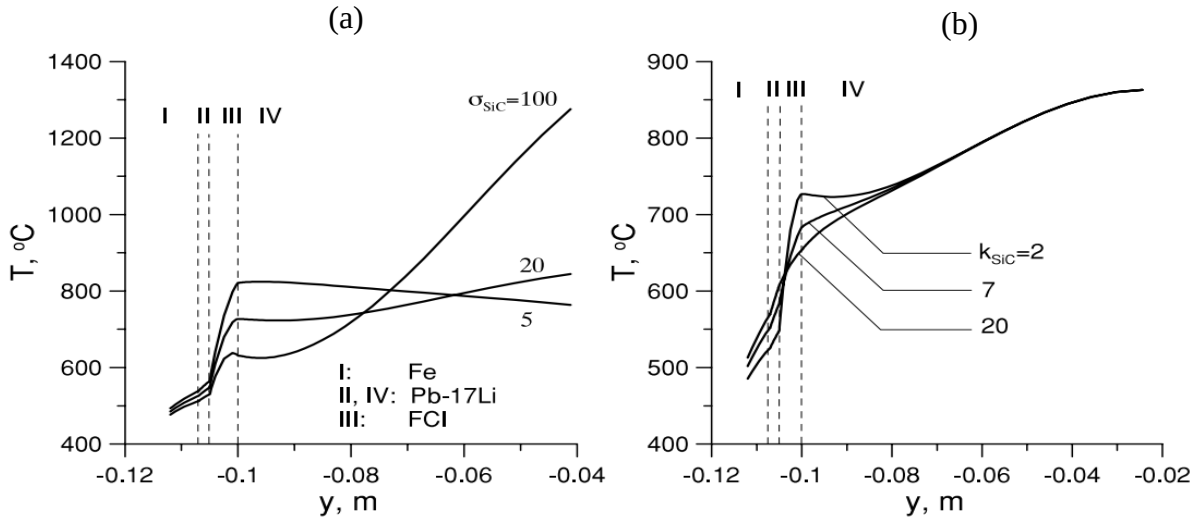

Figure 6.6: Radial temperature distribution in the vicinity of the front wall at the flow exit at (a) $k_{SiC} = 2$ W/m.K and (b) $\sigma_{SiC} = 20$ S/m [87].

6.5 Studies of Corrosion and Transport of Corrosion Products in the DCLL blanket

The study of corrosion of RAFM walls in the PbLi flowing in the thin 2-mm gap includes two parts. In the first part, a parametric analysis was carried out for the front duct whose dimensions and flow parameters are specified in Table. 6.1. In these computations the liquid metal temperature and the electrical conductivity of the FCI are used as parameters. Three temperatures (450, 500 and 550 °C) and three electrical conductivities (0.01, 10 and 100 S/m) are considered. In the second part, numerical computations of corrosion are performed for the entire blanket, including the front poloidal duct and the two return ducts for two FCI electrical conductivities 0.01 and 10

S/m. In these computations, the full temperature distribution computed with the 3D heat transfer code is used to calculate the saturation concentration at the liquid-RAFM interface .

6.5.1 Analysis using temperature and electrical conductivity as parameters

The first computation was performed for a constant PbLi temperature of 500 ^{o}C and the electrical conductivity of the SiC FCI of 10 S/m. The computed velocity field (Fig. 6.7a) demonstrates that in the side gap the velocity is comparable with that in the bulk flow, but in the Hartmann gap, the velocity is two orders of magnitude smaller. In the figure, the velocity is scaled with the mean bulk velocity U_m. Due to very low velocities in the Hartmann gap (smaller than 1 mm/s) the corrosion rate in the Hartmann gap is significantly lower compared to the side gap as demonstrated in Fig. 6.7b. For example, in the Hartmann gap, the wall thinning is 6 μm/yr at the axial location of 1 m from the flow inlet, and for the side gap at the same location, it is 38 μm/yr.

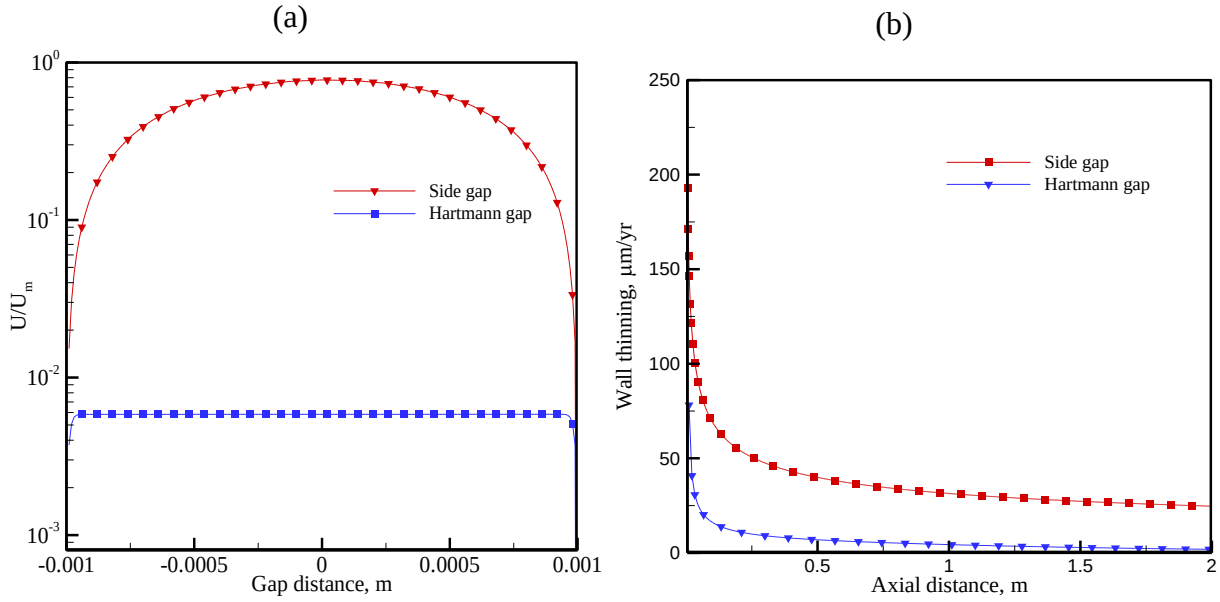

Figure 6.7: (a) velocity distribution in the gap (b) wall thinning with the axial distance in the reference MHD poloidal flow for both side gap and Hartmann gap with T_{PbLi}= 500 ^{o}C and σ_{FCI}=10.0 S·m^{-1} .

TABLE 6.2

The Results of a Parametric Study of the Effect of Electrical Conductivity of SiC and Temperature on Mass Loss

For the Side Gap

Temp (°C)	σ_{SiC} (S/m)	ν_{avg} (μm/yr)	ν_{max} (μm/yr)	ν_{min} (μm/yr)
450	0.01	10.0	54.0	6.0
	10	13.0	70.0	8.0
	100	21.0	120	14.0
500	0.01	29.0	161	19.0
	10	38.0	349	25.0
	100	62.0	357	41.0
550	0.01	86.0	477	56.0
	10	111	622	73.0
	100	185	1060	123

For the Hartmann Gap

Temp (°C)	σ_{SiC} (S/m)	ν_{avg} (μm/yr)	ν_{max} (μm/yr)	ν_{min} (μm/yr)
450	0.01	0.10	1.60	0.00
	10	2.00	26.2	0.60
	100	7.33	77.3	3.75
500	0.01	0.30	2.15	0.00
	10	6.24	78.1	1.86
	100	19.7	220	10.0
550	0.01	0.549	4.43	0.00
	10	17.9	121	5.53
	100	63.1	377	33.1

More computations were then performed for additional temperatures 450 ^{o}C and 550 ^{o}C. Also, the electrical conductivity of SiC was varied from a small value of 0.01 S/m to a large value of 100 S/m. Table 6.2 summarizes the corrosion results obtained in these parametric studies for the tested temperatures and electrical conductivities for the side gap and the Hartmann gap in the form of wall thinning. The table shows average (ν_{avg}), minimum (ν_{min}), and maximum (ν_{max}) wall thinning. The average ν_{avg} is the result of averaging over the duct length as $L^{-1}\int_0^L v(x)dx$. The maximum and minimum wall thinning ν_{max} and ν_{min} occur at the flow inlet and outlet respectively. As expected, the wall thinning increases as the temperature increases. The increase in the SiC electrical conductivity results in higher corrosion losses in both Hartmann and side gap due to higher velocities as seen from Fig. 6.8.

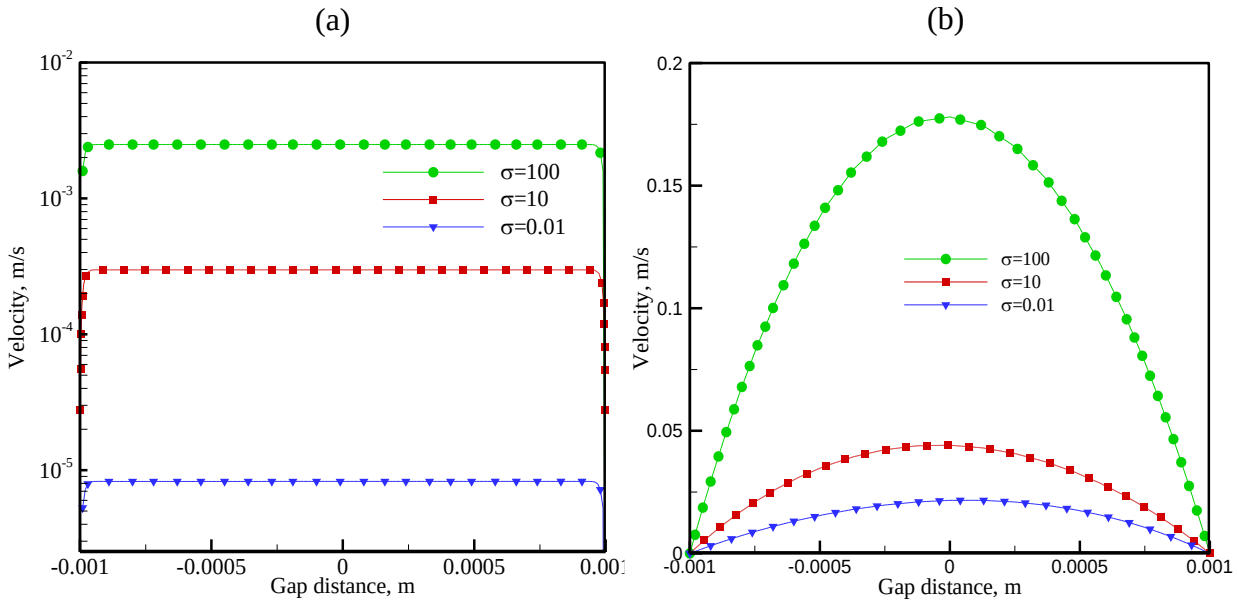

Figure 6.8: Effect of σ_{SiC} (S/m) on the velocity profile at the duct centerline for a) Hartmann gap, b) Side gap for U_m=0.064 m/s.

6.5.2. Analysis using full temperature distribution

The analysis performed in this section is similar to that in Section 6.5.1 but the liquid metal temperature is not taken to be constant. Instead, full temperature distribution based on 3D heat transfer computations is used to specify the temperature-dependent saturation concentration of iron in PbLi at all RAFM-PbLi interfaces. Fig. 6.9 illustrates the temperature distribution in PbLi as the liquid metal flows first through the front duct and then through the return ducts. The temperature field in the flowing PbLi is affected by two opposite processes: neutron volumetric heating and heat losses from the PbLi into cooling helium streams. The most temperature increase occurs in the front duct, where most of the volumetric heat is deposited. The first return duct demonstrates a smaller temperature increase than the front duct. The second return duct demonstrates some decrease in the bulk temperature since the heat losses exceed the heat generation.

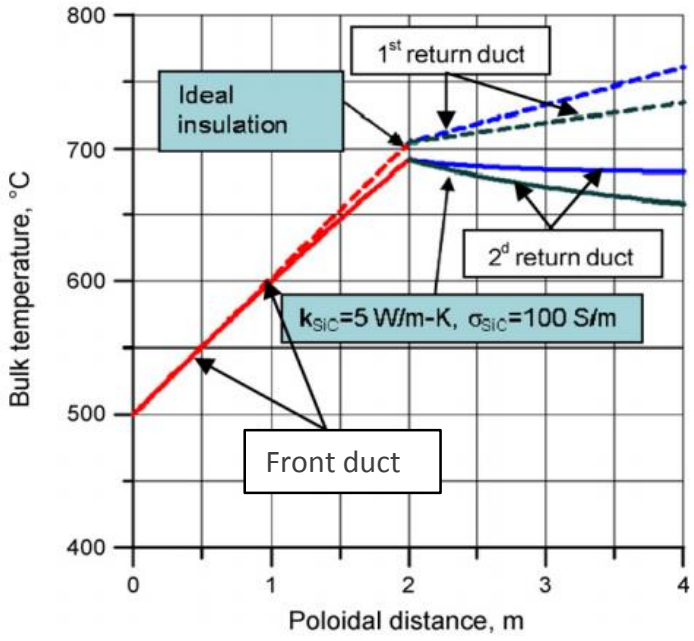

Figure 6.9: Bulk temperature variations in the PbLi for the DEMO scenario [89]

The corrosion analysis is performed for all three poloidal flows (front and two return ducts) at four particular locations in the flow as shown in Fig. 6.10a. Locations 1 and 2 correspond to two Hartmann gaps. In fact, there is no difference between the results for these two locations due to symmetry, so that only one of these two locations is considered. Locations 3 and 4 correspond to the side gap. For all three ducts, corrosion rates are always different between these two locations because of the temperature differences. Figure 6.10b shows the interfacial temperatures for these four locations for all poloidal flows.

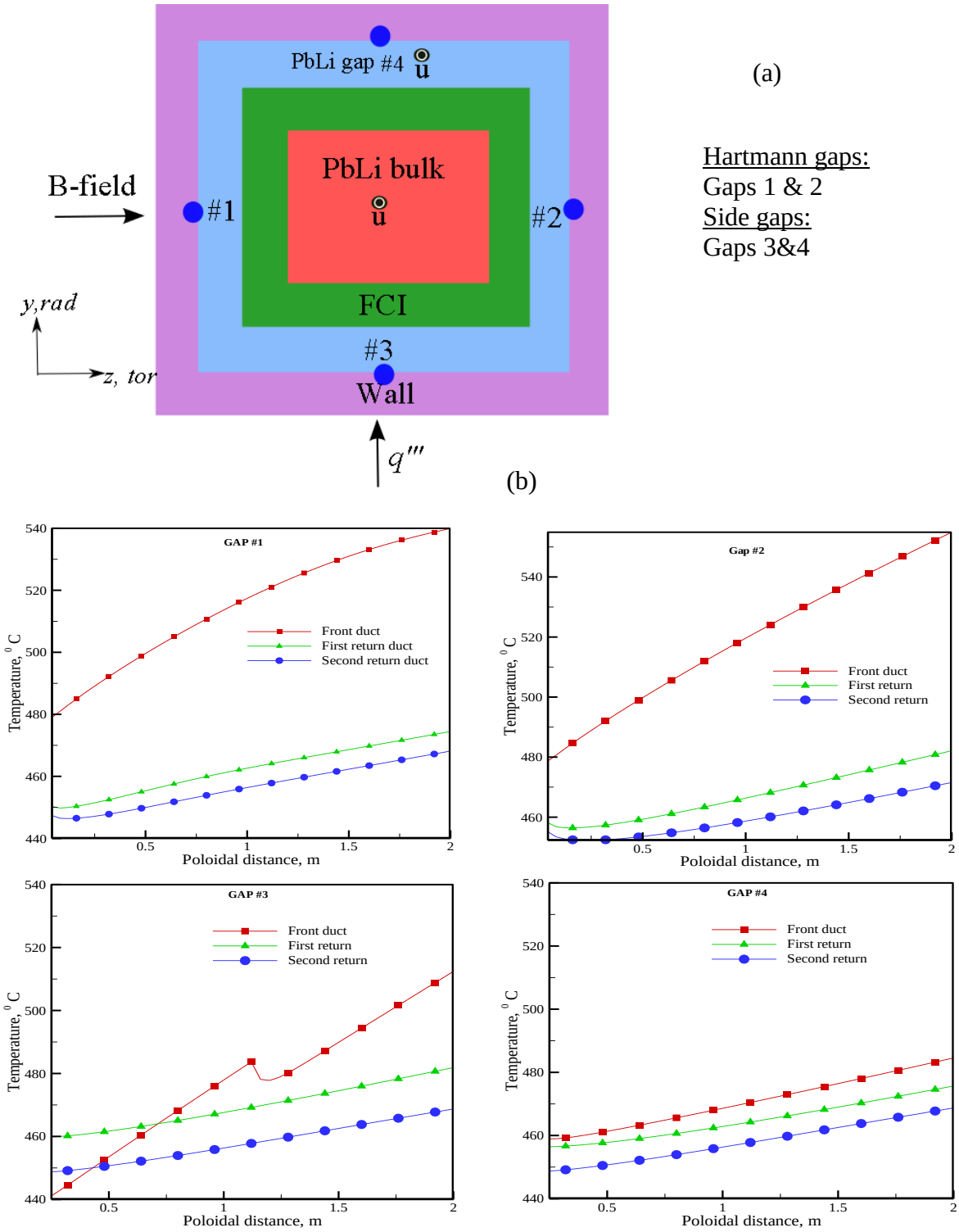

Figure 6.10: (a) four locations are shown where corrosion calculations are performed, (b) temperature distribution at the interface between RAFM and PbLi for all poloidal ducts at the specified locations for $\sigma_{FCI}=100$ S/m.

Mass transfer results have been obtained for the Hartmann and side gaps in the front and return ducts using two values of the FCI electrical conductivity, $\sigma_{FCI} = 0.01$ S/m and $\sigma_{FCI} = 10.0$ S/m. Fig. 6.11 shows the effect of σ_{SiC} on the poloidal temperature distribution at the RAFM wall for all four gaps. It is seen that the temperature at the RAFM wall in the case of $\sigma_{FCI} = 0.01$ S/m is higher compared to the case of $\sigma_{FCI} = 10.0$ S/m. Details of the concentration field are further illustrated in Figs. 6.12 and 6.13 and are summarized in Tab. 6.3.

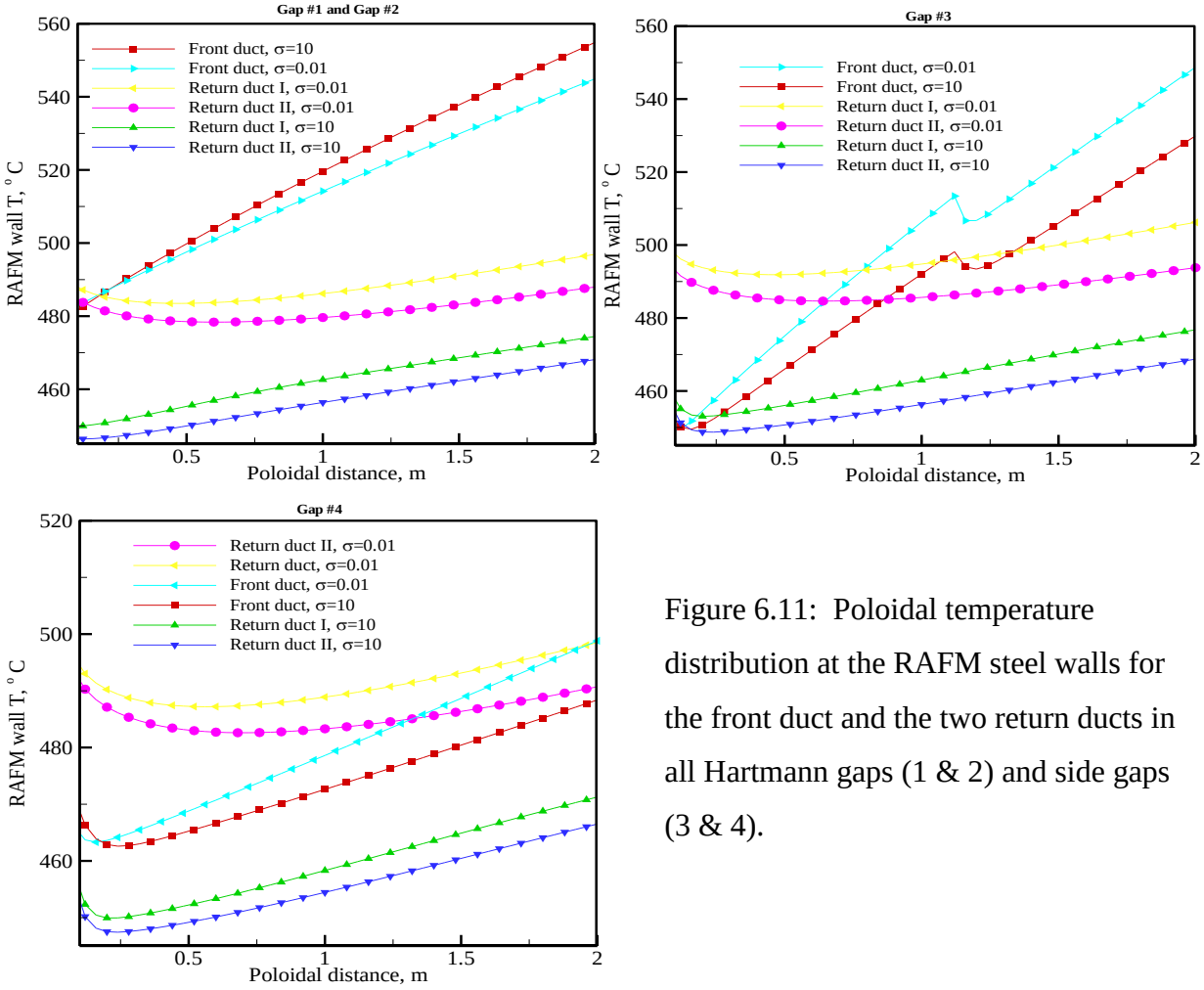

Figure 6.11: Poloidal temperature distribution at the RAFM steel walls for the front duct and the two return ducts in all Hartmann gaps (1 & 2) and side gaps (3 & 4).

TABLE 6.3

Summary of DCLL Mass Transfer Computation Including Front duct and Two Return ducts

Duct	σ_{SiC} (S/m)	Gap #	v_{avg} (μm/yr)	v_{max} (μm/yr)	v_{min} (μm/yr)	Sum of mass loss (kg/yr)
Front duct	0.01	1 or 2	0.027	0.389	0.015	0.000
		3	15.7595	35.856	6.726	0.051
		4	7.02	21.513	6.095	0.023
	10	1 or 2	1.341	11.135	0.050	0.004
		3	15.394	32.892	7.654	0.050
		4	8.995	34.855	9.131	0.029
First return duct	0.01	1 or 2	0.006	0.265	0.003	0.000
		3	7.5735	33.952	6.347	0.025
		4	5.8435	26.878	4.678	0.019
	10	1 or 2	0.1635	6.658	0.022	0.001
		3	5.5415	24.518	6.668	0.018
		4	4.985	34.301	6.588	0.016
Second return duct	0.01	1 or 2	0.005	0.249	0.002	0.000
		3	5.429	26.263	4.098	0.018
		4	5.185	25.774	3.779	0.017
	10	1 or 2	0.142	6.577	0.022	0.000
		3	4.757	24.014	6.560	0.016
		4	4.561	24.021	6.528	0.015
Total mass loss for all gaps	0.01					0.153
	10					0.155

Fig. 6.12 shows the concentration profiles of corrosion products in the side gap (gap #4) as a function of the radial distance for several axial locations.

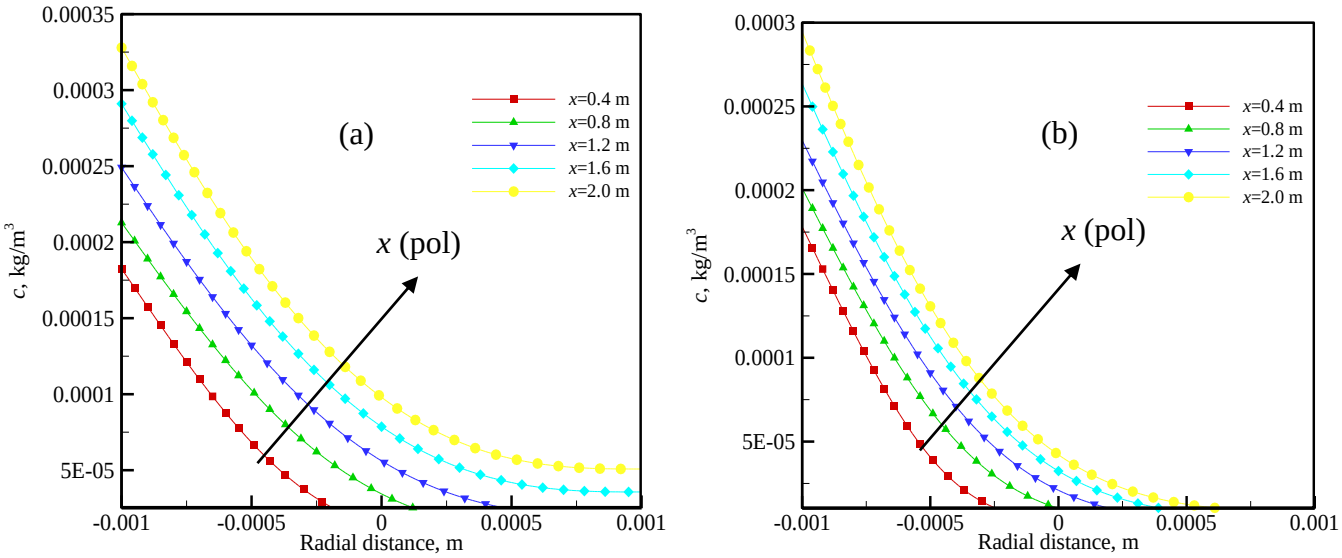

Figure 6.12: Concentration distribution in the front duct calculated for the side gap (gap #4) for (a) $\sigma_{SiC} = 0.01$ S/m and (b) $\sigma_{SiC} = 10.0$ S/m.

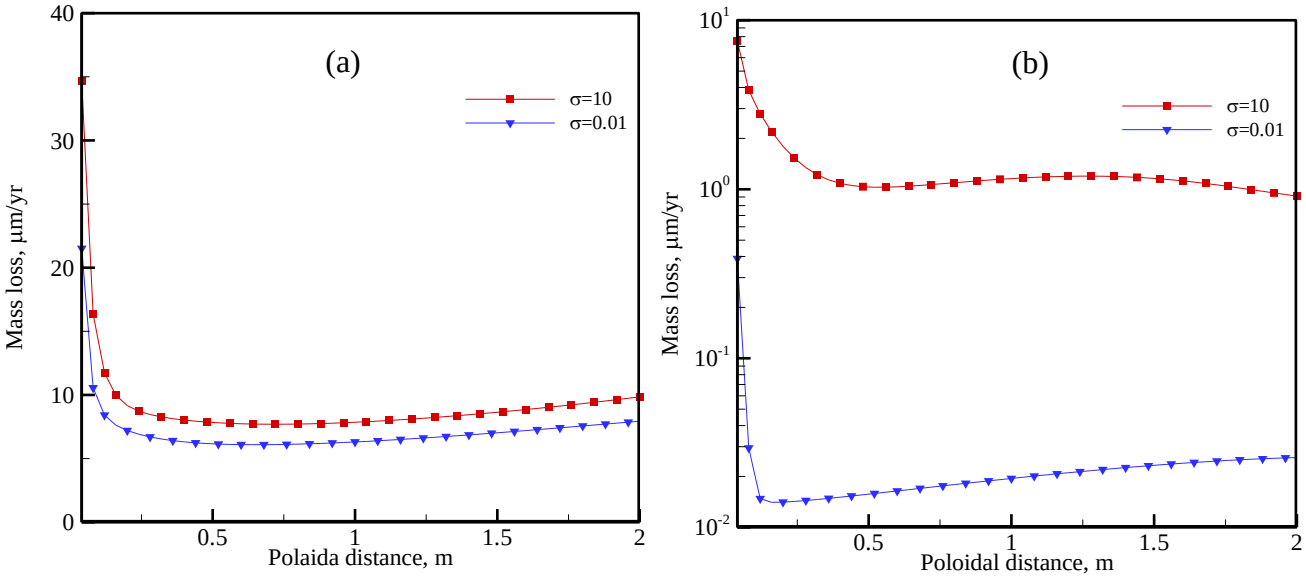

Figure 6.13: Mass transfer comparison for the front duct given in (μm/yr) between two electrical conductivities used in the computation, $\sigma_{FCI} = 0.01$ S/m and $\sigma_{FCI} = 10.0$ S/m (a) Side gap (gap #4), (b) Hartmann gap (gap #1).

Fig. 6.13 shows the mass loss comparison for front duct between the Hartmann gap (# 1) and the side gap (# 4) for both values of electrical conductivity. It is clear that the corrosion rate is much higher in the side gap compared to the Hartmann gap. In the Hartmann gap, the velocity is very slow and the concentration next to the wall rapidly reaches a value close to the saturation concentration. Consequently, there is almost no corrosion occurring in the Hartmann gap.

6.6 Conclusions

Basic characteristics of MHD flow and heat transfer in the front duct and the two return ducts of the DCLL blanket with a SiC_f/SiC FCI were revisited in this this study with numerical simulations using the U.S. DEMO blanket as a prototypical design. After completing the MHD calculations, the velocity distribution is used as an input data for solving the energy equation. The temperature distribution at the RAFM walls was used to specify the saturation concentration at the RAFM wall which is later used in order to solve the mass transfer problem using the TRANSMAG code.

Mass transfer computations have been performed to analyze the mass transfer and transport of corrosion products in flowing PbLi in the gaps formed between the flow channel inserts and the RAFM steel walls in the poloidal ducts (front duct and two return ducts) that transport the liquid metal in a DCLL blanket module. The purpose of this study is to give an initial assessment of the importance of corrosion of the steel wall in a DCLL blanket duct. In the past the DCLL corrosion analysis was conducted only for the Hartmann gaps [88]. However, in this study corrosion analysis for both Hartman and side gaps were done for all poloidal ducts. However it is clear from these computations that the corrosion rate in the side gaps is much higher than in the Hartmann gaps since the velocity in the side gaps is two orders of magnitude higher. Almost 98% of all corrosion occurs in the side gap. Two values of FCI electrical conductivities ($\sigma_{FCI} = 0.01\ \Omega^{-1}\text{m}^{-1}$ and $\sigma_{FCI} = 10.0$) were chosen to study the effect of electrical conductivity on mass transfer. By comparing the results, it is observed that when conductivity decreases, the velocity is reduced in the gaps, which results in less mass transfer in both side and Hartmann gaps. Temperature is the other parameter that affects corrosion rate. As temperature increases, the saturation concentration increases, which results in higher mass loss.

As it was mentioned earlier, most of corrosion occurs in the side-wall section of the gaps. The overall RAFM mass loss per blanket module is ~ 160 g/yr . The average wall thinning is less than 15 μm/yr. The estimated overall mass loss per area based on the corrosion data obtained is ~ 63 g/yr m^2. The total surface area of the wall in the reactor is ~ 662 m^2, which gives an estimate of overall mass loss rate for the whole reactor to be about ~ 44 kg/yr.

The results obtained in this study were compared with the maximum wall temperature of about 470 ºC and maximum wall thinning of 20 μm/yr which ware derived in the past in the Blanket Comparison and Selection Study (BCSS). It is concluded that based on the new results obtained for the corrosion rate under the DCLL conditions, these limiting values can be revisited.

CHAPTER 7

CONCLUSIONS AND FUTURE STUDIES

7.1 Conclusions

Development of a new computational tool for analysis of corrosion. A computational suite called TRANSMAG (TRANSport phenomena in MAGnetohydrodynamic flows) has been developed to address mass transfer processes associated with corrosion of ferritic/martensitic, in particular RAFM steels in the flowing eutectic alloy PbLi with and without a magnetic field. The new tool combines two numerical codes: (i) turbulent hydrodynamic flows in a pipe or a plane channel, and (ii) laminar MHD flows in an electrically conducting rectangular duct.

Construction of a new correlation for saturation concentration of iron in PbLi. The developed computational tool was used to solve a one-parameter inverse mass transfer problem to reconstruct saturation concentration data from the experimental results on corrosion rates in turbulent flows without a magnetic field. These data are then approximated with a new correlation, Eq. (3.21), which gives the saturation concentration of iron in PbLi as a function of the temperature of the liquid in the form of the Arrhenius-like equation. Using this correlation in computations of corrosion processes has resulted in fair prediction of the wall mass loss for a wide range of flow parameters. The applicability of this correlation has been demonstrated in the temperature range

from 450 °C to 550 °C. A good match with the experimental data also suggests the adequacy of the proposed model assumptions, including: mass transfer controlled regime, dilution approximation, one-phase flow and eventually the first type boundary condition in the form of Eq. (3.5).

Numerical analysis of corrosion processes in laminar MHD flows in a rectangular duct. The new correlation for saturation concentration was used in numerical computations using the TRTANSMAG code to analyze mass losses in laminar fully developed rectangular duct flows in the presence of a transverse magnetic field. It was found that the corrosion rate under the effect of a strong magnetic field can be a few times higher compared to pure hydrodynamic flows. However, the computations have revealed significant differences in the corrosion behavior between the Hartmann and the side walls. Namely, the side walls are more affected by the corrosion attack due to formation of high-velocity jets in the flow. The observed differences in the mass loss between these two walls are up to 2-3 times.

The observed differences in the corrosion behavior between the Hartmann and side walls suggest that in MHD rectangular duct flows, most of the mass loss occurs from the side walls, whereas all experimental studies have focused on the Hartmann walls. In both cases, the mass loss in the presence of a magnetic field is always higher compared to the purely hydrodynamic flows. However, the mass loss from the Hartmann wall first increases and then saturates, while the mass loss from the side wall is always increasing. This behavior has been explained by the difference in the thickness of the concentration boundary layer at the Hartmann and side walls. In the case of the Hartmann walls, the thickness of the Hartmann boundary layer is smaller than that of the concentration boundary layer, while in the case of the side walls both boundary layers are

comparable in thickness. The analysis for a case of a strong magnetic field suggests scaling laws for the mass loss *ML* in rectangular ducts, which include the effects of the temperature *T*, mean bulk velocity U_{m} and the applying magnetic field B_0: $ML \sim e^{pT} U_m^q B_0^s$ for the side wall, and $ML \sim e^{pT} U_m^q$ for the Hartmann wall, where $q, s \sim 0.5$. As seen from these laws, the mass loss at the Hartmann wall is not affected by a magnetic field providing the magnetic field is high.

Self-similar analytical solution and analysis of corrosion in the Hartmann flow. A self-similar analytical solution for the corrosion mass transfer problem in the case of the Hartmann flow was obtained for two particular cases. The first particular case corresponds to the initial section of the boundary layer where the Hartmann layer is thicker (or much thicker) than the concentration boundary layer (Zone I). The second particular case corresponds to the section of the boundary layer where the concentration boundary layer is thicker than the Hartmann layer (Zone III). For both solutions for the zones I and III, there was a very good agreement between the analytical solution and the numerical computations.

The obtained solutions were applied to two PbLi blankets: Self-Cooled PbLi (SCLL) and Dual-Coolant PbLi (DCLL) blankets. Two blanket scenarios are considered for an inboard (IB) blanket at magnetic field of 10 T and outboard (OB) blanket at 4 T. The analysis suggests that in the conditions of the DCLL blanket, over the entire blanket length, the concentration boundary layer at the Hartmann wall is thicker than the Hartmann layer. Therefore the entire blanket should be considered as Zone III. An opposite tendency was observed for the SCLL OB blanket where the concentration boundary layer is always thinner than the Hartmann layer. As a result the entire blanket can be treated as Zone I. In the case of the SCLL IB blanket, the concentration boundary layer is first thinner and then thicker than the Hartmann layer. For the lower velocity range, the

transition occurs closer to the blanket inlet, while for the higher velocity range such transition can be observed close to the blanket outlet. Therefore all three zones I, II and III can be present over the SCLL IB blanket length.

Numerical study of the effect of a magnetic field on corrosion of RAFM steel in a turbulent PbLi flow. The effects of a magnetic field on corrosion of ferritic/martensitic steels in a turbulent PbLi flow in a magnetic field were studied for three magnetic field orientations with respect to the main flow direction: steramwise, spanwise and wall-normal. For all cases, the magnetic field always suppresses turbulence resulting in smaller corrosion rates compared to hydrodynamic flows. However, the wall-normal magnetic field has the strongest effect on reduction of the corrosion rate due to more intensive suppression of turbulence compared to the spanwise and streamwise field orientation. The weakest effect is observed in the case of the streamwise magnetic field. Of these three magnetic field orientations, the case of a wall-normal magnetic field is the most interesting as both turbulence suppression and formation of the Hartmann layer occur. Once the flow in a wall-normal magnetic field becomes laminar, the corrosion rate increases slightly due to steeper velocity gradients in the Hartmann layer. This behavior resembles variations of the friction factor in the MHD flow in a wall-normal magnetic field but is quantitatively different. This stresses that there is no direct analogy between momentum and heat and mass transfer once a magnetic field is applied.

Turbulent MHD corrosion in the case of a wall-normal magnetic field. The numerical data for the mass loss in the case of a wall-normal magnetic field was approximated using a specially constructed dimensionless correlation. The correlation for the dimensionless mass transfer

coefficient (Sherwood number) was obtained in the following form: $Sh - Sh_o = c\ Ha^d$. Here, Sannier's empirical correlation [16] can be used to calculate the Sherwood number Sh_0 in a hydrodynamic PbLi flow. The parameters c and d have been evaluated using numerical data, such that $Sh = Sh_0 - 0.792 \times \left(Ha^{1.289} \right)$. In this correlation, the effect of temperature is introduced via the first term on the righ-hand-side of the equation, while the second term is responsible for the effect of a magnetic field. Comparisons of the present data for corrosion with the predictions from Sannier's equation have demonstrated that this equation cannot be applied to fusion blanket applications, as MHD effects in the PbLi flows are dominant in a blanket.

Interpretation of the existing experimental data. The results obtained in the present study for corrosion in laminar and turbulent flows with and without a magnetic field help to explain contradictive experimental observations about the effect of a magnetic field on corrosion rates. In turbulent flows, the corrosion rate is typically reduced as the magnetic field is increased due to suppression of turbulence by a magnetic field. In laminar flows, however, the tendency is opposite. Namely, in rectangular duct MHD flows, much stronger corrosion rates can be observed at the Hartmann walls (doubling the corrosion rates compared to hydrodynamic flows [5] and at the side walls (2-3 times stronger corrosion rates compared to the Hartmann wall). As applied to experimental studies, this suggests that the corrosion data must always be analyzed, taking effects of the magnetic field on the velocity structure into account. These new results also suggest that the presently accepted corrosion limits (maximum corrosion rate and maximum allowable temperature at the solid-liquid interface) for a PbLi blanket have to be revisited.

Corrosion analysis for DCLL blanket. Basic characteristics of MHD flow and heat transfer in the front and the two return ducts of the DCLL blanket were first revisited in this study using the U.S. DEMO blanket as prototypical design. After completing the MHD calculations, the velocity distribution is used as an input data for solving energy equation. Temperature distribution at the RAFM walls was then used to specify the saturation concentration at the RAFM wall.

Mass transfer computations were than performed to analyze the mass transfer and transport of corrosion products with the flowing PbLi in the thin gaps between the flow channels insert and the RAFM walls in the poloidal ducts of the blanket. This study has the purpose to give an initial assessment of the corrosion losses in the DCLL blanket using the temperature and the electrical conductivity of the FCI as a parameter. It was found that corrosion losses in the side gaps (parallel to the magnetic field) are much higher compared to those in the Hartmann gaps (perpendicular to the magnetic field) since the velocity in the side gaps are order of magnitude higher. Almost 98% of all corrosion occurs in the side gaps. The overall mass loss in the DCLL blanket was computed at ~160 g/yr per three ducts. Although the case of the FCI electrical conductivity $\sigma_{FCI} = 10$ S/m demonstrates higher corrosion losses compared to the other case of $\sigma_{FCI} = 0.01$ S/m, the difference between these two cases is insignificant. The average wall thinning in the DCLL blanket was found to be smaller than 20 μm/yr (this limit is widely accepted in present blanket analysis studies) but at some locations the maximum wall thinning was computed at 35 μm/yr.

7.2 Future Studies

The analysis performed in this study is based on corrosion models, which rely on several assumptions. Also some simplifications were introduced, especially in the case of analytical studies. Moreover, the analysis was limited to relatively simple flow geometries. Although all these assumptions are justified using available experimental, numerical or analytical data, further improvements of the models seem to be needed. Below, we summarize some suggestions on improving the models and also give recommendations how the corrosion analysis of the present study can be extended in the future.

The utilized corrosion model assumes pure iron and pure PbLi. However RAFM steel includes other components in addition to iron (*e.g.* chromium) and PbLi may also have some impurities, (*e.g.* oxygen). It is also assumed that in the considered temperature range there are not any chemical interactions between PbLi and SiC. However, in the reality, all these additional components, including some products due to PbLi-SiC reactions will be present. This may affect the corrosion chemistry between RAFM and PbLi and needs to be analyzed and possibly some new parameters/equations should be included in the corrosion models in the future to add new effects. The formation of surface intermetallic compounds and formation of oxide or nitride layer are good examples for such factors.

Liquid metal corrosion for the most part simply depends on the solution rate and the extent of solubility of the solid metal in the liquid metals. In this study it was assumed that the main corrosion mechanism is uniform dissolution of steel in PbLi. It appears to be well justified for RAFM steels in the experimental studies in the past. However, many complicating factors can influence the solution rater or the attainment of the solubility limit. Some minor corrosion mechanisms were also observed in the past experimental studies, such as intergranular

penetration, formation of intermetallic compounds, leaching of particular steel components, *etc*. In some conditions, such mechanisms may become significant, and it will require additional investigations. The present model assumes a mass transfer controlled corrosion process and neglect the transition effects. For high velocities, the surface reactions could control the corrosion processes as discussed in Chapter 1. Other mechanisms such as erosion-corrosion or cavitation-corrosion need to be considered in the future if blanket velocities are sufficiently higher than those in the present study.

Additionally, it was assumed that the only effect of the applied magnetic field on corrosion is due to modification of the velocity field caused by MHD effects. However, another possible effect of the magnetic field is related to the induced electric currents crossing the interface. Moreau [89] stated that the presence of the magnetic field is responsible for the existence of the induced electric currents, which are closing through the electrically conducting duct walls. This may lead to the additional electro-dissolution mechanism, which was found to be quite relevant. At present it is not clear if this effect is really important or not. This also suggests some studies in the future.

The boundary condition on concentration used in this study is the first type boundary condition, which assumes saturation concentration at the interface. This is however an approximation, which is valid if the diffusion processes in the boundary layer are fast enough. Another possible approach to this boundary condition (also discussed in the dissertation) is the third type boundary condition. This approach may be more accurate but it requires the empirical or computational data for the mass transfer coefficient in addition to the saturation concentration. Further evaluations for the boundary condition seem to be useful, especially if the corrosion model was modified to include impurities.

The corrosion analysis is performed in this study for strait, long ducts in a uniform magnetic field. A real blanket always has a very complex geometry, including elbows, manifolds, contractions, expansions, manifolds *etc*. Such geometry variations along the axis may result in a highly intense vortex flow structures and lead to a high local corrosion/precipitation rate. Therefore, more sophisticated corrosion analysis is needed for all blanket elements of complex geometry. Also, the magnetic field has other components (radial and poloidal) and gradients. This may result in more complex MHD flows compared to simplified MHD flows used in the present study. Correspondingly, there will be some effects on corrosion. These effects should be addressed in future studies.

The buoyancy effects and the flow development effects in DCLL flows were not included in this study. To some degree these simplifications can be justified since corrosion occurs in a very thin 2-mm gap where these effects seem to be insignificant. However, full 3D MHD analysis coupled with the mass transfer analysis could be very useful. Also in this study, corrosion was addressed in laminar MHD flows and in turbulent MHD flows. Another important flow regime, which can be envisaged in many blanket flows, is quasi-two-dimensional (Q2D) turbulence, where the turbulent vortices are stretched in the direction of the applied magnetic field. The Q2D turbulence has also many other special features, which make this sort of turbulence to be very different from ordinary turbulence. The effect of Q2D turbulence on corrosion in the PbLi/RAFM system is an additional research topic for the future studies.

The k-ε model for MHD turbulent flows used in this study is limited to the flows in a channel with thin conducting walls, when all induced currents are closing in the flow domain. To include the effect of the conducting wall of a finite thickness, some modifications of the k-ε need to be done or a new turbulence model derived. This is beyond the scope of the dissertation but once

such a model appears, corrosion analysis (similar to that performed in this study) should be repeated.

Finally, the material limits (interface temperature and maximum wall thinning) derived in the past need to be revisited. The suggested corrosion model, correlations and solutions of this dissertation can be used for this purpose. However the corrosion analysis should be coupled with the deposition analysis for the "cold" section of the liquid metal loop, where deposition processes will definitely occur. Such deposition processes are different from the corrosion processes and should be studied in parallel with corrosion studies, including experiments, development of new phenomenological models and computations.

APPENDIX A

A1. Model/Code Validation

After completing the MHD calculations, the velocity profile is used as input data for the mass transfer problem of corrosion products in the DCLL poloidal gaps. These gaps formed between the FCI wall and ferritic steel. In the gap one wall boundary is ferritic steel and the other boundary wall is Silicon Carbide. Ferritic steel boundary is electrically conductive while the Silicon carbide is non-conductive. Typically for MHD problems in literature, classic solution for velocity is derived using the assumption that both boundaries have the same electrical conductivity. However in this study, this is a special kind of Hartmann velocity profile due to the differences in the wall electrical conductivity. Analytical solution derived By Vatazhing [90] for the case with walls of different electrical conductivity, was studied. In order to validate the numerical code for fully-developed MHD flow in a duct with different wall electrical conductivities, comparison made between this analytical solution and numerical computation for the gap.

For incompressible viscous fluid, the governing equations (original notation as used in Vatazhing derivation) for steady fully developed channel flow with the uniformly applied transverse magnetic field (see Fig. 1) can be written as (L=half depth of the channel):

$$\nu\left(\frac{d^2\bar{u}}{dy^2}\right)+a\left(\frac{d\overline{H_x}}{dy}\right)=-\left(\frac{1}{\rho^a}\right)\left(\frac{dP}{dx}\right)=-\left(\frac{a}{L}\right)\left(\frac{P}{R_M^2}\right)$$

(A.1)

$$\eta\left(\frac{d^2\overline{H_x}}{dy^2}\right)+a\left(\frac{d\bar{u}}{dy}\right)=0 \tag{A.2}$$

Or , in non-dimensional form:

$$\left(\frac{d^2\bar{u}}{d\zeta^2}\right)+R_M\left(\frac{d\overline{H_x}}{d\zeta}\right)=-\frac{P}{R_M}, \tag{A.3}$$

$$\chi\left(\frac{d^2\overline{H_x}}{d\zeta^2}\right)+R_M\left(\frac{d\bar{u}}{d\zeta}\right)=0. \tag{A.4}$$

In these equations, the dimensionless quantities $\bar{u}$, $\overline{H_x}$ (induced magnetic field), P , ζ and χ (magnetic Prandtl number) are defined by

$$\bar{u}=\frac{u}{a},\quad \overline{H_x}=\frac{H_x}{H_y},\quad P=-\left(\frac{1}{\rho\nu^2L^{-3}}\right)\left(\frac{dP}{d\chi}\right),\quad \zeta=\frac{y}{L} \text{ and } \quad \chi=\frac{\eta}{\nu}. \tag{A.5}$$

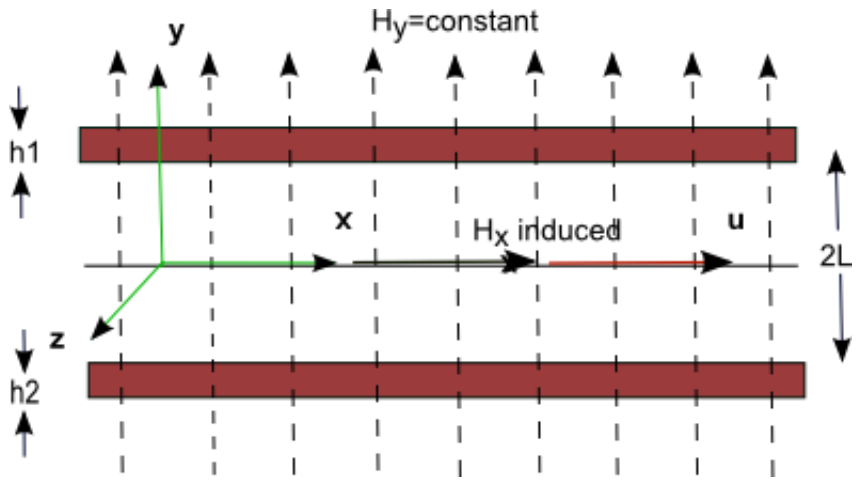

Figure A.1: Channel configuration for MHD laminar flow

The Alfvén wave velocity a is known to be equal to $(\mu_e H_y^2/4\pi\rho)^{1/2}$. The applied magnetic field is denoted by H_y while the fluid density, conductivity, magnetic permeability, and viscous

and electrical diffusivities are denoted respectively by ρ, σ, μ_e, ν and η. Using the Gaussian system of units, the electrical diffusivity η is equal to $(1/\sigma)\cdot(c^2/4\pi\mu_e)$, where c is the speed of light.

The boundary conditions for the problem are listed below as

$$\bar{u} = 0\ , \qquad \text{at} \qquad y = \pm L \qquad \text{or} \qquad \zeta = \pm 1 \tag{A.6}$$

$$\left(\frac{d\overline{H_x}}{d\zeta}\right) + \left(\frac{1}{\varphi_2}\right)\overline{H_x} = 0\,, \qquad \text{at} \qquad \zeta = +1, \tag{A.7}$$

and

$$\left(\frac{d\overline{H_x}}{d\zeta}\right) - \left(\frac{1}{\varphi 1}\right)\overline{H_x} = 0\,, \qquad \text{at} \qquad \zeta = -1 \tag{A.8}$$

The last two are the magneto-hydrodynamic boundary conditions with φ_1 and φ_2 being the electrical conductance ratio of the upper and lower channel walls. They are defined by:

$$\varphi_1 = \frac{\sigma_{w1} h_1}{\sigma_f L}\,, \quad \varphi_2 = \frac{\sigma_{w2} h_2}{\sigma_f L}\,, \tag{A.9}$$

Where w and f stand respectively for wall and fluid; h is the wall thickness subscript 1 and 2 denote lower and upper walls respectively. These magneto-hydrodynamic boundary conditions are exact in this case and have been put in their full generalities; the electrical conductance ratio φ_1 and φ_2 may be different or equal to each other.

The solutions of the velocity equations can be written as:

$$\left(\frac{u}{\nu\ L^{-1}}\right)\left(\frac{1}{P}\right) = \left(\frac{\phi_1}{M}\right)\left[\coth M - \frac{\cosh M\zeta}{\sinh M}\right] \tag{A.10}$$

In this solution M denotes the Hartmann number and is equal to $a\ L\ (\eta\nu)^{-1/2}$, while ϕ_1 represents

$$\phi_1 = \frac{\varphi_2 + \varphi_1 + 2}{(\varphi_2 + \varphi_1)M \coth M + 2} \tag{A.11}$$

The velocity profile obtained from the computational code (using the input data shown in table A.1) was compared with the velocity profile obtained from the analytical solution. Fig. A.2 shows the comparison between the Hartmann velocities profiles at the duct centerline. The results are very close. There is just a few percent difference between the maximum Hartmann velocities. It is reasonable because the flow in the gap are close to that of Hartmann flow, but there still could be some 3D effects. However there is a small difference between the analytical solution and computation shows the 3D effects are very small.

TABLE A.1

Parameters for the Flow in the Channel

Half depth of the channel	0.001 m
Ferritic wall thickness	0.005 m
FCI thickness	0.005 m
Magnetic field strength	4 T
Electrical conductivity of PbLi	0.7E06 $S^{-1}m^{-1}$
Electrical conductivity of Fe (σ_{w1})	1.4E06 $S^{-1}m^{-1}$
Electrical conductivity of FCI (σ_{w2})	0.01 $S^{-1}m^{-1}$

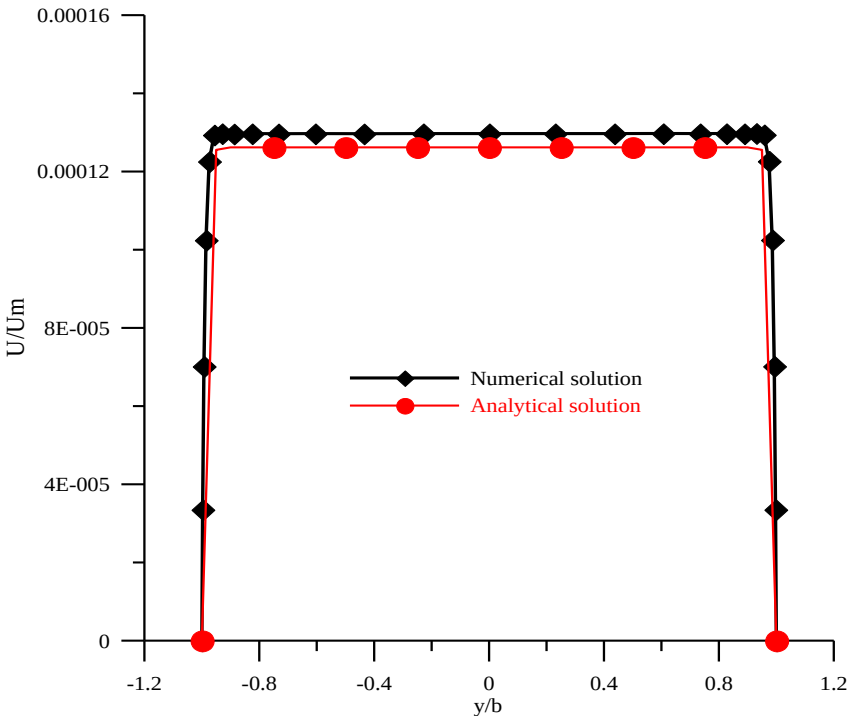

Figure A.2. Velocity profile obtained from the analytical and numerical solution at the duct centerline

REFRENCES

[1] S. Malang, M. Tillack, C. P. C. Wong, N. Morley, S. Smolentsev, Development of the lead lithium (DCLL) blanket concept, *Fusion Science and Technology*, 60 (2011), 249-256.

[2] M. Abdou, *et al*. Blanket Comparison and Selection Study, *ANL/FPP 83-1*,1983 Argonne National Laboratory, Lemont, IL.

[3] D.L. Smith, C.C. Baker, D.K. Sze, G.D. Morgan, M.A. Abdou, S.J. Piet, S.R. Schultz, R.W. Moir, J.D. Gordon, Overview of the blanket comparison and selection study, *Fusion Technology*, 8 (1985) 10-113.

[4] O.K. Chopra, D.L. Smith, Compatibility of ferrous alloys in a force circulation Pb-17Li system, *Journal of Nuclear Materials*, 141-143 (1986) 566-570.

[5] I. Bucenieks, R. Krishbergs, E. Platacis, G. Lipsbergs, A. Shishko, A. Zik, F. Muktepāvela, Investigation of corrosion phenomena in Eurofer steel in Pb-17Li stationary flow exposed to a magnetic field, *Magnetohydrodynamics*, 42 (2006) 237-251.

[6] W.D. Manly, Fundamentals of liquid-metal corrosion, *ORNL-2055*, 1956.

[7] H. Brogstedt, Röhrig, Recent results on corrosion behavior of MANET structural steel in flowing Pb-17Li eutectic, *Journal of Nuclear Materials*, 179-181 (1991) 596-598.

[8] S. Malang, I. N. Sviatoslavsky, Corrosion product cleanup system for a liquid metal cooled fusion power reactor blanket, *Annual Meeting of the American Nuclear Society*, , 1984, New Orleans, USA, 46: 289-290.

[9] W. Krauss, J. Konys, H. Steiner, J. Novotny, Z. Voss, O. Wedemeyer, Development of Modeling Tools to Describe the Corrosion Behavior of Uncoated EUROFER in Flowing Pb-17Li and their Validation by Performing of Corrosion Tests at T up to 550°C, FZKA 7295, Forschungszentrum Karlsruhe, 2007.

[10] F. Balbaud-Célérier, F. Barbier, Investigation of models to predict the corrosion of steels in flowing liquid lead alloys, J. Nuclear Materials 289 (2001) 227-242.

[11] H. Glasbrenner, J. Konys, Z. Voß, Corrosion behavior of low activation steels in flowing Pb-17Li, *Journal of Nuclear Materials*, 281 (2000) 225-230.

[12] S. Smolentsev, R. Moreau, L. Bühler, C. Mistrangelo, MHD thermo fluid issues of liquid-metal blankets: phenomena and advances, *Fusion Engineering and Design*, 85 (2010) 1196-1205.

[13] F. Barbier, A. Alemany, S. Martemianov, On the influence of a high magnetic field on the corrosion and deposition processes in the liquid Pb-17Li alloy, *Fusion Engineering and. Design*, 43 (1988) 199-208.

[14] V. Coen, Corrosion problems in nuclear fusion reactors, in: *A Working Party Report on Corrosion in the Nuclear Industry, European Federation of Corrosion Publications*, Great Britain, 1989.

[15] P. F. Tortorelli, J. H. DeVan, Corrosion of ferrous alloys exposed to thermally convective Pb-17 at% Li, *Journal of Nuclear Materials*, 141-143 (1986) 592-598.

[16] J. Sannier, T. Flament, A. Terlain, Corrosion of martensitic steels in flowing Pb17Li, *Proc. 16th Sym*p. *Fusion Technology*, London, UK, 1990, 901-905.

[17] J. Sannier, M. Broc, T. Flament , A. Terlain, Corrosion of austenitic and martensitic stainless steels in flowing Pbl7Li alloy, *Fusion Engineering and Design*, 14 (1991) 299-307.

[18] G. Benamati, C. Fazio, I. Ricapito, Mechanical and corrosion behavior of EUROFER 97 steel exposed to Pb-17Li, *Journal of Nuclear Materials*,. 307-311 (2011) 1391-1395.

[19] J.Konys, W.Krauss, Z.Voss, O.Wedemeyer, Corrosion behavior of EUROFER steel in flowing eutectic Pb–17Li alloy, *Journal of Nuclear Materials*, 329–333 (2004) 1379–1383.

[20] J. Konys , W. Krauss, Z. Voss, O. Wedemeyer, Comparison of corrosion behavior of bare and hot-dip coated EUROFER steel in flowing Pb–17Li, *Journal of Nuclear Materials*, 367–370 (2007) 1144–1149.

[21] J. Konys , W. Krauss, J. Novotny, H. Steiner, Z. Voss, O. Wedemeyer, Compatibility behavior of EUROFER steel in flowing Pb–17Li, *Journal of Nuclear Materials*, 386–388 (2009) 678–681.

[22] J. Konys, W. Krauss, H. Steiner, Validation of modeling tools to describe the corrosion/precipitation behavior of EUROFER steel in flowing Pb-17Li, *Fusion Science and Technolog*, 56 (2009) 281-288.

[23] P. Tortorelli, Deposition behavior of ferrous alloys in molten lead-lithium, *Fusion Engineering and Design*, 14 (1991) 335-345.

[24] M. G. Barker, M. J. Capadi, The deposition of corrosion products in Pb-17Li, Journal of Nuclear Materials 212-215 (1994) 1534-1537.

[25] P. Tortorelli, in: *Proc. Fourth Int'l Conf. on Liq. Metal Engineering and Technology*, 3 (1988) 528-1 – 528-10.

[26] P. J. Karditsas, C. B. A. Forty, Activation product transport in the helium cooling circuit of the SEAFP plant model 1, *16th IEEE/NPSS Symposium on Fusion Engineering*, 1995, Urbana, IL, USA, 2:1002-1005.

[27] L. Di Pace, F. Dacquait, P. Schindler, V. Blet, F. Nguyen, Y. Philibert, B. Larat, Development of the PACTITER code and its application to safety analyses of ITER primary cooling water system, *Fusion Engineering and Design*, 82 (2007) 237-247.

[28] S. Malang, D. L. Smith, Modeling of Liquid-Metal Corrosion/Deposition in a Fusion Reactor Blanket, *ANL/FPP/TM-192*, 1984.

[29] C. Mistrangelo, MHD and Corrosion Analysis of Dual Coolant PbLi Blanket Modules for *ARIES-CS*, *FZKA 7311*, Forschungszentrum Karlsruhe , 2007.

[30] C.P.C. Wong, S. Malang, M. Sawan, M. Dagher, S. Smolentsev, B. Merrill, M. Youssef, S. Reyes, D.K. Sze, N.B. Morley, S. Sharafat, P. Calderoni, G. Sviatoslavsky, R. Kurtz, P. Fogarty, S. Zinkle, M. Abdou, An Overview of dual coolant Pb-17Li breeder first wall and blanket concept development for the US ITER-TBM design, *Fusion Engineering and Design*, 81 (2006) 461-467.

[31] L. Di Pace, F. Dacquait, P. Schindler, V. Blet, F. Nguyen, Y. Philibert, B. Larat, Development of the PACTITER code and its application to safety analyses of ITER primary cooling water system. Fusion Engineering and Design, 82 (2007) 237-247.

[32] S. Malang, Influence of magnetic field on liquid metal corrosion, 13th SOFT Conf., Varese, Italy, Sept. 24-28, 1984.

[33] A. Terlain, T. Dufrenoy, Influence of a magnetic field on the corrosion of austenitic and martensitic steels by semi-stagnant Pb17Li, *Journal of Nuclear. Materials*, 212-215 (1994) 1504-1508.

[34] R. Krishbergs, E. Ligere, F. Muktepavela, E. Platacis, A. Shishko, A. Zik, Experimental studies of the strong magnetic field action on the corrosion of RAFM steels in Pb17Li melt flows, *Magnetohydrodynamics* 45 (2009) 289-296.

[35] E. Platacis, A. Ziks, A. Poznjak, F. Muktepavela, A. Shishko, S. Sarada, P. Chakraborty, K. Sanjay, M. Vrushank, R. Fotedar, E. K. Rajendra, A. K. Suri, Corrosion phenomena of FMS (P-91) steel in Pb-Li in magnetic field, In: *8th Int. Pamir Conf. on Fundamental and Applied MHD*, Borgo, Corsica, France, 2011, 2: 587-592.

[36] F. Barbier, A. Alemany, S. Martemianov, On the influence of a high magnetic field on the corrosion in the liquid Pb-17Li alloy, *Fusion Engineering and Design*, 33 (1987) 299-308.

[37] F. Barbier, A. Alemany, Magnetic field effect on the deposition of nickel in molten Pb-17Li, *Journal of Nuclear Materials*, 258-263 (1998) 508-512.

[38] E. Dalas, G. Koutsoukos, The effect of magnetic fields on calcium carbonate scale formation, *Journal of Crystal Growth*, 96 (1989) 802-806.

[39] K. Higashitani, A. Kage, S. Katamura, K. Imai, S. Hatade, Effects of a magnetic field on the formation of CaCO3 particles, Journal of Colloid Interface Science, 156 (1993) 90-95.

[40] H.E. Lundager Madsen, Influence of magnetic field on the precipitation of some inorganic slats, *Journal of Crystal Growth*, 152 (1995) 94-100.

[41] H.U. Borgstedt, M. Grundmann, The influence of liquid Pb-17Li eutectic on the mechanical properties of structural materials, *Fusion Engineering and Design*, 6 (1988) 155-158.

[42] M. Broc, T. Flament, P. Fauvet, J. Sannier, Corrosion of austenitic and martensitic stainless steels, *Journal of Nuclear Materials*, 155-157 (1988) 710-714.

[43] H. Glasbrenner, J. Konys, H.D Röhrig, K Stein-Fechne, Corrosion of ferritic-martensitic steels in the eutectic Pb-17Li, *Journal of Nuclear Materials*, 283-287 (2000) 1332-1335.

[44] M. Kondo, T. Nagasaka, T. Muroga, A. Sagara, V. Tsisar, A. Suzuki, T. Terai, M. Takahashi, N. Fujii, T. Yokoyama, H. Miyamoto, E. Nakamura, Flow assisted corrosion and erosion-corrosion of RAFM steel in liquid breeders, *Fusion Engineering and Design*, 86 (2011) 2500-2503.

[45] Y. F. Li, M. Kondo, T. Nagasaka, T. Muroga, V. Tsisar, The corrosion influence of Pb-Li on microstructure and mechanical properties of 9Cr-ODS and CLAM steels, *Fusion Science and Technology*, 60 (2011) 359-363.

[46] T.L. Bergman, A.S. Lavine, F.P. Incropera, D.P. Dewitt. *Fundamentals of Heat and Mass Transfer* , New Jersey : Wiley , 2011.

[47] G.M. Grjaznov, V.A. Evtikhin, I. Lyublinski, Materials science of liquid-Metal systems of thermonuclear reactors, energoatomizdat, *in Russian*, 1989.

[48] M.G Barker, V. Coen, H. Kolbe, J.A Lees, L. Orecchia and T. Sample, The effect of oxygen impurities on the behavior of type 316 stainless steel in Pb-17Li , *Journal of Nuclear Materials*, 155-157(1988) 732-735.

[49] H. Feuerstein, H. Gräbner, J. Oschinski, J. Beyer, S. Horn, L. Hörner, K. Santo, Compatibility of Metals, Alloys and Coatings with Static Pb-17li Eutectic Mixture *FZKA 5596*, Forschungszentrum Karlsruhe (1995).

[50] M. Abdou, A. Ying, N. Morley, K. Gulec, S. Smolentsev *et al*. On the exploration of innovative concepts for fusion chamber technology – *APEX interim report overview*, *Fusion Engineering and Design*, 54 (2001) 181-247.

[51] W. P. Jones, B. E. Launder, The prediction of laminarization with a two-equation model of turbulence, *Int*. *Journal of Heat and Mass Transfer*, 15 (1972) 301-314.

[52] S. Smolentsev, M. Abdou, N. Morley, A.Ying, T. Kunugi, Application of the k-epsilon model to open channel flows in a magnetic field, *Int. Journal of Engineering and Science*, 40 (2002) 693-711.

[53] F. G. Blottner, Variable grid scheme applied to turbulent boundary layers, *Computer Methods in Applied Mechanics and* Engineering, 4 (1974) 179-194.

[54] S. Smolentsev, M. Abdou, N. B. Morley, M. Sawan, S. Malang, C. Wong, Numerical analysis of MHD flow and heat transfer in a poloidal channel of the DCLL blanket with a SiCf/SiC flow channel insert, *Fusion Engineering and Design*, 81 (2006) 549-553.

[55] M. J. Pattison, S. Smolentsev, R. Munipalli, M. Abdou, Tritium transport in poloidal flows of a DCLL blanket, *Fusion Science and Technology*, 60 (2011) 809-813.

[56] D. W. Peacaman, H. H. Rachford, The numerical solution of parabolic and elliptic differential equations, *Journal of the Society for industrial and Applied Mathematics*, 3 (1955) 28-41.

[57] R. Moreau, Magnetohydrodynamics, Kluwer Academic Publishers, Dordrecht, 1990.

[58] R. Moreau, Y. Bréchet, L. Maniguet, Eurofer corrosion by the flow of the eutectic alloy Pb–Li in the presence of a strong magnetic Field. *Fusion Engineering and Design*, 86 (2011) 106-120.

[59] S. Malang, R. Mattas, Comparison of lithium and the eutectic lead-lithium alloy, two candidates liquid metal breeder materials for self-cooled blankets. *Fusion Engineering and Design*, 27 (1995) 399-406.

[60] G. Rampal, A. Li Puma, Y. Poitevin, E. Rigal, J. Szczepanski , C. Boudot, HCLL TBM for ITER-design studies. *Fusion Engineering and Design*, 75-79 (2005) 917-922.

[61] R.A. Gardner AND P.S. Lykoudis. Magneto-fluid-mechanic pipe flow in a transverse magnetic field. Part 1. Isothermal flow. *Journal of Fluid Mechanics*, 47 (1971) 737-764.

[62] R.A. Gardner AND P.S. Lykoudis. Magneto-fluid-mechanic pipe flow in a transverse magnetic field. Part 2. Heat transfer. *Journal of Fluid Mechanics*, 48 (1971) 129-141.

[63] I.R. Kirillov, C.B. Reed, L. Barleon, K. Miyazaki. Present understanding of MHD and heat transfer phenomena for liquid metal blankets. *Fusion Engineering and Designs*, 27 (1995) 553-569.

[64] H. Nakaharai, J. Takeuchi, T. Yokomine, T. Kunugi, S. Satake, *et al*. The influence of a magnetic field on turbulent heat transfer of a high Prandtl number fluid. *Experimental Thermal and Fluid Science*, 32 (2007) 23-28.

[65] A. Terlain, T. Dufrenoy. Influence of a magnetic field on the corrosion of austenitic and martensitic steels by semi-stagnant Pb17Li. *Journal of Nuclear Materials*, 212-215 (1994) 1504-1508.

[66] Ph. Deloffre, A. Terlain, A. Alemany, A. Kharicha. Corrosion study of an austenitic steel in Pb-17Li under magnetic field and rotating flow. *Fusion Engineering and Design*, 69 (2003) 391-395.

[67] S. Smolentsev, S. Saeidi, S. Malang, M. Abdou. Numerical study of corrosion of ferritic/martensitic steels in the flowing PbLi with and without a magnetic field. *Journal of Nuclear Materials*, 432(2011) 294-304.

[68] A. Jess, P. Wasserscheid. Chemical Technology: An Integral Textbook (Wiley, New York, 2012).

[69] M. Abdou, A. Ying , N.B. Morley , K. Gulec, S. Smolentsev, *et al*. On the exploration of innovative concepts for fusion chamber technology. *Fusion Engineering and Design*, 24 (2001)181-247.

[70] H. Branover. Magnetohydrodynamic Flows in Ducts (Wiley, New York, 1978, p. 290).

[71] J. Konys, W. Krauss, J. Novotny, H. Steiner, Z. Voss, *et al.*. Compatibility behavior of EUROFER steel in flowing Pb-17Li. *Journal of Nuclear Materials*, 386-388 (2009) 678-681.

[72] J. Sommeria AND R. Moreau. Why, how, and when, MHD turbulence becomes two-dimensional. *Journal of Fluid. Mechanics*, 118 (1982) 507-518.

[73] D. Krasnov, P. parepalli, O. zikanov, T. boeck. Effect of wall conductivity on turbulent channel flow under spanwise magnetic field. *Proceedings in Applied Mathematics and Mechanics*, 10 (2010) 515-516.

[74] S. satake, T. kunugi, N. naito, A. sagara. Direct numerical simulation of MHD flow with electrically conducting wall. *Fusion Engineering and Design*, 81 (2006) 367-374.

[75] D. K. Sze, M. Tillack, L. El-Guebaly, Blanket systems selection for the ARIES-ST. *Fusion Engineering and Design*, 48 (2000) 371-378.

[76] C. P. C. Wong, S. Malang, M. Sawan, M. Dagher, S. Smolentsev, B. Merrill, M. Youssef, S. Reyes, D. K. Sze, N. B. Morely, S. Sharafat, P. Calderoni, G. Sviatoslavsky, R. Kurtz, P. Fogatry, S. Zinkle, M. Abdou, An overview of dual coolant Pb-17Li breeder first wall and blanket concept development for the US ITER-TBM design. *Fusion Engineering and Design*, 81 (2006) 461-467.

[77] C. P. C. Wong, S. Malang, M. Sawan, S. Smolentsev, S. Majumdar, B. Merrill, D. K. Sze, N. Morely, S. Sharafat, M. Dagher, P. Peterson, H. Zhao, S. J. Zinkle, M. Abdou, M. Youssef, Assessment of first wall and blanket options with the use of liquid breeder. *Fusion Science and Technology*, 47 (2005) 502-509.

[78] S. Malang, M. Tillack, C. Wong, N.B. Morley, S. Smolentsev. Development of the Lead Lithium (DCLL) blanket concept. *Fusion Science and Technology*, 60 (2011) 249-256.

[79] S. Smolentsev, N.B. Morley, M. Abdou, S. Malang. Dual-Coolant Lead-Lithium (DCLL) blanket status and R&D needs. *Submitted to Fusion Engineering and. Design*.

[80] ARIES Team, M. S. Tillack, X. R. Wang, J. Pulsifer, S. Malamng, D. K. Sze, ARIES-ST breeding blanket design and analysis. Fusion Engineering and Design 49-50(2000) 689-695.

[81] J. Davidson, F. Kulacki, Convective heat transfer with electric and magnetic Fields, *Handbook of single-phase convective heat transfer*, S. Kakac, R.Shah, and W. Aung, Eds., John Wiley & Sons, NY, 1987.

[82] S. Smolentsev, N. Moreley, M. Abdou, Code development for analysis of MHD pressure drop reduction in a liquid metal blanket using insulation technique based on a fully developed flow model. *Fusion Engineering and Design*, 73 (2005) 83-93.

[83] R. Alcouffe, R. Baker, F. Brinkley, D. Mar, R. O'Dell, W. Walters, DANTSYS 3.0, A Diffusion Accelerated Neutral Particle Transport Code System, *LA-12969-M, Los Alamos National Laboratory*, 1995.

[84] S. Smolentsev, N. Morley, and M. Abdou, Magnetohydrodynamic and thermal issues of the SiC_f/SiC flow channel insert. *Fusion Science and Technology*, 50 (2006) 106-120.

[85] Changho, P., Kazuyuki, N., Yamamoto, Y., Konishi. Compatibility of materials for advanced blanket with liquid LiPb. in: TOFE 18, San Francisco, 2008, Book of Abstracts, P1.67 .

[86] Morley, N.B., Medina, A., Abdou, M.A.: Measurements of specific electrical contact resistance between SiC and lead-lithium eutectic alloy. in: TOFE 18, San Francisco, 2008, Book of Abstracts, P2.66.

[87] S. Smolentsev, R. Moreau, M. Abdou, Characterization of Key Magnetohydrodynamic Phenomena in PbLi flows for the US DCLL Blanket. Fusion Engineering and Design, 83(2008)771-783.

[88] C. Mistrangelo, MHD and Corrosion Analysis of Dual Coolant PbLi Blanket Modules for ARIES-CS, FZKA 7311, 2007

[89] R. Moreau, Y. Bréchet, L. Maniguet. Eurofer corrosion by the flow of the eutectic alloy Pb-Li in the presence of a strong magnetic field. Fusion Engineering and Design. 86 (2011) 106-120.

[90] A. Vatazhin, G. Lyubimov, and S. Regirer. Magnetohydrodynamic flows in channels. Moscow:Nauka, 1970 (In Russian).